Title

An Integrated Study of the Porous Structure and Mechanical Properties of Diatoms

Author

Diaz Moreno, Miguel Fernando

Publication Date

2015

UNIVERSITY OF CALIFORNIA, MERCED

An Integrated Study of the Porous Structure and Mechanical Properties of Diatoms

A dissertation submitted in partial satisfaction of the requirements
for the degree of Doctor of Philosophy

in

Biological Engineering and Small-scale Technologies

by

Miguel Fernando Diaz Moreno
B.S.c (Universidad Industrial de Santander, Colombia) 2005

Committee in charge

Dr. Lilian Dávila, Chair
Dr. Valerie Leppert
Dr. Yanbao Ma

2015

The dissertation of Miguel Fernando Diaz Moreno is approved, and it is acceptable in quality and form for publication on microfilm and electronically:

Dr. Lilian Dávila, Chair
Date

Dr. Valerie Leppert
Date

Dr. Yanbao Ma
Date

University of California, Merced

2015

Dedicated to my parents, Miguel and Cecilia, and my lovely sister, Marly

TABLE OF CONTENTS

List of Figures

List of Tables

Acknowledgments

First and foremost, I would like to acknowledge my advisor Dr. Lilian P. Dávila for her support and guidance during my Ph.D. studies. I will always appreciate her persistence and patience in helping me keep motivated to accomplish my goals as they have evolved along my career. Thank you also for the teaching mentoring and pursuing opportunities that led to the collaborations with UC Davis and the Federal University of Rio de Janeiro, Brazil. I am also thankful to my dissertation committee for their support and availability when I came across with questions and ideas that could enrich my experience as a researcher.

In addition, I would like to thank other professors at UC Merced, Dr. Ye and Dr. Viney, for allowing me to use their lab space and instruments that helped me to carry out my research project. Furthermore, I would also like to thank Mike Dunlap for their constant help by maintaining the Imaging and Microscopy Facility at UC Merced, and Timothy E. Allis for taking care of our group lab needs.

I am deeply thankful to my family and friends back home for their love and support. My infinite thanks also goes to Shelley Wang for being unconditional during the long hours from the beginning to the end. Each word of encouragement alleviated the hardship of the work and motivated me to continue moving forward.

During this journey I have met incredible people who have impacted my life in many ways professionally and personally, Gayatri and Ankur Kamthe, Benjamin Doblack, Chun Tang, Max Larner, Kennedy Nguyen, Kevin Mercurio, Jimei Yang, Emily Reed, Tzu-I-Chao, Vipawee Limsakoune, and Yang Liu, all who have made this learning process very enjoyable.

Finally, I would like to express my appreciation to various funding sources including startup funds, a NSF-funded COINS subaward, a Miguel Velez and GRC scholarships. Their financial support has been essential in my research and graduate education.

Curriculum Vitae

EDUCATION

Ph.D. Biological Engineering and Small-scale Technologies
School of Engineering, University of California, Merced (2015)
Faculty Advisor: Lilian P. Dávila
Dissertation: An integrated study of the porous structure and mechanical properties of diatoms.

B.S., Chemical Engineering,
School of Chemical Engineering, Universidad Industrial de Santander, Colombia (2005)
Thesis: Formulation and characterization of a polymeric adhesive, and plant design for its fabrication.

ORAL PRESENTATIONS AND PUBLICATIONS

Diaz Moreno, M.F. and L.P. Dávila. Study of Porous Diatom Bio-structures via Experiments and Simulations for Nanotechnology Applications. BEST Research Seminar Series, UC Merced, March 21, 2014.

Diaz Moreno, M.F. and L.P. Dávila. The Study of Hierarchical Porous Biostructures for Nanotechnology Applications. Materials Research Society Fall Meeting, Boston, MA, Dec 3, 2013.

Diaz Moreno, M.F. and L.P. Dávila. Size-dependent Properties of Porous Diatom Biostructures via Experiments and Simulations for Nanotechnology Applications. XII Brazilian Materials Research Society Meeting, Campos do Jordão, Brazil, October 2013.

Diaz Moreno, M.F. and L.P. Dávila. The Size-dependent Structure and Mechanical Properties of Silica Bio-structures via Experiments and Simulations. Materials Research Society Spring Meeting, San Francisco, CA, April 3, 2013.

Diaz Moreno, M.F. and L.P. Dávila. Studies of the Nanomechanical Behavior of Silica Nanowires: Large-scale MD Simulations and Finite Element Method. Materials Research Society Fall Meeting, Boston, MA, Nov 27, 2012.

Diaz Moreno, M.F. and L.P. Dávila. Nanomechanics of Silica Nanowires via Finite Element Method Simulations. Mechanical Engineering Seminar Series, UC Merced, Nov 16, 2012.

Diaz Moreno, M.F. and L.P. Dávila. A FEM Study of the Mechanical Response of Bio-inspired Structures for Nanotechnology Applications. Biological Engineering and Small-Scale Technologies Seminar Series, UC Merced, Nov 4, 2011.

Chao T., Diaz Moreno M.F., Premasekharan G., and Nguyen K. Vita–Chip: An Innovative Design for Cancer Treatment. White Paper. CITRIS Big Idea Competition, Mar 8, 2011.

Diaz Moreno, M., K. Ma, J. Schoenung, and L.P. Dávila. The Hierarchical Porous Structure and Mechanical Properties of Diatoms: An Integrated Approach Toward Engineered Nanotemplates. Submitted Mar 20, 2015, In-review May 9, 2015.

POSTER PRESENTATIONS

Diaz Moreno, M. and L.P. Dávila. The Porous Structure and Mechanical Properties of Amorphous Silica Bio-structures via Simulations. Materials Research Society Fall Meeting, Boston, MA, Nov 29, 2012.

Viscarra, F., M. Diaz Moreno, and L.P. Dávila. Study of Bio-inspired Diatom Structures for Nanotechnology Applications. SHPE National Conference Fall Meeting, Anaheim, CA, Oct 30, 2011.

Diaz Moreno, M. and L.P. Dávila. Nanomechanics of Bio-inspired Diatom Structures for Nanotechnology Applications. Summer School, UIUC, Urbana, IL July 22, 2011.

Diaz Moreno, M.F., F. Viscarra, and L.P. Dávila. The Mechanical Properties Simulations of Bio-inspired Diatom Structures. Materials Research Society Fall Meeting, Boston, MA, Nov 29, 2010.

Diaz Moreno, M.F., F. Viscarra, and L.P. Dávila. Predicting the Mechanical Properties of Biological Inspired Diatoms. COMSOL Conference, Boston, MA, Oct 7, 2010.

SCHOLARSHIPS AND TRAVEL GRANTS

Miguel Velez Fellowship (2011 and 2013)

School of Engineering Graduate Fellowship (2012)

UC Merced Graduate Division Travel Scholarship. Recipient of a travel grant for attending the UC Entrepreneurship Academy at UC Davis (2010).

Carnegie Mellon University-Heinz Foundation Fellowship. Awarded a travel fellowship to participate in a one-week Future Faculty workshop (2009).

OUTREACH ACTIVITIES

SHPE-Noche de Ciencias, Los Árboles Elementary School, San Jose, CA (Oct 2011).

Bobcat Day Nanoscience Exhibit, University of California, Merced (April 2010).

Preview Day Nanoscience Exhibition, University of California, Merced (October 2009).

TEACHING, RESEARCH AND RELATED EXPERIENCE

Teaching Assistant, MSE 112 course, University of California, Merced (2011-2013).

Teaching Assistant, ENGR 45 course, University of California, Merced (2011-2013).

LANGUAGE SKILLS

Fluent in Spanish and basic Italian.

COMPUTER SKILLS

Finite Element Method Software: COMSOL Multiphysics

CAD Software: ProENGINEER, Rhinoceros

Simulations Software: Aspen HYSYS, MATLAB

Operating Systems: OS X, Windows, and Linux

Miguel Fernando Diaz Moreno
May 2015
BEST Graduate Program

An Integrated Study of the Porous Structure and Mechanical Properties of Diatoms

Abstract

Diatoms are microscopic algae featuring porous cell wall structures (frustules). Due to the wide variety of diatom shapes and intricate architectures, diatom frustules are viable prototypes to guide the design and fabrication of nanodevices for applications ranging from sensors to nanotemplates. The porous structure and mechanical behavior of biosilica diatom frustules were evaluated through ambient nanoindentation, AFM-based nanoindentation and finite element method (FEM) analysis. Two diatom species, *Coscinodiscus sp.* (centric) and *Synedra sp.* (pennate), were investigated through ambient nanoindentation and FEM simulation. High-resolution microscopy unveiled the diatom species structures. These diatom frustule dimensions varied largely depending on diatom species (diameters from 70-250 μm and lengths from 100-300 μm) with pore diameters ranging from 0.1-3.0 μm. Young's modulus E and hardness H of the diatom frustules were obtained via ambient nanoindentation. These values varied also depending on diatom species: E from 1.1-10.6 GPa, H from 0.10-1.03 GPa for the *Coscinodiscus sp.*; and E from 13.7-18.6 GPa, H from 0.85-1.41 GPa for the *Synedra sp.* Predictive FEM simulations were performed on well-validated 3D frustule models, to correlate the mechanical response with specific morphology variables such as pore sizes. A correlation between mechanical properties and porosity was established for selected frustules. Furthermore, AFM investigation and FEM simulation involving 3D frustule models with hierarchical geometries were achieved to investigate the structure-property relationship upon compressive loads. AFM imaging and AFM-based nanoindentation of the centric and pennate frustules provided surface morphology and associated load-displacement curves, which were used to further characterize the diatoms. The calculated average E was 21.5 GPa and 26 GPa for the *Coscinodiscus sp.* and *Synedra sp.* respectively, which are higher than the values obtained from ambient nanoindentation. FEM compression simulations were also performed on centric models only to study the role of the hierarchical structures on their mechanical response. Displacement and stress distributions of a three-layered hierarchical frustule model under varied loads were systematically investigated. Results were compared with a stacking of three porous layers for further discussion. Suggestions for future experiments and modeling efforts are provided to enhance the ability to map strategies for the fabrication of 3D nanostructures and nanodevices.

CHAPTER 1: INTRODUCTION

1.1 Background and motivations

Amorphous silica has been studied extensively because its unique properties make it useful in numerous applications and because of its abundance in nature. In particular, silica has been widely investigated since it is the most common compound in the earth's crust, being present in various forms such as silica minerals, silicate minerals and amorphous silica. Silica has five stable polymorphs: quartz, coesite, stishovite, cristobalite, and tridymite, which exist at different temperatures and pressures. In addition, silica has the attribute of performing well at elevated temperatures or in corrosive environments where refractory components or fillers require materials with reliable properties at extreme conditions. Many studies have investigated the mechanical behavior of glass materials; however, their structural modifications and dynamic behavior at elevated load conditions remain incompletely understood. Due to the technological importance of amorphous silica in many applications, its mechanical properties have also been broadly investigated [1].

Several experimental and simulation approaches have been developed over decades for investigation of materials behavior. Atomistic simulations have been used as an important tool for predicting the deformation of amorphous solids, metallic glasses [2,3] and oxide glasses. Nakano *et al*. [4] investigated pore interface growth and the roughness of fracture surfaces in silica via Molecular Dynamics (MD) simulations, finding an inverse relationship between mass density and pore growth. Davila *et al.* [5] performed atomistic simulations of amorphous silica at shock pressures, reproducing experimental pressure-volume behavior and demonstrating nanostructural modifications via ring size distributions. Additionally, continuum mechanics simulations have been used to study the mechanical behavior of thin films [6], biological materials [7], and silicate systems [8]. Pan *et al.* [6] investigated the mechanical properties of thin films via load-deflection curves generated using FEM simulations to mimic AFM-based experimental setups, finding good agreement with experimental results after critical constants were adjusted in up to 30% from their original values. Similarly, Ji *et al.* [7] used FEM simulations of AFM-based nanoindentations to examine the mechanical behavior of biomaterials, reporting size dependence of fracture strength at the nanoscale. Zeng *et al.* [8] analyzed experimental load-depth results of Vickers indentations in several ceramics and glasses (e.g. soda-lime glass, aluminosilicate glass, fused silica) to validate experimental calculation of mechanical properties such as hardness and surface displacement, finding good agreement between experimental and FEM simulation results.

Glasses have been the focus of many studies in the past due to their outstanding properties from the fundamental and applied standpoint. In particular, silica glass, natural and synthesized in the laboratory, has been the center of myriad studies as it belongs to a group of materials considered one of the most ancient in human history, but still not fully understood. In nature, several microorganisms like sponges and diatoms fabricate silica via biomineralization processes, which constitutes the backbone of their complex exoskeleton architectures, allowing them to be sheltered in marine habitats. Given the large and varied population of diatom species and rapid growth rate, their biosilica structures are readily available for potential use in nanoscale applications.

Diatoms are a fascinating major group of algae, which are a primary component of the oceanic food chain, and have intricate silica (hydrated silicon dioxide) exoskeleton structures (also known as frustules) [9], as shown in Figure 1. These microalgae can be found in aqueous environments such as marine and freshwater habitats, and the number of diatom species is estimated to be anywhere from 100,000 to 1,000,000, with structural characteristics varying widely between species [10]. Diatoms play a key role in global carbon fixation, being responsible for around 20% of marine fixation [11]. There are two types of diatoms: centric diatoms (radially symmetric) and pennate diatoms (bilaterally symmetric). Diatom wall structures are mainly composed of amorphous silica, surrounded by a thin organic coating [12]. These porous structures are hierarchically organized featuring nano and micro scale dimensions [13], suggesting potential nanotechnology applications in biophotonics, microfluidics, drug delivery [14], lithography [10], electronics [15] and sensors [11].

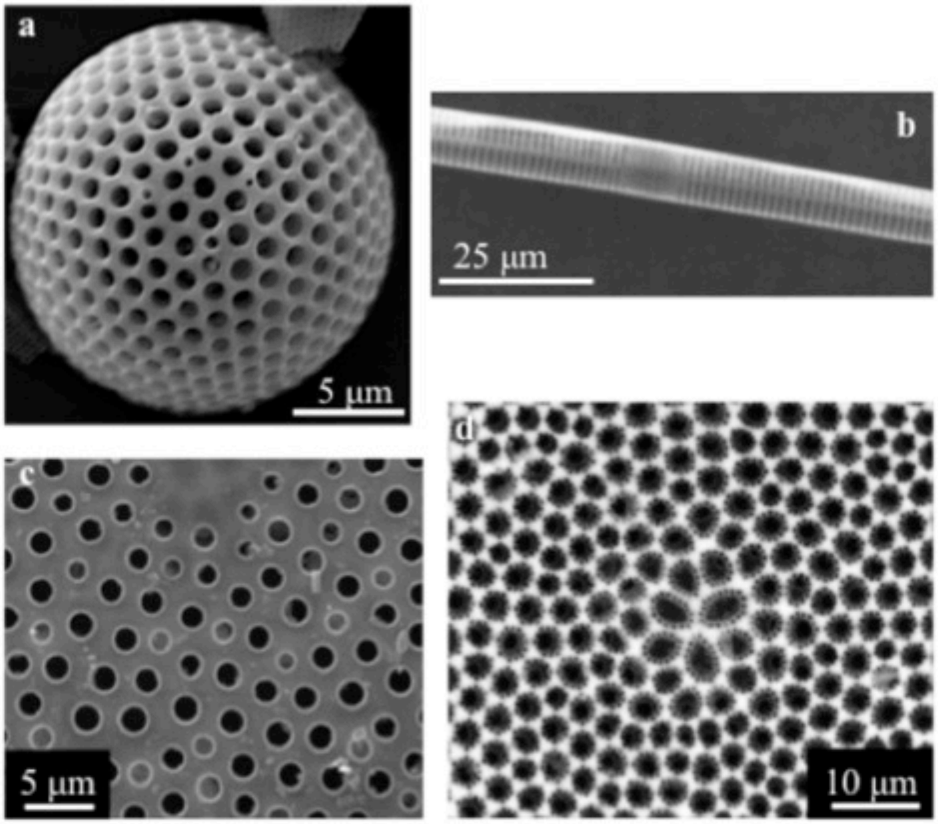

Figure 1. Varied diatom silica structures available in nature displaying species-specific morphology and dimensions: *Stephanopyxis sp.* (*a*), *Synedra sp.* (*b*), and *C. wailesii* (*c*-*d*).

The growth of nanotechnology during the past decades has motivated its interdisciplinary study all over the world. The study of nanomaterials has suggested a wide range of applications for nanometer-sized structures, as these behave quite differently than bulk materials [16] due to their unique characteristics, including increased relative surface area and quantum effects [17]. These characteristics allow nanomaterials to exhibit exceptional optical, magnetic, electrical, and mechanical properties advantageous over macro materials [18], allowing the pursuit of applications such as drug delivery systems, optical sensors, actuators, catalytic components and self-assembled devices [19]. In particular, oxide nanostructures have merited special attention due to their optical properties, suggesting potential application in optical waveguides [20] and photonic devices [21].

Characterization of nanomaterials has been made possible by the development of techniques such as atomic force microscopy (AFM), scanning tunneling microscopy (STM), scanning electron microscopy (SEM), and transmission electron microscopy (TEM). The AFM technique is widely used for investigating surfaces of nanomaterials [22] and characterizing them mechanically on an atomic scale [23-25]. STM is a technique frequently used for imaging surfaces atomically [26], while SEM provides a 3-dimensional analysis of the sample. TEM is an effective technique for providing detail at the atomic level through the interaction of a thin section of the sample with a beam of electrons [27]. All of the above techniques together have facilitated the understanding of nanomaterials according to their particular advantages, expanding scientific discovery more rapidly.

The production of structures with nanometer dimensions has also been widely pursued in the past few decades. In particular, some experimental work has been reported in characterizing the mechanical properties of amorphous silica nanowires. Dikin *et al.* [18] have calculated the bending modulus using the mechanical resonance method, finding a value close to 47 GPa for amorphous silica nanowires of 100 nm in diameter and 10 µm in length. Also, Ni *et al.* [28] examined amorphous silica nanowires of 50 to 100 nm in diameter by AFM three-point bending tests, obtaining values of elastic modulus around 76.6 GPa, close to values reported for bulk silica.

Currently, nanotechnology is being explored in several research fields from chemistry, physics and biology to medicine, engineering and electronics. The unique properties of nanomaterials have allowed their introduction into commercial applications, confirming their increasing importance. The basic methods developed for fabricating nanomaterials include bottom-up and top-down approaches. The top-down approach involves the fabrication of nanostructures from an existing solid of a larger size than the final structure. The size reduction is achieved by applying external radiation or chemical processes. In the top-down approach, accomplishing nanostructural assembly is not necessary because all the parts are patterned and built in place, which offers a significant advantage for applications such as optical lithography and fabrication of integrated circuits. In the bottom-up approach, the use of physical or chemical forces at the nanoscale plays a key role in achieving assembly atom by atom into larger arrangements

[29], facilitating the development of complex morphologies. In brief, the top-down methods include methods such as compaction and consolidation, electrospinning and arc discharge, while the bottom-up methods involve techniques such as chemical vapor deposition, atomic layer deposition and electron deposition [29]. Recently, biological systems have been the inspiration of bottom-up approaches to reproduce 3D nanostructures from small building blocks with self-assembly capabilities.

Despite all of the attributes of nanotechnology, there are limitations to full incorporation of these novel materials into commercial applications. The main limitation of nanomaterials is the lack of scalability from the lab to larger production, which would require a low production cost (production at low temperature and pressure). Another limitation in fabricating nanomaterials is the challenge of exact reproduction of material properties between production batches as well as the difficulty of manipulation of the nanostructures for device fabrication. In addition, characterization of nanomaterials presents a challenge, although there have been improvements with recent advances in microscopy techniques. Likewise, the use of nanomaterials has raised concerns about their possible environment hazards and health effects. Furthermore, in order to optimize the properties of nanomaterials, it is necessary to organize them in regular arrays through precise, reproducible, and scalable methods. 2D templates and 3D structures fabricated by a bottom-up approach have been utilized to address the challenge of placing nanomaterials in arrangements where their properties can be exploited [30].

1.1.1 Diatoms in nature

Diatoms are photosynthetic eukaryotic unicellular organisms, which constitute approximately 40% of the marine production and are responsible of fixing ~25% of the carbon dioxide present in the ocean. With more than hundred thousand different species, diatoms have become broadly studied because of their relation to climate change, biofouling, and evolution [11]. One of the most outstanding features of diatoms is their cell wall (Figure 2), which is finely coated with organic material. This wall is mostly composed of hydrated silica ($SiO_2.nH_2O$), and the silica content is estimated to account for 60% or more of the dried weight. The cell wall is composed of two large and intricate parts called valves, held together by thin belt-like pieces called girdle bands. The valves fit one on top of each other, similar to a Petri dish, and are retained in place by the girdle bands. The set of components together is called a frustule, and it fits tightly, allowing the entrance of nutrients only through the pores and slits in the valves while protecting the cell from predators [31]. Diatoms reproduce via an asexual cycle in which the mother cell gives a valve to each daughter cell. After several replications, the frustule shrinks considerably in size and a sexual cycle follows to regulate the frustule size. The silica cell walls are created in the silica deposition vesicles within the diatom by depositing layers of silica glass while providing them with intricate features [32].

The natural world presents a number of examples of intricate 3D nanostructures with reproducible micro- and nano-scale features. Biological examples of systems, which create 3D rigid microstructures of silica using a bottom-up approach can be found in aquatic organisms such as hexactinellid sponges or diatoms. These organisms have developed complex glassy structures that suggest potential new approaches to materials fabrication at the nanometer scale. Diatom structures have been extensively studied in recent decades primarily for biological purposes, due to their importance in ecosystems and carbon dioxide fixation [9]. However, in recent years, the research community has been focusing on diatom structures because of their micro- and nano-size features, and symmetrical pore arrays, for nanotechnology applications.

Diatoms have a wide range of highly patterned structures such as ribs, ridges and other similar features in the micrometer and nanometer scale.

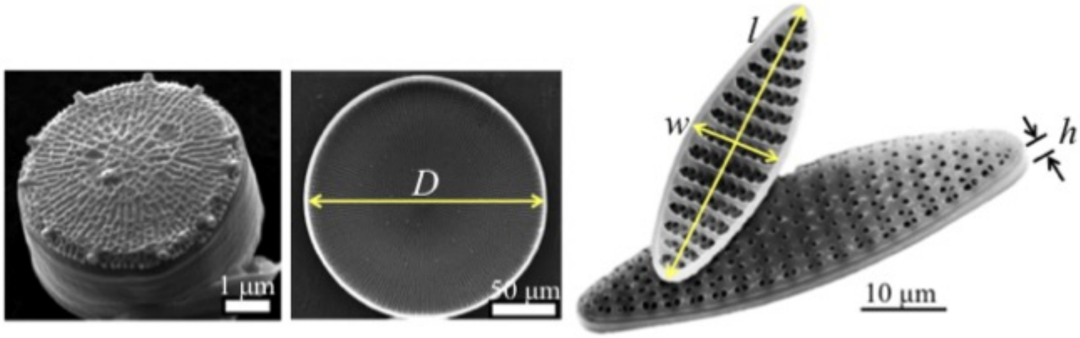

Figure 2. SEM diatom images of centric *Coscinodiscus wailesii* (left) [13], and pennate *Fragilariopsis kerguelensis* (right) [33] with relevant frustule dimensions: diameter *D*, length *l*, width *w*, and height *h* respectively.

1.1.2 Diatoms in the laboratory

The complex porous structures of diatoms have attracted scientists in hopes recreating similar 3D structures using current technology. The study of the chemical compounds used during silica deposition such as amino acids, peptides and polyamides have led to the identification of silaffins (highly charged proteins) as the major contributor to the formation of the complex hierarchical diatom cell walls [34]. Recently, the genomic sequence of *Thalassiosira pseudonana* diatom species has been accomplished, opening the door to possible engineered diatom structures [35]. In addition, Hildebrand *et al.* [36] have demonstrated the isolation of genes encoding silicic acid transporters, which is promising for possible manipulation of diatom structures, as those genes are responsible for the transport across the cell and perhaps the construction of the macro structure.

Several efforts have been made toward replicating diatom structures using techniques currently applied in nanotechnology. Belegratis and coworkers [37] have used natural diatoms for creating templates, as well as replicas via two-step soft lithography and 3D laser lithography, to use those templates in nanoimprint lithography processes. In both cases the models obtained replicated most of the features of the diatoms at the micrometer scale.

In another study, 3D printing of hierarchical structures inspired by diatoms has suggested that lightweight porous structures are able to tolerate higher loads than their constituent materials in other configurations, attributing the damage tolerance to the bio-inspired hierarchical architecture [38].

1.1.3 Diatom properties

Understanding the physical properties, and in particular the mechanical characteristics, of diatoms is extremely useful for future nanotechnology applications (Figure 3). A comprehensive mechanical characterization of these siliceous structures will allow the design of suitable applications such as photonic devices, nanotemplates or drug delivery carriers, and appropriate usage conditions. In order to take full advantage of these characteristics, a thorough understanding of the dependence of the mechanical properties of the diatom structures on morphological and biological variables is necessary. The main focus of this work was to study the dependence of the mechanical properties of diatom structures on their morphological variables.

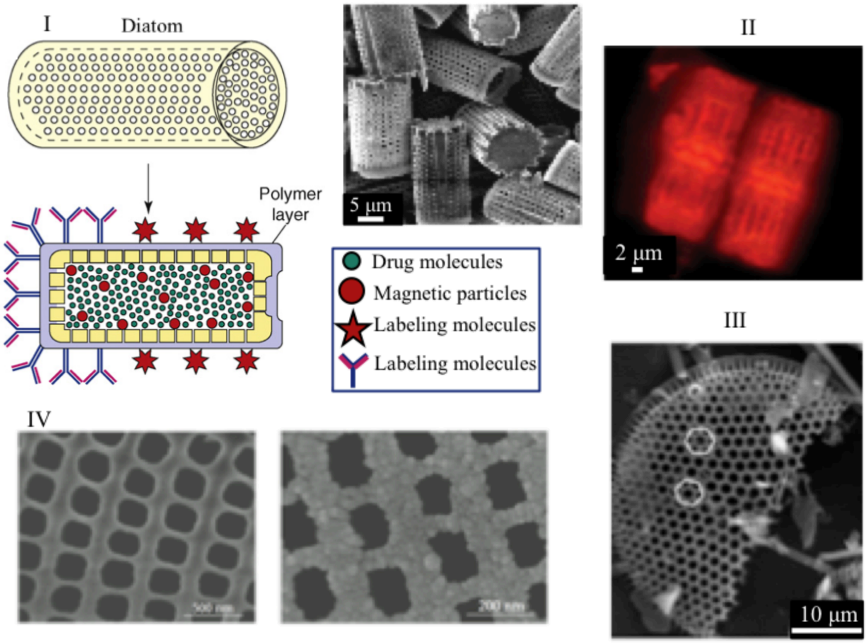

Figure 3. Potential nanodevices using diatom frustules from different species. A functionalized frustule of a pennate diatom is proposed as drug delivery carrier (I) [14]. A photonic device using a diatom is displayed on top right (II) [19], and nanotemplates of centric diatoms are shown in (III) and (IV), with the latter having the pore size tuned by deposition of materials [39-40].

To date, few studies have been reported which focus mainly on characterizing the complex biological structures of diatoms. Mechanical analysis and characterization of diatom structures have been pursued mainly using atomic force microscopy, nanoindentation and SEM techniques. Initial studies conducted by Higgins *et al.* [41] focused on the topography and mechanical properties of adhesive mucilages secreted by the *Craspedostauros australis* diatom species using the AFM technique. A soft and cohesive outer mucilage layer was found, encasing most of the frustule. Subsequently, Hamm *et al.* [42] investigated the mechanical protection offered by the frustule using needle-loading tests on several species, discovering an inverse relationship between the size of the frustule and the force required to break it. Later, *in vivo* studies of several diatom species were performed by Higgins *et al.* [43] using AFM experiments to determine morphology features of the diatom frustule. Losic *et al.* [44] analyzed morphology via SEM and performed AFM-based nanoindentations, mapping the frustule of the *Coscinodiscus* diatom species, and finding that the elastic modulus varied widely (1.7-15.6 GPa) depending on porosity, thickness and pore size. In further studies, Losic *et al.* [45] compared morphological features of *Coscinodiscus* versus *Thalassiosira eccentric* species, including the organization of porous silica layers, topography, pore size, shape and density. Recently, Hildebrand *et al.* [46] investigated other regions in several diatom biostructures (e.g., valves, girdle bands and bristles) using AFM, enabling visualization of girdle bands at several scales and describing varied porous morphologies within the frustule. Additionally, Yao *et al.* [47] performed localized nanoindentations of *Coscinodiscus* diatom frustules at different incident angles to calculate their elastic modulus and hardness, finding low Young's modulus E (ranging from 0.59-2.77 GPa) and hardness values (ranging from 0.03-0.12 GPa), and a good agreement with Finite Element Method (FEM) simulations performed using similar experimental conditions. From all previous studies, a variety of mechanical properties of biosilica diatom frustules based on nanoindentation have been reported. The challenges of measuring mechanical properties of diatom species experimentally are due to the differences existing between each species and sample preparation. A clear correlation between mechanical properties and diatom features (e.g., porosity, thickness and pore size) has not yet been established.

1.2 Scope of this study and objectives

The approach used in this work consists of describing the structural modifications and mechanical behavior of diatom structures and models under different load conditions at room temperature using suitable techniques. The first goal is to understand the mechanical response (hardness and Young's modulus) of selected diatom structures under different compression loads using ambient and AFM-based nanoindentations. Computer simulation assists to analyze and predict the mechanical behavior of diatom structures in conditions not experimentally measureable (e.g. von Mises stress), but essential for nanotechnology applications. In addition, realistic diatom models are helpful in the study of the mechanical behavior of varied diatom frustules with specific morphology variables (e.g. pore or slit sizes). Results from calculated von Mises stress and displacement distributions can be used to unveil the effect that uniform loads have on these frustules and to evaluate a possible correlation between mechanical properties and porosity. In Chapter 2, the methodology of these simulations is described in detail, as well as the type of experimental techniques carried out. Well-established ambient and AFM nanoindentation protocols are used for determining the mechanical properties of diatom biostructures. The results from ambient nanoindentations and uniform compression load simulations are described in Chapter 3. The approach of coupling experimental and simulation methods allows the analysis of the mechanical properties of diatom frustules with characteristic dimensions, selected based on their pore size and arrangement and potential applications.

The second goal of this study is to perform more precise measurements via AFM of the mechanical properties of the selected diatom frustules, to understand the possible sources of property variation characteristic of diatom structures. More realistic diatom models can aid the investigation of the characteristic hierarchical assembly of layers in centric frustules as in nature, when subjected to uniaxial compression FEM simulations. Our simulations are analyzed in terms of hierarchical structure, displacement and von Mises distributions, and the response of mechanical response of frustules. The methodology used for these measurements and calculations is explained in Chapter 2 and the results are presented in Chapter 4.

The FEM-based simulations can be used to analyze von Mises stress and displacement distributions within diatom structures under uniform compression and nanoindentation conditions similar to experiments. To achieve this, it is necessary to build 3D diatom models using CAD software with characteristic micrometer and nanometer dimensions as obtained by SEM imaging. Simulation conditions can be pursued at room temperature similar to the experimental tests. FEM simulations of uniaxial compression and nanoindentation conditions can be pursued on diatom structures, and the results can be compared against experiments. Von Mises stress distributions in the strained diatoms can be evaluated for dependence on the defined morphological parameters.

The overall goal of this study is to investigate the mechanical behavior of biological diatom structures from the micro- to the nano-scale. To accomplish this, it is necessary to prepare selected diatom samples for ambient and AFM-based nanoindentations by removing organic material from the diatom frustules, allowing the determination of frustule geometries and dimensions via visual characterization using SEM imaging. Subsequently, nanoindentations on selected diatom frustules are needed to evaluate the effect of morphology on their mechanical properties using AFM. The pre- and post-nanoindentation SEM images permit the analysis of failure modes in the diatoms frustules at different compressive loads. In addition, the information obtained can be used to calculate the mechanical properties (e.g. Young's modulus) of selected diatom frustules with a defined set of morphological parameters. This allows the creation of a database, which can be correlated with diatom species with their corresponding stiffness, nanofeatures, and dimensions for future design purposes.

1.3 Significance

Researchers have turned their attention to the usage of bio-inspired materials with regular microscopic structures, which feature morphologies at the micro and nano size, such as diatoms [48]. Due to their availability in nature, low cost and ease of production at ambient conditions, diatom structures are a potential alternative to be used as templates for nanotechnology applications. The advances achieved in genetic modification of frustule geometry and size suggests a mechanism to accomplish the controlled adjustment of these amorphous silica structures for use in future applications. However, a clear understanding on the mechanical behavior of these complex hierarchical structures has not yet been achieved.

This investigation provides an understanding of the relationship between the mechanical properties and the morphology of selected diatom species. The use of experimental techniques such as ambient nanoindentation and AFM, coupled with computer simulation, gives a better understanding of the behavior of the structures from the nano- to the micro-scale. In addition, the use of FEM simulations allows the investigation of potential scenarios where engineered diatom structures could outperform natural frustules, taking advantage of their strong but lightweight hierarchical architectures.

This study can contribute to current investigations in areas such as bioengineering, nanotechnology, materials science and optics among others where information about mechanical performance is critical for successful device design.

1.4 References

1. Sugiura, H., Ikeda, R., Kondo, K., and Yamadaya, T. Densified silica glass after shock compression. *Journal of Applied Physics* **81**, 1651-1655 (1997).

2. Falk, M.L. and Langer, J.S. Dynamics of viscoplastic deformation in amorphous solids. *Physical Review E* **57**, 7192 (1998).

3. Schuh, C.A. and Lund, A.C. Atomistic basis for the plastic yield criterion of metallic glass. *Nature Materials* **2**, 449-452 (2003).

4. Nakano, A., Kalia, R.K. and Vashishta, P. Growth of pore interfaces and roughness of fracture surfaces in porous silica: million particle molecular-dynamics simulations. *Physical Review Letters* **73**, 2336 (1994).

5. Dávila, L.P., Caturla, M.-J., Kubota, A., Sadigh, B., Díaz de la Rubia, T., Shackelford, J. F., Risbud, S. H., and Garofalini, S. H. Transformations in the medium-range order of fused silica under high pressure. *Physical Review Letters* **91**, 205501 (2003).

6. Pan, J.Y., Lin, P., Maseeh, F. and Senturia, S.D. Verification of FEM analysis of load-deflection methods for measuring mechanical properties of thin films. *Solid-State Sensor and Actuator Workshop*, *4th Technical Digest, IEEE* 70-73 (1990).

7. Ji, B. and Gao, H. Mechanical properties of nanostructure of biological materials. *Journal of the Mechanics and Physics of Solids* **52**, 1963-1990 (2004).

8. Zeng, K., Soderlund, E., Giannakopoulos, A.E. and Rowcliffe, D.J. Controlled indentation: A general approach to determine mechanical properties of brittle materials. *Acta Materialia* **44**, 1127-1141 (1996).

9. Raven, J.A. and Waite, A.M. The evolution of silicification in diatoms: Inescapable sinking and sinking as escape? *New Phytologist* **162**, 45-61 (2004).

10. Drum, R.W. and Gordon, R. Star trek replicators and diatom nanotechnology. *Trends in Biotechnology* **21**, 325-328 (2003).

11. Kröger, N. and Poulsen, N. Diatoms, from cell wall biogenesis to nanotechnology. *Annual Review of Genetics* **42**, 83-107 (2008).

12. Almqvist, N., Delamo, Y., Smith, B.L., Thomson, N.H., Bartholdson, A., Lal, R., Brzezinski, M. and Hansma, P. K. Micromechanical and structural properties of a pennate diatom investigated by atomic force microscopy. *Journal of Microscopy* **202**, 518-532 (2001).

13. Hildebrand, M. Diatoms, biomineralization processes, and genomics. *Chemical Reviews* **108**, 4855-4874 (2008).

14. Gordon, R., Losic, D., Tiffany, M.A., Nagy, S.S. and Sterrenburg, F.A.S. The glass menagerie: diatoms for novel applications in nanotechnology. *Trends in Biotechnology* **27**, 116-127 (2009).

15. Parker, A.R. and Townley, H.E. Biomimetics of photonic nanostructures. *Nature Nanotechnology* **2**, 347-353 (2007).

16. Law, M., Goldberger, J. and Yang, P. Semiconductor nanowires and nanotubes. *Annual Review of Materials Research* **34**, 83-122 (2004).

17. Dowling, A. Nanoscience and Nanotechnologies. *Royal Society and Royal Academy of Engineering*, London, (2004).

18. Dikin, D.A., Chen, X., Ding, W., Wagner, G. and Ruoff, R.S. Resonance vibration of amorphous SiO_2 nanowires driven by mechanical or electrical field excitation. *Journal of Applied Physics* **93**, 226-230 (2003).

19. Sandhage, K.H., Dickerson, M.B., Huseman, P.M., Caranna, M.A., Clifton, J. D., Bull, T.A., Heibel, T.J., Overton, W.R., and Schoenwaelder, M.E.A. Novel, bioclastic route to self-assembled, 3D, chemically tailored meso/nanostructures: shape-preserving reactive conversion of biosilica (diatom) microshells. *Advanced Materials* **14**, 429-433 (2002).

20. Tong, L., Lou, J. and Mazur, E. Single-mode guiding properties of subwavelength-diameter silica and silicon wire waveguides. *Optics Express* **12**, 1025-1035 (2004).

21. Tong, L. and Mazur, E. Glass nanofibers for micro- and nano-scale photonic devices. *Journal of Non-Crystalline Solids* **354**, 1240-1244 (2008).

22. Binnig, G., Quate, C.F. and Gerber, C. Atomic force microscope. *Physical Review Letters* **56**, 930 (1986).

23. Butt, H.-J., Cappella, B. and Kappl, M. Force measurements with the atomic force microscope: Technique, interpretation and applications. *Surface Science Reports* **59**, 1-152 (2005).

24. Gaboriaud, F. and Dufrêne, Y.F. Atomic force microscopy of microbial cells: Application to nanomechanical properties, surface forces and molecular recognition forces. *Colloids and Surfaces B: Biointerfaces* **54**, 10-19 (2007).

25. Allison, D., Dufrêne, Y.F., Doktycz, M.J. and Hildebrand, M. Biomineralization at the nanoscale: learning from diatoms. *Elsevier*, (2008).

26. Binnig, G., Rohrer, H., Gerber, C. and Weibel, E. Surface studies by scanning tunneling microscopy. *Physical Review Letters* **49**, 57 (1982).

27. Williams, D.B. and Carter, C.B. The transmission electron microscope: A textbook for materials science, *Springer* US, (2009).

28. Ni, H., Li, X. and Gao, H. Elastic modulus of amorphous SiO_2 nanowires. *Applied Physics Letters* **88**, 043108 (2006).

29. Ozin, G.A. and Arsenault, A.C. Nanochemistry: A chemical approach to nanomaterials. *Royal Society of Chemistry*, Cambridge, UK, (2005).

30. Xia, Y. and Lim, B. Nanotechnology: Beyond the confines of templates. *Nature* **467**, 923-924 (2010).

31. Round, F.E., Crawford, R.M. and Mann, D.G. Diatoms: biology and morphology of the genera. *Cambridge University Press*, New York, (1990).

32. Kröger, N. Prescribing diatom morphology: Toward genetic engineering of biological nanomaterials. *Current Opinion in Chemical Biology* **11**, 662-669 (2007).

33. Smetacek, V. Oceanography: Bacteria and silica cycling. *Nature* **397**, 475-476 (1999).

34. Wieneke, R., Bernecker, A., Riedel, R., Sumper, M., Steinem, C., Geyer, A. Silica precipitation with synthetic silaffin peptides. *Organic and Biomolecular Chemistry* **9**, 5482-5486 (2011).

35. Armbrust, E.V. *et al.* The genome of the diatom *Thalassiosira Pseudonana*: Ecology, evolution, and metabolism. *Science* **306**, 79-86 (2004).

36. Hildebrand, M. Biological processing of nanostructured silica in diatoms. *Progress in Organic Coatings* **47**, 256-266 (2003).

37. Belegratis, M.R., Schmidt, V., Nees, D., Stadlober, B. and Hartmann, P. Diatom-inspired templates for 3D replication: Natural diatoms versus laser written artificial diatoms. *Bioinspiration and Biomimetics* **9**, 016004-1-11 (2014).

38. Jang, D., Meza, L.R., Greer, F. and Greer, J.R. Fabrication and deformation of three-dimensional hollow ceramic nanostructures. *Nature Materials* **12**, 893-898 (2013).

39. Gutu, T., Jeffryes, C., Wang, W., Chang, C.-H., Rorrer, G.L., and Jiao, J. Structural and electrical characterization of diatom *Pinnularia sp.* biosilica coated with CdS thin film. *Materials Research Society Symposium.* **P**., 1187 (2009).

40. Pérez-Cabero, M., Puchol, V., Beltrán, D. and Amorós, *P. Thalassiosira Pseudonana* diatom as biotemplate to produce a macroporous ordered carbon-rich material. *Carbon* **46**, 297-304 (2008).

41. Higgins, M.J., Crawford, S.A., Mulvaney, P. and Wetherbee, R. Characterization of the adhesive mucilages secreted by live diatom cells using atomic force microscopy. *Protist* **153**, 25-38 (2002).

42. Hamm, C.E., Merkel, R., Springer, O., Jurkojc, P., Maier, C., Prechtel, K., and Smetacek, V. Architecture and material properties of diatom shells provide effective mechanical protection. *Nature* **421**, 841-843 (2003).

43. Higgins, M.J., Sader, J.E., Mulvaney, P. and Wetherbee, R. Probing the surface of living diatoms with atomic force microscopy: the nanostructure and nanomechanical properties of the mucilage layer. *Journal of Phycology* **39**, 722-734 (2003).

44. Losic, D., Short, K., Mitchell, J.G., Lal, R. and Voelcker, N.H. AFM nanoindentations of diatom biosilica surfaces. *Langmuir* **23**, 5014-5021 (2007).

45. Losic, D., Pillar, R., Dilger, T., Mitchell, J. and Voelcker, N. Atomic force microscopy (AFM) characterisation of the porous silica nanostructure of two centric diatoms. *Journal of Porous Materials* **14**, 61-69 (2007).

46. Hildebrand, M., Doktycz, M. and Allison, D. Application of AFM in understanding biomineral formation in diatoms. *Journal of Physiology* **456**, 127-137 (2008).

47. Yao, S., Subhash, G. and Maiti, S. Analysis of nanoindentation response of diatom frustules. *Journal of Nanoscience and Nanotechnology* **7**, 4465-4472 (2007).

48. Dragnea, B. Bio-inspired materials: Unnatural life. *Nature Materials* **7**, 102-104 (2008).

CHAPTER 2: METHODOLOGY

The objectives defined previously in Chapter 1 of this dissertation were accomplished successfully using different methods including experiments and simulations.

2.1 Experimental section

This component includes the mechanical investigation of diatom frustules, employing standard characterization techniques that are commonly used in studying nanomaterials.

Ambient and AFM nanoindentation techniques were used to calculate the mechanical properties (e.g. Young's modulus and hardness) of diatom structures, and their dependence on morphological variables (e.g. pore diameter, pore location). For this purpose, it was also necessary to use imaging techniques such as SEM to determine the initial and final state (before and after indentation loads) of the diatom architectures.

The overall objective of the experimental section of the project was to completely characterize diatom structures via SEM, ambient and AFM-based nanoindentations toward their potential use in nanotechnology applications.

<u>Justification of methods</u>: The resolution of SEM and AFM imaging techniques was considered adequate for this study of diatoms to demonstrate the important micro- and nano-morphological features that affect their mechanical properties. SEM and AFM methods have been widely used in previous independent diatom studies. In addition, ambient and AFM-based nanoindentation were determined appropriate for the study of diatom frustules due to their optimal load sensitivity and high spatial resolution, as reported before for porous alumina and other biomaterials similar to diatoms.

2.1.1 Diatom species selection and sample preparation

Diatom species were selected based on two main requirements: regular pore arrangement and pore size suitable for nanotechnology applications (smaller than 600 nm) [1-3]. An initial survey indicated that *Coscinodiscus sp.* and *Synedra sp.* diatom species met the above desired selection requirements while having different frustule symmetry.

Separated vials containing diatom species *Coscinodiscus sp.* and *Synedra sp.* (pre-cleaned with nitric acid to remove organic material and mineral debris such as sand and mud, and dissolved in 70% ethanol) were purchased from Carolina Biological Supply Company (Burlington, North Carolina). This diatom frustule solution contained cleaned diatom frustules (with complete valves and girdle bands) and broken pieces of fossil diatoms.

A verification process was carried out to determine when the diatom structure was free of organic material and ready to be tested, using a standard optical microscope (Olympus SZX16 stereomicroscope).

The sample preparation for optical analysis and SEM imaging began with the preparation of an adhesive solution by mixing gelatin and deionized water (3% *w/v*) at 60 °C for 3 minutes. A glass slide was spin-coated with 100 μL of the gelatin solution, creating a thin film that increased adhesion between the diatom frustules and the slide. A small amount (50 μL) of the diatom frustule solution was placed on a glass slide coated with the gelatin solution. The diatom frustule solution was air-dried, and the deposited frustules were arranged using a 3D-printed micromanipulator and a glass microneedle via light microscopy (Appendix A). Optical images were used to verify when diatom structures were free of organic material, as reported elsewhere [4]. Several arranged glass slides containing diatom frustules were prepared similarly, and heated up to 30 °C for approximately 1 minute to promote further adhesion between the frustules and slides. This sample preparation method was found to provide good quality adhesion characteristics (improved over the Poly-L-lysine method used in prior similar efforts [5] and tested for comparison), maintaining diatom frustules in place when considerable forces were applied directly on them with a glass microneedle.

2.1.2 Scanning Electron Microscopy (SEM) characterization

First developed in 1942 by Zworykin, SEM imaging is a powerful technique that allows topographical examination and characterization of organic and inorganic materials from nanometer to micrometer size by providing three-dimensional images of the surface of the sample [6-7].

2.1.2.1 General description

SEM works by exposing the sample to a focused electron beam that can be either static at one point (localized analysis) or mobile (surface analysis) within the sample. As a result of the electron beam-specimen interactions the kinetic energy initially carried in the electron beam is dissipated, and resultant signals that include secondary electrons, backscattered electrons, X-rays, and phonons of different energies are generated. The signals resulting from SEM investigation give information about the surface or morphology, chemical composition, and crystalline structure of the sample analyzed.

The main components of a scanning electron microscope include the electron source and lenses, deflection system, electron detector, camera and operator controls. Initially the electron beam is generated in the electron source or gun, and accelerated to energy between 0.1 to 30 keV. Subsequently, the electron beam is demagnified and focused to a smaller target radius by the electron lenses located in the electron column. Finally, the resultant signals of the electron beam-specimen interaction are collected and converted to point-by-point intensity changes creating the image [7]. There are also several modes in which the SEM can be operated that include resolution mode (small electron probe size), high-current mode (large electron probe current), depth-of-focus mode (small convergence probe angle), and low-voltage mode (low accelerating voltages) [7]. In the study presented here, the samples were analyzed in resolution mode (10-30 kV). Specifics used in obtaining the best quality images are described in the associated Experimental section (Chapter 3).

2.1.2.2 Sample preparation

Diatom slides were sputter-coated with gold (approximately 2 nm in thickness) and mounted on a SEM stub using double-sided carbon tape for increased conductivity. Diatom frustule pore sizes and arrangements were examined using a SEM (FEI Quanta 200 SEM) shown in Figure 4, equipped with a tungsten filament operated at 30 kV. Similar uncoated diatom samples were studied via ambient indentation (described in the following section), with SEM images produced for analysis of frustule morphology.

Figure 4. Scanning electron microscope FEI Quanta 200 SEM used in this study. *Courtesy of* FEI.

The SEM images collected allowed creation of a detailed record of the diatom frustule dimensions, which were fundamental for creation of realistic 3D diatom models described further below.

2.1.2.3 Analysis of SEM images: dimensions and topography

The interpretation of SEM images is conducted mainly by direct observation of the images generated in the modes mentioned in the previous section. Although it can be assumed than the topographic description of the sample is evident, the features and image resolution of the sample rely in a thorough knowledge of the parameters involved in the setup of the SEM.

The level of detail obtained (pore diameter, number of pores) permitted a good representation of a diatom frustule via 3D modeling.

2.1.3 Ambient nanoindentation

This technique has its origins in Mohs [8] hardness scale, and it has gained considerable attention in the last two decades to become a standard method to characterize the mechanical properties of different type of materials.

Assumptions: The method developed by Oliver and Pharr was used in this section to calculate the mechanical properties of diatom frustules via ambient nanoindentation. This approach is based on the Sneddon relationship that assumes that for an arbitrary punch profile there is a power relationship between the penetration on a sample and the total force necessary to create it. The unloading region of the load vs. displacement curve is linearly fitted and the slope of this fitting determine the elastic properties of the sample as reported for several porous, and biomaterials. It was assumed that the quality of the data obtained was appropriate to obtain a good fitting and the elastic modulus obtained was within data reported for different species of diatoms.

2.1.3.1 General description

Similar to indentation tests, ambient nanoindentation is a method to calculate the mechanical properties of a material by indenting it with a calibrated indenter (of known geometry and properties) at a defined penetration depth (nm in the case of nanoindentation).

Contrary to the indentation approach of calculating the contact area via optical microscopy, in nanoindentation tests the area of contact between the sample and the indenter is calculated indirectly due to the small size of the impression.

Commonly, a nanoindenter is composed of a motion system or motor, an optical microscope, an indenter head, a computer, and an isolating case as shown in Figure 5.

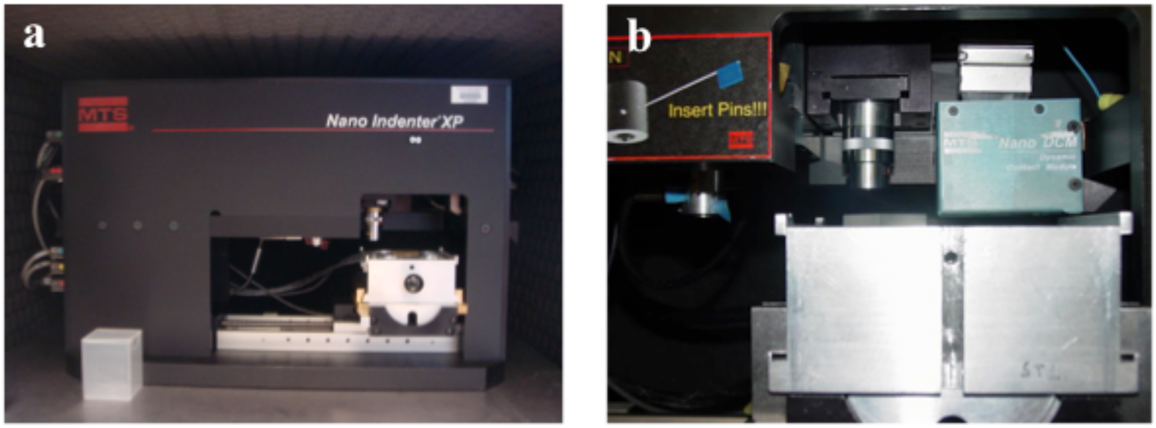

Figure 5. MTS Nano Indenter® XP utilized in this study (*a*), and close-up of the camera and indenter holder (*b*). *Courtesy of* MTS.

2.1.3.2 Sample preparation

Diatom samples were prepared as described previously for the optical analysis. To ensure the diatom sample was on a flat surface prior to any ambient nanoindentation, the glass slide was attached to cured casting resin holders using mounting adhesive (Ted Pella CrystalbondTM 509). It was important to ensure that all the frustules on the same glass slide had similar heights, as the nanoindenter is very sensitive to height variation, which affects the correct measurement of the *p-h* curves.

Assumptions: There were two main assumptions related to this procedure. First, all of the diatom samples that were placed on a metallography stub were assumed to be at the same height (i.e. a similar indentation depth was accomplished). Second, the diatom samples were fixed in place, that is, they did not displace in the *x*- or *y*- direction (sliding) before, during, and after each indentation was performed (i.e. ensuring that all indentations were carried out under similar loading conditions).

2.1.3.3 Analysis of mechanical properties: load vs. displacement curves

Ambient nanoindentations were performed using a MTS Nano Indenter® XP equipped with a diamond Berkovich indenter tip (radius: 20 nm, Young's modulus: 1,141 GPa and Poisson's ratio: 0.07 [9]). In an effort to identify the maximum load that could be applied on the diatom, a method of G-series continuous stiffness measurement (CSM) standard hardness, modulus, and tip calibration was used, in which a maximum vertical displacement of 200 nm was defined. The allowable drift rate was set to be 0.05 nm/s before nanoindentation was initiated. Surface approaching velocity was 10 nm/s. A maximum load range of 10 to 30 μN was identified from the CSM method. Subsequently, a G-series basic hardness and modulus load control method was applied to obtain load vs. displacement (*p-h*) curves for different diatom frustules. The peak-load holding time was 10 seconds. Key mechanical properties, such as Young's modulus E and hardness H, were calculated from the unloading portion of the *p-h* curves via the Oliver-Pharr relationship [9] (Figure 6), using the software Dureza [10]. A Poisson's ratio of 0.17 was used for the diatom frustule, as previously reported [11]. When the AFM tip geometry and related parameters are known, both H and E can be calculated via Equations 1 and 2 [9], where H is determined by P_{max} (the peak indentation load) and A (the nanoindentation contact area), E_r is the reduced Young's modulus and S is the slope of the unloading curve.

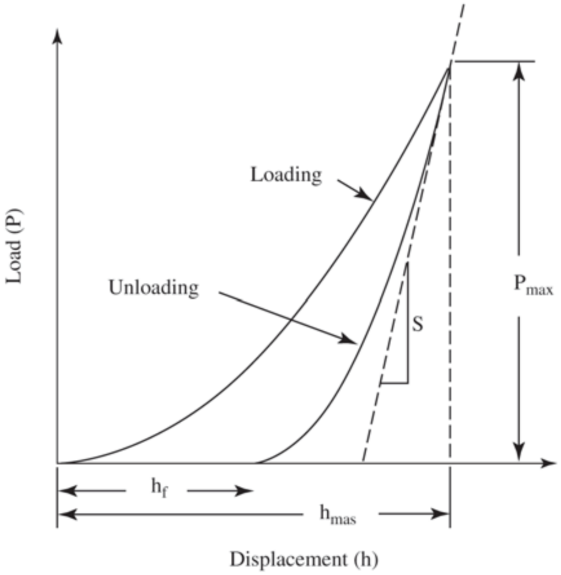

Figure 6. The indenter load-displacement plot for material indentation test [9].

$$H = \frac{P_{\max}}{A} \qquad \text{Equation 1}$$

$$E_r = \frac{\sqrt{\pi}}{2}\frac{S}{\sqrt{A}} \qquad \text{Equation 2}$$

2.1.4 Atomic Force Microscopy (AFM) characterization and nanoindentation

Scanning Probe Microscopy (SPM) has become one of the most often used techniques to investigate forces and strains in small materials with nanometer resolution. Invented by Gert Binnig in the 1980s, AFM is one of the most common SPM methods, in which force interaction or tunneling current from a probe to a surface is calculated to create a surface map based on the morphology and material properties of the sample.

Assumptions: The method developed by Sader was used in this section to calculate the mechanical properties of diatom frustules via AFM nanoindentation. It was also assumed that most of the frustule area of the samples was parallel to the glass slide, avoiding nanoindentation approaches and imaging issues. Furthermore, diatom samples were permanently fixed, that is, they did not displace in the *x*- or *y*- direction before, during, and after each AFM nanoindentation was performed.

2.1.4.1 General description

An atomic force microscope is composed of an AFM cantilever, a sharp tip, piezoelectric scanner, and operator controls as shown in Figure 7. The working principle of AFM is the recording of the probe-sample interaction as displacement of the probe on the surface of the sample, and associated short- and long-range forces. The forces that play a key role in the AFM displacement when the tip is close to the sample surface are the Coulomb (short range) and van der Waals (long range) forces. The Coulomb repulsive forces are created between the electron cloud of the tip and the sample surface, growing as the tip gets closer to the sample surface. Inversely, the van der Waals forces are important at larger tip-sample separation ($\geq$ 10 nm) [12].

AFM tests can be performed in one of the three main modes: contact, tapping and non-contact mode. The contact mode is mostly used to scan rough samples with large topographical variation in depth. This mode allows rapid scanning, with some loss of resolution due to the involvement of lateral forces. In comparison, AFM experimentation using tapping mode results in increased lateral resolution at a slower scanning speed. Finally, AFM tests in non-contact mode permit analysis of very soft samples with minimal damage [12].

2.1.4.2 Sample preparation

Upon successful sample preparation as previously described, diatom frustules were placed on pre-cleaned glass slides and imaged in air and in intermittent contact (tapping) mode using a Solver NEXT (NT-MDT) microscope as shown in Figure 7, and Bruker NCHV-A probes (Figure 8), with length (L) 125 µm, width (b) 42 µm, thickness (t) 3.5 µm, and fundamental resonance frequency (ω_f) 320 kHz, as reported by the manufacturer and verified via optical and electron microscopy.

Assumptions: It was assumed in this procedure that experimental conditions (i.e. humidity, sound vibrations) were constant during each imaging or nanoindentation session, which allowed minimum extra calibration of the AFM instrument between measurements of several frustules.

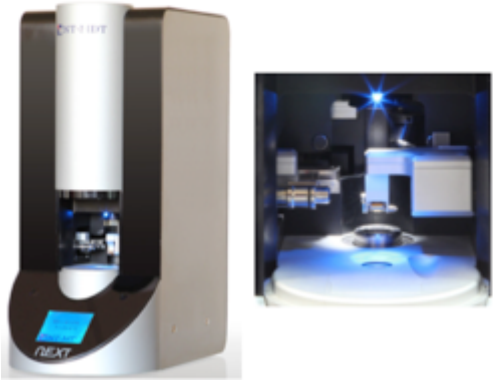

Figure 7. Atomic Force Microscope NT-MDT Solver Next used to gather images and force-distance curves. *Courtesy of* NT-MDT.

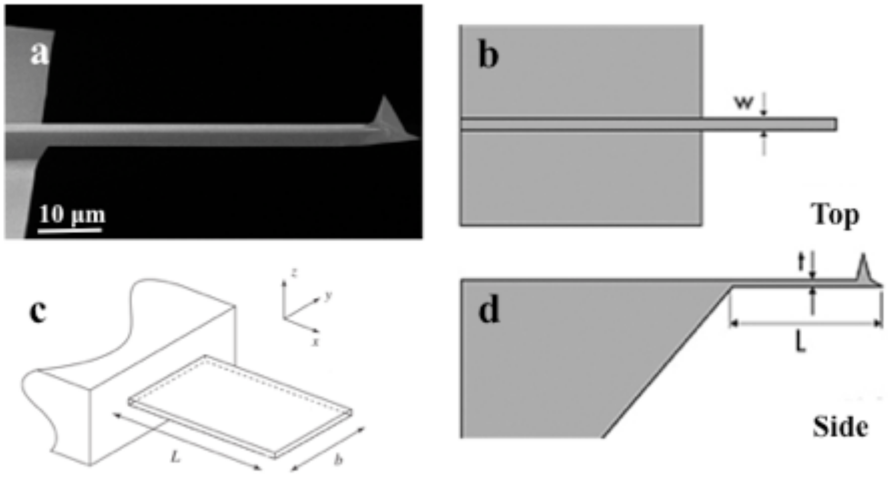

Figure 8. SEM image of a Bruker AFM cantilever (a), displaying the dimensions utilized for its calibration: width *w* (b), length *l* (c and d), and thickness *t* (d). *Courtesy of* Bruker AFM probes.

The cantilevers used were calibrated using two separate methods. The first method consisted of measuring *L* and *b* via optical imaging, calculating ω_f of the probe in air, and obtaining the quality factor (Q_f) of the fundamental mode of the cantilever. Equation 3 was then used to calculate the spring constant of the cantilever (*k*) as described by Sader *et al.* (Eqs.18-20) [13], which states that *k* of a rectangular cantilever is given by:

$$k = 0.1906 * \rho_f * b^2 * L * Q_f * \Gamma(\mathrm{Re}) * \omega_f^2 \qquad \text{Equation 3}$$

where ρ_f is the density of the fluid, and $\Gamma_i(\mathrm{Re})$ is the imaginary component of the hydrodynamic function Γ, which is only dependent on the Reynolds number, Re. The second method used was developed by Meyer *et al.* [12] and requires measuring similar parameters as the previous method, as well as thickness *t*. This method primarily uses Equations 4 and 5 to obtain the spring constant (*k*) of the AFM probe.

$$k = \frac{E_c \omega_f t^3}{4L^3} \qquad \text{Equation 4}$$

$$t = \frac{2\sqrt{12}\ \pi}{1.875^2}\sqrt{\frac{\rho_f}{E_c}}\omega_f L^2 \qquad \text{Equation 5}$$

After calculating the spring constant of the cantilevers, less than 5% deviation was found between the two methods. Additionally, spring constant values fell within the range reported by the manufacturer (within 14% of the nominal value). In this study, the Sader method (Eq. 3) was selected due to its lesser complexity for the calibration of the force-displacement curves described further later in this chapter.

2.1.4.3 Analysis of AFM images and depth profiles

AFM intermittent contact (tapping) mode imaging in air were carried out to establish morphological parameters of diatom structures such as pore depth, at the nanometer scale.

AFM imaging in air was accomplished separately by mounting clean diatom samples on a glass slide (using the same procedure as described for optical analysis) and imaging using a NT-MDT Solver Next AFM microscope. The probes used were purchased from Bruker NCHV-A with a spring constant of 42 N/m and resonant frequency of 300 kHz.

Several sections of the frustule were scanned to account for radial or longitudinal variations in the imaging results. First, larger areas were scanned (20 µm x 20 µm) in order to localize important features of the frustule, then smaller areas (5 µm x 5 µm) were scanned within the first selection to investigate fine details at higher resolution (slower scan speeds).

2.1.4.4 AFM nanoindentation measurements: load vs. displacement curves

First, AFM imaging was conducted in tapping mode by positioning the probe of an AFM microscope on top of a specific diatom frustule, and approaching the probe to the top frustule until the frustule-probe separation reaches the predefined initial value. A large scan area (e.g. 20 µm x 20 µm) of each top frustule was first obtained as a preview AFM image, in order to more efficiently select an optimum subarea(s) of the frustule morphology for nanoindentation. Once the best indentation area of a frustule was selected, several nanoindentation tests were performed to determine the most adequate voltage (and thus indentation force) that would produce the desired displacement without permanent failure. After a sequential nanoindentation-imaging procedure, the final nanoindentation force was set to 2.5 volts (corresponding to 10 nN). Each AFM indentation thereafter was accomplished by moving the AFM tip into the top frustule surface along the vertical axis (*z*-axis), until the piezoelectric material deformed and the corresponding cantilever deflection value (predefined by the voltage applied) was reached. A voltage vs. cantilever deflection curve was recorded for each individual indentation. The voltage-deflection curves were converted to load vs. tip-sample displacement profiles using the calculated sensitivity *s* (Eq. 6) and calibrated *k* values (Eq. 3) of the AFM equipment and the calibrated value of *k* together with JPK SPM Data Processing Software (JPK Instruments AG). Once a set of AFM indentations was successfully completed on a given diatom frustule, additional indents were performed on a standard glass slide to determine the sensitivity *s* (in nm/V) of a hard surface. The Young's modulus *E* of each diatom frustule was calculated using the retracting curve technique (Eq. 6-10) [13], defined by the slope in the linear region of the conventional load-tip-to-sample displacement profile (retracting part) as described below.

After a set of AFM indentations was successfully completed on a given diatom frustule, additional indents were performed on a standard glass slide to determine the sensitivity *s* (in nm/V) of the AFM equipment, which is defined by the slope of the increasing linear region of the retracting curve (Equation 6).

$$s = \frac{\Delta I_{PSD}}{\Delta Z_p} \qquad \text{Equation 6}$$

where I_{PSD} is the photodiode voltage, and Z_p is the *z*-position of the piezoelectric translator. The cantilever's deflection Z_c is obtained using the photodiode voltage and sensitivity *s* (Equation 7).

$$Z_c = \frac{I_{PSD}}{(\Delta I_{PSD} / \Delta Z_p)} \qquad \text{Equation 7}$$

The applied force *F* on the sample (e.g. a diatom frustule herein) is determined via Equation 8, as the spring constant of the AFM cantilever k_c was defined in previous AFM calibration.

$$F = k_c * Z_c \qquad \text{Equation 8}$$

The tip-sample separation *T* is calculated using Equation 9. For cases prior to any contact, $T = Z_p$ as there is no deflection on the cantilever.

$$T = Z_p + Z_c \qquad \text{Equation 9}$$

In the contact region, the Hertz model (Equation 10) is used to describe the tip-sample interaction, where δ represents the penetration depth, E is the reduced Young's modulus (accounting for both the sample and the tip properties as reported previously [14]), R is the tip radius, and v is the Poisson's ratio of the sample.

$$F = \delta^{\frac{3}{2}} * 2 * E * \frac{\sqrt{R}}{3 * (1 - v^2)} \qquad \text{Equation 10}$$

Once the displacement and F (Eq. 8) are determined, the Hertz equation (Eq. 10) can be used to calculate the Young's modulus of the diatom. In this study, the spring constant of the cantilevers used was k = 42 N/m.

2.2 Simulation section

The combination of modeling and computer simulation enhances the understanding of the macroscopic behavior of materials by analyzing their structures and dynamics at different length and time scales. Computer simulations have been demonstrated to provide valuable analysis capabilities for studying materials in engineering and science. Because of the complex, expensive and time-consuming process of prototyping, computer simulations have been helpful in creating models that can be easily analyzed and modified iteratively. These analyses provide important information about unique material structure and properties.

This section was mainly designed to investigate the mechanical response of diatom frustules to varied conditions and structural parameters not easily available via experiments.

Justification of methods: The use of FEM simulations allows the study of a complete diatom frustule due to its capabilities to represent intricate 3D models with different length scales (micron and nanoscale) of interest. Other simulation methods such as molecular dynamics are not as efficient computationally to reproduce the mechanical behavior of structures at the micron scale.

2.2.1 Diatom model creation: Computer-Aided Design (CAD) software

SEM images previously obtained of the diatom frustule were used for creation of precise 3D diatom models via CAD modeling software Pro/ENGINEER Wildfire version 4.0. Real diatom frustules in nature are made of two dome-shaped structures (or valves) joined together as the two parts of a "Petri dish". Each 3D CAD diatom model was first simplified to include only the top flat-shaped valve of each frustule with key features (e.g. pores), to reduce the computational cost (Chapter 3). 2D models of the contour of diatom frustules were first created with dimensions measured from SEM images, and extruded to the appropriate diatom height. The resulting solid 3D models were then hollowed, and pores and slits were added as per the SEM micrographs, to allow evaluation of structure-property relations and property variation between diatom species. The porosity for a given diatom frustule was calculated using Equation 11, determined by A_{empty} (empty area per pores, top of diatom model) and A_{total} (total area, top of diatom model). Here also, d is the pore diameter, D is the diatom frustule diameter, and N is the number of pores.

$$\%Porosity = \frac{A_{empty}}{A_{total}} * 100 = \frac{Nd^2}{D^2} * 100 \qquad \text{Equation 11}$$

2.2.2 Finite Element Method (FEM) simulation

Subsequently, enhanced dome-shaped 3D frustule models were created using shell models for computational efficiency, in order to investigate the role of hierarchical structure on the mechanical properties of the centric diatom. Each porous (shell) layer was successively joined with two other similar layers via “I-beam” structural units [5], to represent a real hierarchical frustule structure as specified by SEM. In this study, each 3D CAD diatom model included the large frustule valve only (called epitheca), with specific dimensions as reported independently [5], for computational efficiency. The resultant 3D CAD diatom frustule model was composed of one dome-shaped top valve surface (epitheca) containing a hierarchical assembly of three porous siliceous layers. This 3D hierarchical model of a real centric frustule was used in this study to investigate microstructure-property relations via simulations, to compare data with those available in the laboratory, and to predict other properties not readily accessible otherwise.

2.2.2.1 General description: computational mechanics methods

Computational mechanics is a subcategory of computer science, which is used to investigate phenomena ruled by the principles of mechanics, utilizing computational techniques. The importance of computational mechanics lies in the use of computers for solving complex mechanical analysis problems within a reasonable timeframe. Computational mechanics methods are an efficient and robust alternative for solving problems where analytical approaches are difficult to apply, or when experimental requirements are complicated to satisfy. However, because of this computational dependence, these methods have limitations when complicated computational models are investigated, resulting in large computing times and potential calculations inaccuracies (Appendix B).

Several computational mechanics methods are broadly used in numerous fields including aerospace, electronics, automotive and nuclear, and for examining phenomena such as solid and structural mechanics, fluid flow analysis, heat transfer, and biomechanics.

Among the most common computational mechanics methods are the Finite Volume Method (FVM), Finite Difference Method (FDM), Boundary Element Method (BEM) and Finite Element Method (FEM).

2.2.2.2 Finite element method

FEM has been widely used to analyze large models with relative long time durations, where the primary goal is to investigate the behavior of materials and processes at the macro level. This technique has traditionally been utilized in the macroscale regime, where the majority of science and engineering challenges arise, although it has been successfully applied to mesoscale problems as well.

2.2.2.2.1 FEM definition

FEM is an approximated numerical technique broadly used for solving boundary value problems that include a large variety of systems in engineering. The term “Finite Element Method” was first introduced in 1960 by Prof. Ray Clough, and later documented by Prof. O.C. Zienkiewicz [15]. Originally proposed as an analytical procedure for evaluating elastic-plastic plane stress of 2D structures [16], the FEM technique is currently used for analyzing a broad range of phenomena in multiple dimensions.

Since its early development, the FEM has been an indispensable tool for engineers and scientists for analysis of structural problems. Among its applications are thermal and mechanical analysis of bio-devices, electronics chips, microfluidic devices, aircraft parts, and electromagnetic analysis of antennas [17].

The basic approach of the FEM procedure is the segmentation of the system into a non-overlapping but continuous set of elements, solving the governing equations for each element, and then assembling the elemental results to approximate a global solution [18]. To accomplish this, FEM uses variational methods to solve the boundary value problem. The most common variational methods used for approximating a solution of boundary value problems are the Ritz method and the weighted residual methods. The most commonly use weighted residual methods are the Galerkin, least squares and collocation methods, with the first being the most extensively adopted.

The procedure for applying the FEM on a boundary value problem can be broadly summarized as consisting of four principal components: discretization and development of governing equations, assembly of element equations, application of boundary conditions, and calculation of primary unknowns and derived variables (Appendix C).

In the discretization and development of governing equations, the problem domain is discretized into a set of non-overlapping elements with defined shape and size to form a mesh or grid. The governing equations are developed for each element by using the physics of the problem, and typically Galerkin's Method or variational principles. Subsequently, in the assembly of element equations, the governing equations for each element in the mesh are assembled into a set of global equations. The global equations model the properties of the entire system. Next, the boundary conditions of the system are evaluated. The boundary conditions represent specific values that satisfy the variables of interest in the system. By defining the boundary conditions, the global equations are modified. Lastly, the global equations are solved for the primary unknowns at the nodes and the derived variables are calculated using the nodal values of the primary variables.

FEM allows performance of multidimensional analysis of a phenomenon, given certain conditions. The dimensional space is selected depending on the phenomenon of interest and the properties to be calculated. The most realistic representation, and also the most computationally expensive, is 3D analysis. This analysis is made when a phenomenon is occurring in all three coordinate directions of the system domain. 3D analysis is usually applied to intricate models or to phenomena with multidirectional implications such as mechanical analysis of aircraft components.

2.2.2.2.2 Structural mechanics via FEM

The FEM is a robust tool for solving problems in structural mechanics and determining relevant properties. Following the division of the problem domain, the elemental units may possess physical properties such as density, Young's modulus and Poisson's ratio.

Once the FEM simulation has been completed, several calculations can be performed for analysis of the FEM results. Among the most common outputs calculated using the FEM are von Mises stress, strain energy and displacement (Appendix D).

2.2.2.2.3 Mechanical analysis methods

The FEM includes flexible capabilities for displaying results in 2D and 3D plots, and allows controlling parameters for graphically tracking potential changes in variables of interest. Some of the most useful plots for analyzing mechanical properties with the FEM are stress-strain, von Mises stress, and total and partial deformation profiles in 3D.

2.2.2.3 Simulation setup and FEM-based software

A tetrahedral mesh was generated using the FEM software COMSOL Multiphysics version 4.3b, and a linear geometry solver was selected to capture small deflections of the diatom frustule upon compressive loads. On loading, the mesh was monitored until the stresses converged, with a final average mesh density ranging between 36,500-69,800 elements per µm^3 depending on diatom geometry and pore size, with a higher concentration of elements located at the top of a given frustule for improved accuracy. Various diatom frustules were simulated in the same way to ensure that the observed response was due to the load-diatom interactions and not to the imposed boundary conditions or possible meshing and convergence errors.

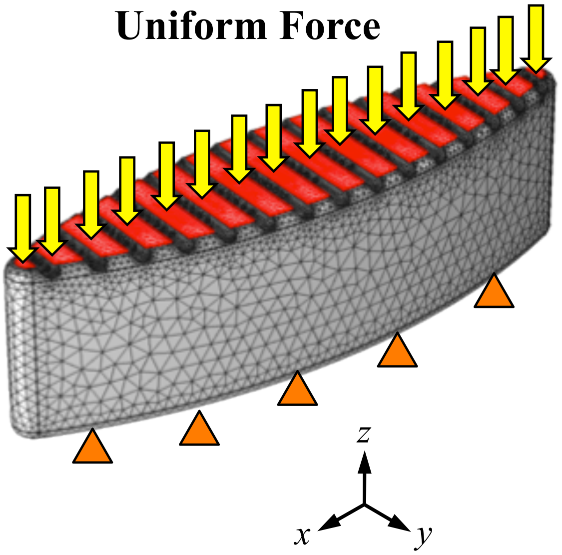

Figure 9. 3D *F. kerguelensis* diatom model displaying FEM hybrid tetrahedral mesh under uniform compression. The model had a finer mesh on the top of the diatom where the contact took place, while the bottom of the structure was fixed in all directions.

2.2.2.4 FEM nanoindentation simulations and experimental conditions

Experimental data (e.g. displacement) and nanoindentation simulations were first used to reproduce nanoindentation testing conditions and validate each calculated *p-h* curve for a given diatom frustule. 3D CAD diatom models were imported into FEM software COMSOL, and a Berkovich nanoindenter tip was modeled with a face angle of 65.27°. A quarter of the 3D model was simulated to decrease simulation time. The species-dependent Young's moduli of the diatom frustules obtained from nanoindentation experiments (e.g. average E = 16.6 GPa for the *Synedra sp.)* were used to uniquely define each model, as well as the reported Poisson's ratio. A contact pair was defined between the simulated indenter and the diatom model, allowing both materials to behave elastically. The mesh elements were set to be smaller in the diatom model than in the indenter to avoid convergence issues. A fixed boundary was applied at the bottom of the diatom model, while the top boundary of the indenter was set with a prescribed displacement as observed in the experimental data. The lateral boundary faces of the indenter were restricted from movement in the *x*- or *y*-direction to avoid shifting or sliding of the indenter. The resultant forces at the contact boundary were evaluated, and plotted versus the prescribed displacement of the indenter. Each calculated *p-h* curve was compared with its associated experimental *p-h* curve. The slope in the linear region of each *p-h* curve, between 0 and 20 nm displacement, was used for this evaluation to ensure that the purely elastic region was reproduced (see section 3.4.1).

2.2.2.5 FEM uniform compression simulations and post-processing analysis

Once the nanoindentation simulation *p-h* curves were validated against nanoindentation experiments, uniform compression simulations were performed on each diatom model (see section 3.4.2). These simulations allowed evaluation of relevant fabrication conditions for nanotemplates, e.g. uniform loading, where experimental data is not readily available due to manipulation and testing challenges. As before, SEM images and properties of experimental diatom frustules from ambient nanoindentation (*e.g.* average E = 2.33 GPa for the *Coscinodiscus sp.*) were used to distinctively define each diatom model. Complete 3D CAD diatom models, with top frustules only (epitheca), were created for uniform compression simulations using an appropriate mesh depending on the diatom species. 3D CAD diatom models were imported into FEM software COMSOL, and a uniform compressive experimental load was modeled with its corresponding maximum experimental displacement (*e.g.* 1.03 µm for the *Coscinodiscus sp.*). A fixed boundary was applied at the bottom of the diatom model to avoid shifting or sliding, while the top of the diatom frustule was set with a prescribed displacement similar to experiments. The lateral faces of the diatom model were unrestricted to allow deformation. It was assumed in this study that the uniform compression simulation methodology was validated via the experimental data and nanoindentation calculations (*e.g. p-h* curves). Mechanical properties such as the strain displacement and von Mises stress distribution were then analyzed for each diatom frustule as a function of porosity.

Analyses of the strain displacement and von Mises stress distribution were calculated within COMSOL via Equations 7-8 [16]. The strain displacement x is defined by equation 7 as the motion vector of each point within a solid, or $u\ [X,\ t]$, where u is the displacement vector, X is the initial position and t is time [16]. Von Mises stress σ_{mises} determined by equation 8 represents the multi-axial stress state of a solid described by the three principal stresses (σ_1, σ_2 and σ_3), and can be used as failure criteria when compared to the yield strength of a given material [16]. Hence, Equation 7 is used to calculate the strain displacement based on an initial position X, final position x, and time t, and Equation 8 calculates the maximum effective stress at a given point in a 3D model.

$$x = x(X,t) = X + u(X,t)$$ Equation 7

$$\sigma_{mises} = \sqrt{\frac{1}{2}(\sigma_1 - \sigma_2)^2 + (\sigma_1 - \sigma_3)^2 + (\sigma_2 - \sigma_3)^2}$$ Equation 8

2.3 References

1. Wang, D., Zhang, L., Lee, W., Knez, M. and Liu, L. Novel three-dimensional nanoporous alumina as a template for hierarchical TiO_2 nanotube arrays. *Small* **9**, 1025-1029 (2013).

2. Yao, H., Zheng, G., Li, W., McDowell, M., She, Z., Liu, N., Lu, Z. and Cui, Y. Crab shells as sustainable templates from nature for nanostructured battery electrodes. *Nano Letters* **13**, 3385-3390 (2013).

3. Li, D., Chang, P.-C., Chien, C.-J. and Lu, J.G. Applications of tunable TiO_2 nanotubes as nanotemplate and photovoltaic device. *Chemistry of Materials* **22**, 5707-5711 (2010).

4. Hasle, G.R. and Fryxell, G.A. Diatoms: Cleaning and mounting for light and electron microscopy. *Transactions of the American Microscopical Society* **89**, 469-474 (1970).

5. Losic, D., Pillar, R., Dilger, T., Mitchell, J. and Voelcker, N. Atomic force microscopy (AFM) characterisation of the porous silica nanostructure of two centric diatoms. *Journal of Porous Materials* **14**, 61-69 (2007).

6. Bogner, A., Jouneau, P.H., Thollet, G., Basset, D. and Gauthier, C. A history of scanning electron microscopy developments: Towards "wet-STEM" imaging. *Micron* **38**, 390-401 (2007).

7. Goldstein, J., Newbury, D., Joy, D., Lyman, C., Echlin, P., Lifshin, E., Sawyer, L., and Michael, J. Scanning electron microscopy and X-ray microanalysis, New York: *Springer* (2002). Print.

8. Samsonov, G.V. Handbook of the physicochemical properties of the elements. Springer (1968). Print.

9. Oliver, W.C. and Pharr, G.M. An improved technique for determining hardness and elastic modulus using load and displacement sensing indentation experiments. *Journal of Materials Research* **7**, 1564-1583 (1992).

10. Shuman, D.J., Costa, A.L.M. and Andrade, M.S. Calculating the elastic modulus from nanoindentation and microindentation reload curves. *Materials Characterization* **58**, 380-389 (2007).

11. Almqvist, N., Delamo, Y., Smith, B., Thomson, N., Bartholdson, A., Brzezinski, M., and Hansma, P. Micromechanical and structural properties of a pennate diatom investigated by atomic force microscopy. *Journal of Microscopy* **202**, 518-532 (2001).

12. Meyer, E. and Hug, H. Scanning probe microscopy: the lab on a tip. New York: *Springer* (2003). Print.

13. Sader, J.E. Frequency response of cantilever beams immersed in viscous fluids with applications to the atomic force microscope. *Journal of Applied Physics* **84**, 64-76 (1998).

14. Cappella, B., and Dietler, G. Force-distance curves by atomic force microscopy. *Surface Science Reports* **34**, 1-104 (1999).

15. Clough, R.W. Original formulation of the finite element method. *Finite Elements in Analysis and Design* **7**, 89-101 (1990).

16. Reddy, J.N. An introduction to the finite element method. New York: *McGraw Hill* (2006). Print.

17. Strang, G. and Fix, G. An analysis of the finite element method, Wellesley: *Prentice Hall* (1973). Print.

18. Bower, A.F. Applied mechanics of solids. Boca Raton: CRC / *Taylor and Francis* (2010). Print.

CHAPTER 3: AMBIENT NANOINDENTATION EXPERIMENTS AND FEM SIMULATIONS

From all previous studies, a variety of mechanical properties of biosilica diatom frustules based on nanoindentation have been reported. The challenges of measuring mechanical properties of diatom species experimentally are due to the differences existing between each species and sample preparation. A clear correlation between mechanical properties and diatom features (e.g., porosity, shape, thickness and pore size) has not yet been established. Therefore, robust modeling across different length scales is necessary to simulate the response of diatom frustules to deformation, in order to facilitate future biosilica nanotemplate designs and fabrication. Associated experimental testing is also required to validate the accuracy of the modeling.

3.1 Experimental evidence

Previously, mechanical analysis and characterization of diatom structures have been pursued using calibrated microneedles, ambient nanoindentation, and SEM imaging techniques.

Hamm *et al.* [1] investigated the frustules of *T. Punctigera* and *F. kerguelensis* using micro glass needle-loading tests, discovering an inverse relationship between the size of the frustule and the force required to break it. This unique behavior suggested that diatoms have evolved to "respond to predators, adapting their frustule architecture to improve their mechanical rigidity by supporting localized pressures without breaking".

In another study, Yao *et al.* [2] performed localized ambient nanoindentations on *Coscinodiscus sp.* diatom frustules at different incident angles to calculate their elastic modulus and hardness, finding low Young's modulus E (ranging from 0.59-2.77 GPa) and hardness values H (ranging from 0.03-0.12 GPa). The investigators reported that these mechanical properties were strongly dependent on the location of the indentation (independent of frustule size), and a good agreement with FEM simulations performed using similar experimental conditions.

3.2 Previous calculations

A FEM study of the mechanical response of *F. kerguelensis* diatom model to various loads revealed that high (tensile and compressive) stresses were localized within the girdle band region of the frustule [1]. These results indicate that this diatom species can use such protective armor against naturally occurring predators.

In a recent study, Garcia *et al.* [3] performed molecular dynamic simulations of diatom-inspired nanoporous materials, investigating the effect of hierarchical nanoporous layers under tensile deformation. The results in that study showed a significant enhancement of the mechanical properties of the material, including superior deformability compared to brittle silica glass. In addition, Yao *et al.* [2] performed FEM simulations on 2D and 3D sections of diatom frustule models and found good agreement with experiments using similar testing conditions.

The limited number of similar studies highlights the need to explore increased length scales via FEM analysis to calculate the properties of diatom frustules at the microscale.

3.3 Experimental section

3.3.1 Morphology analysis (before and after nanoindentation) via SEM

Several frustules from two specific diatom species (listed below) were selected and prepared for SEM as described before in the Methodology section (Chapter 2), and each SEM stub was mounted separately to ensure consistent characterization conditions.

<u>Assumptions:</u> SEM images of Synedra diatom species did not reveal pores between the ribs. The pores size, later revealed via AFM, was 100 nm and average SEM resolution is 10 nm. It was assumed that the pennate frustules were not explored enough in those areas rather than the pores were not present in the samples imaged with SEM. In addition, the cracks revealed on SEM images after ambient nanoindentations were assumed to be the result of the nanoindenter-sample interaction, despite not having taken SEM images before the nanoindentations. This assumption applied to both *Coscinodiscus* and *Synedra* diatom species.

3.3.1.1 Coscinodiscus sp.

Figure 10 displays representative SEM images of a *Coscinodiscus sp.* diatom frustule, emphasizing its ordered pore arrangement at the microscale. A hierarchical structure was observed in the *Coscinodiscus* frustules, displaying ordered pores of around 100 nm in diameter. These observations were in good agreement with previous independent studies on these diatoms [3-6].

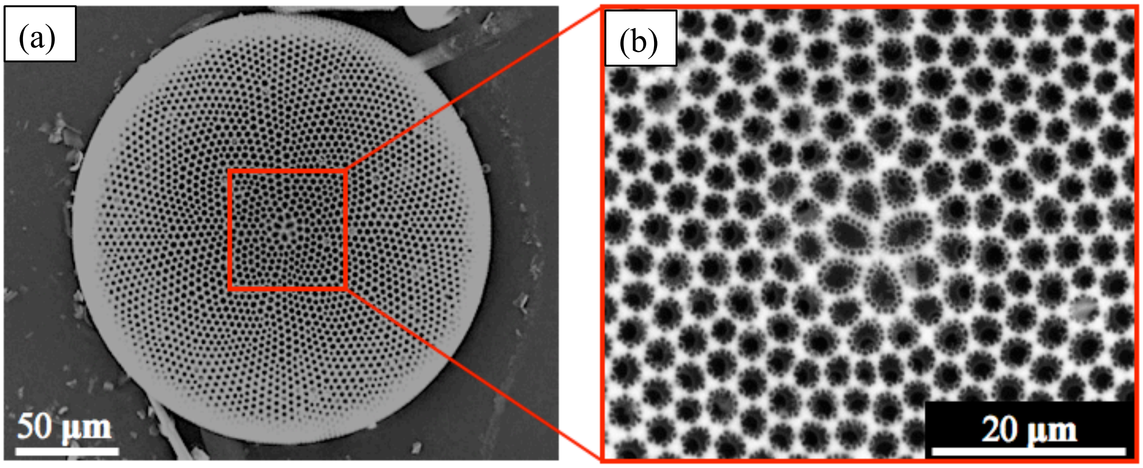

Figure 10. SEM micrograph of a characteristic *Coscinodiscus sp.* diatom frustule examined prior to nanoindentation experiments. The biosilica centric frustule (a) has a diameter ~200 µm and a highly ordered pore arrangement (b), which varies in size and orientation.

Upon completing selection and evaluation of various *Coscinodiscus sp*. diatom frustules, ambient nanoindentation testing was pursued on each frustule as described in the Methodology section (Chapter 2) [7-8], and subsequent SEM imaging was obtained for these diatom structures to evaluate their characteristics after ambient nanoindentation tests. Typical SEM images of some of these biostructures evaluated after nanoindentation are illustrated in Figure 11, highlighting different indentation marks found. Images show different types of indent marks resulting from selected nanoindentations: surface pits within two highlighted indentation areas (Fig. 11(*a*)), presence of an extended crack (Fig. 11(*b*), shown via red arrows), and multiple cracks and edge defects (Fig. 11(*c*)).

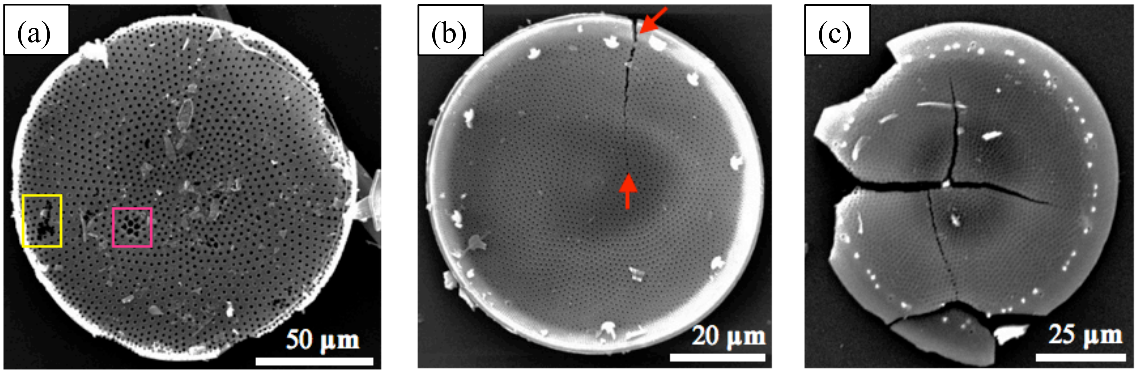

Figure 11. Representative SEM micrographs of *Coscinodiscus sp.* diatom frustules after nanoindentation experiments. Centric frustule images show different types of indent marks resulting from selected nanoindentations: surface pits within two highlighted indentation areas (*a*), presence of an extended crack (*b*), and multiple cracks and edge defects (*c*).

3.3.1.2 Synedra sp.

SEM images of elongated *Synedra sp.* diatom frustules were also taken prior to ambient nanoindentation experiments, revealing characteristic longitudinal slits and ribs with thicknesses of ~2 mm and ~3 mm respectively (Figure 12). The resultant dimensions and morphological features were consistent with prior reported studies [8-9], showing that those features are dependent on diatom species or frustule symmetry.

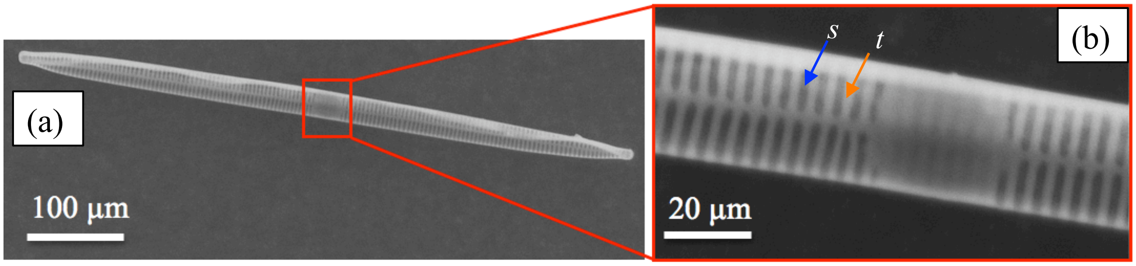

Figure 12. SEM micrograph of a characteristic *Synedra sp.* diatom frustule evaluated prior to ambient nanoindentation experiments. The pennate frustule (*a*) has a length *l* of ~600 μm, a width *w* of ~30 μm, and contains valve surfaces with distinct features such as lateral longitudinal slits (*b*) with a thin slit width *s* of ~2 μm (blue arrow) and a rib thickness (distance between slits) *t* of ~3 μm (orange arrow).

Similar as before, pennate *Synedra sp.* diatom frustules were examined using SEM after ambient nanoindentation testing was conducted on each frustule. Figure 13 shows some of the SEM images of these frustules obtained to identify their failure mode after nanoindentation tests.

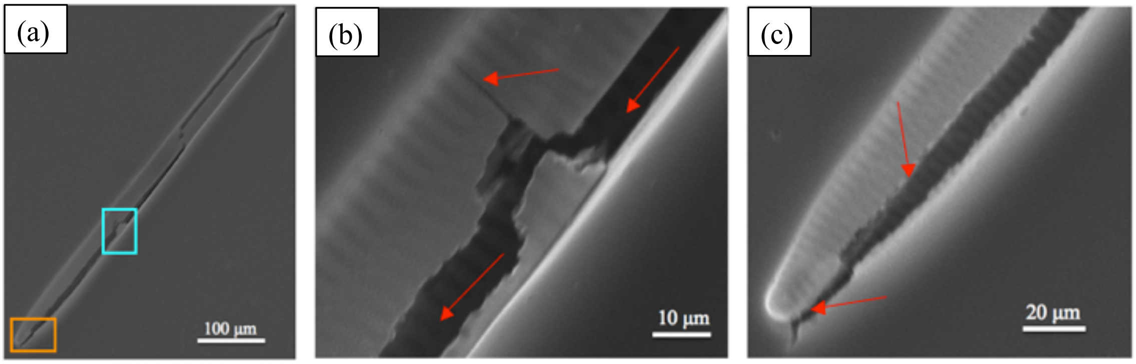

Figure 13. Selected SEM micrographs of a *Synedra sp.* frustule after ambient nanoindentation experiments (*a*, blue and orange boxes). The pennate diatom image (*a*) reveals a longitudinal crack (*b*) shown via red arrows, which extends until reaching one end of the frustule (*c*).

3.3.2 Ambient nanoindentation experiments

A set of diatom frustules per diatom specie was prepared as described in the Methodology section (Chapter 2) and each glass slide was mounted separately on the metallography stub to ensure consistent testing conditions.

As stated earlier, load-displacement (*p*-*h*) curves were measured and analyzed for each diatom nanoindentation to calculate mechanical properties such as the Young's modulus and hardness, using the Oliver-Pharr relationship [10].

Assumptions: Ambient nanoindentation on the centric and pennate diatom frustules in this study did not reach plastic deformation. In fact, all the indentation results were assumed within the elastic regime. In addition, the calculation of the Young's modulus followed the well-documented Oliver and Pharr method, which uses the Sneddon relationship that suggests a power correlation between the load and the indentation displacement created on the sample for several indenter geometries.

3.3.2.1 Load-displacement curves

3.3.2.1.1 Coscinodiscus sp.

Figure 14 displays representative *p*-*h* curves of *Coscinodiscus sp.* illustrating their low stiffness values compared with bulk silica glass (73.1 GPa). A summary of the experimental measurements for this diatom species is included in Table 1.

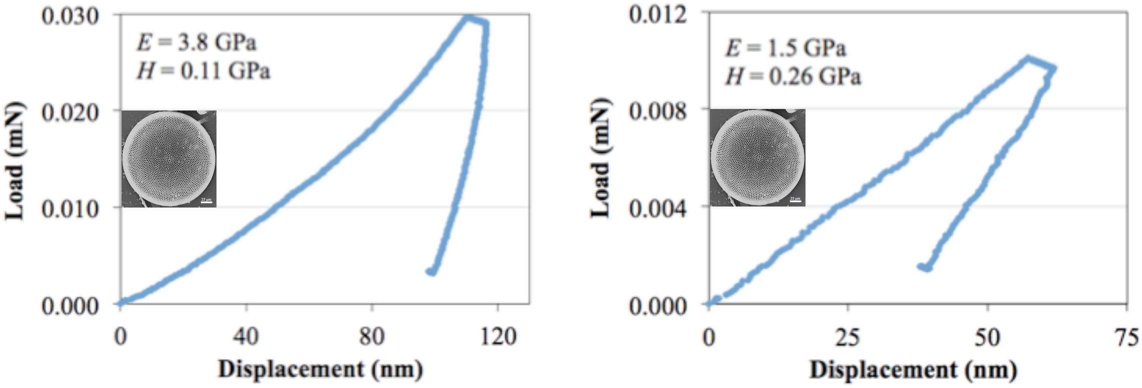

Figure 14. Two representative experimental determinations of Young's moduli for *Coscinodiscus sp.* diatom frustules, showing that values are low (average E = 3.1 GPa) compared to the value for bulk silica glass (73.1 GPa).

3.3.2.1.2 Synedra sp.

Load-displacement curves of *Synedra sp.* diatom frustules were also analyzed as shown in Figure 15. It is apparent that these elongated diatoms have ~5 times larger Young's moduli and hardness values than the centric diatoms (Figure 14), and such frustules display significantly less displacement upon nanoindentation tests than their centric frustule counterparts [7]. Table 2 shows the experimental measurements for the *Synedra sp.* diatom species.

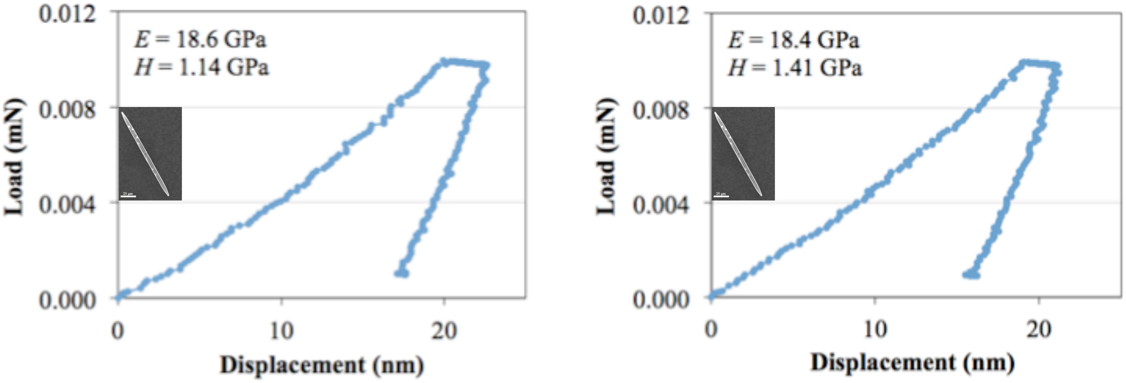

Figure 15. Two other experimental measurements of Young's moduli for *Synedra sp.* diatom frustules, displaying values significantly higher (average E = 16.6 GPa) compared to the *Coscinodiscus sp.* diatom frustules (Fig. 14).

3.3.2.2. Young's modulus measurements

The Young's modulus and hardness were calculated using the Oliver and Pharr method [10] described in the Methodology section (Chapter 2), and summarized in Table 1 for the *Coscinodiscus sp.* and Table 2 for the *Synedra sp.*

3.3.2.2.1 Coscinodiscus sp.

Table 1. Experimental data obtained from selected *Coscinodiscus sp.* diatom frustules.

Centric Frustule ID	E (GPa)	H (GPa)
C-2	3.8	0.11
C-6	1.1	0.11
C-12	1.5	0.26
C-13	5.6	0.10
C-14	1.7	0.23
C-20	6.2	0.34
C-21	10.6	1.03
Mean[#]	3.1	0.17
Standard deviation[#]	2.7	0.24

Average Young's moduli for *Coscinodiscus sp.* frustules: E_{avg} = 3.1 GPa. Mean$^{\#}$ and standard deviation$^{\#}$ denote values using a larger sample set. A load of 10 µN was applied.

3.3.2.2.2 Synedra sp.

Table 2. Experimental data obtained from selected *Synedra sp.* diatom frustules.

Pennate Frustule ID	***E* (GPa)**	***H* (GPa)**
S-28a	13.7	0.85
S-28b	15.7	1.08
S-28c	18.6	1.14
S-28d	18.4	1.41
Mean	16.6	1.12
Standard deviation	2.3	0.23

Average Young's moduli for *Synedra sp.* frustules: E_{avg} = 16.6 GPa. Mean$^{\#}$ and standard deviation$^{\#}$ denote values using a larger sample set. A load of 10 µN was also applied.

3.4 Simulation section

Assumptions: Experimental data and nanoindentation simulations were used to reproduce nanoindentation experimental conditions and validate the simulated indenter load-displacement curves, as reported elsewhere [7]. The nanoindentation simulation setup and simulated load-displacement curves were found in good agreement with experiments in the elastic region as described in the next section. It was assumed that a similar method is applicable for uniform compression experiments, also in the elastic region. In addition, the 3D diatom models created from SEM and AFM images were assumed to be a good representation of the epitheca of diatom frustules. Furthermore, the average mechanical properties obtained from ambient nanoindentations were considered a good representation of the mechanical properties of diatom frustules modeled.

3.4.1 Validation of simulation method using nanoindentation test conditions

As described in the Methodology section (Chapter 2), experimental data (e.g. displacement) and nanoindentation simulations were first used to mimic nanoindentation test conditions and validate the simulated indenter load-displacement (*p-h*) curves. SEM micrographs obtained from the diatom frustu1les studied were used for the creation of accurate 3D diatom models. The CAD diatom models were imported into the FEM-based software COMSOL Multiphysics version 4.3b, and a Berkovich nanoindenter tip was modeled to reproduce the tip-substrate interaction during nanoindentation tests. For efficient computation, only a section of the 3D diatom model was simulated. Each diatom frustule model was assigned the corresponding experimentally determined average Young's modulus to define it uniquely. The resultant *p-h* curves of the simulated models were monitored carefully for convergence and compared with the experimental measurements to verify their validity. Figure 16 illustrates a nanoindentation simulation setup and associated simulated *p-h* curve, in reasonable agreement with experiments in the elastic region. Since the nanoindentation simulations replicate well the nanoindentation conditions (i.e., localized compression), it is reasonable to assume that a similar method is applicable for other experiments such as compressive loading (e.g., uniform compression), also in the elastic region. Parameters were monitored carefully to ensure convergence of results, and a suitable mesh was used in uniform compression simulations of the 3D diatom frustule models.

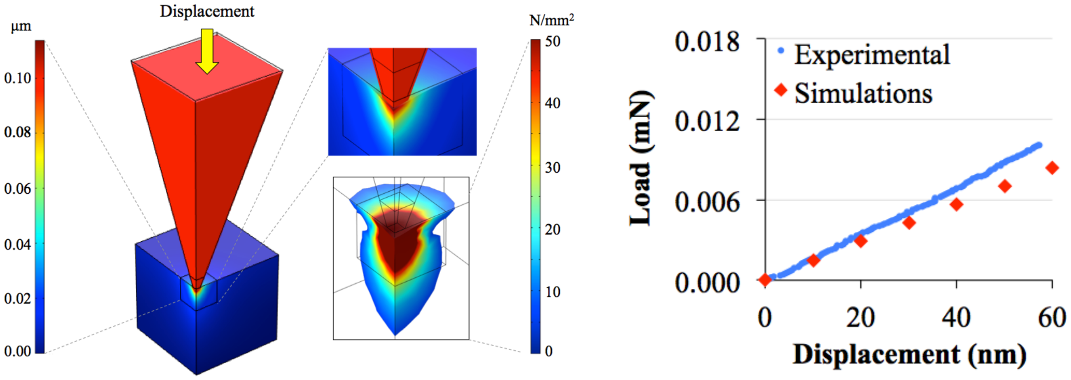

Figure 16. FEM nanoindentation simulation setup (left) and resultant validated load-displacement curve for a given *Coscinodiscus sp.* diatom frustule using experiments and simulations (right). Insets show close-up views of the (left, top) displacement and (left, bottom) stress distributions around the nanoindenter tip in the solid silica model. A similar simulated technique is used afterwards to reproduce uniform compression conditions where measurements are not readily accessible experimentally.

3.4.2 FEM uniform compression simulations

Mechanical response via von Mises stress and displacement distributions was analyzed for 3 specific epitheca diatom models (*Coscinodiscus sp.*, *Synedra sp.* and *F. kerguelensis*) upon uniform compression simulation as shown in Figures 17-28. In each case, a suitable 3D model of the diatom frustule as in nature was simulated first, with its measured dimensions from SEM images and E_{avg} (e.g. 22.4 GPa for *F. kerguelensis* [1]). Next, a "modified" diatom model was simulated with the largest pores or smallest slits depending on the diatom species, as suitable for templates.

3.4.2.1 Displacement distributions

To investigate the effect of diatom frustule morphology, *Coscinodiscus sp.* (Figure 17), *Synedra sp.* (Figure 19), and *F. kerguelensis sp.* (Figure 21) diatom models were created using SEM micrographs and their mechanical properties were analyzed upon uniform compression simulations. In addition, diatom models with larger pore size *d* were analyzed (Figs 18 and 22) to study the porosity effects on the structures mechanical integrity. Displacement distributions were evaluated for each diatom model under similar simulation setup.

3.4.2.1.1 Coscinodiscus sp.

The results illustrated in Figure 17 for *Coscinodiscus sp.* models show the extent of the displacement of the top surface, primarily in the center and decreasing radially outward toward the edge of the structure (top and side view). In addition, close-up views show detailed features of each distribution without displacement.

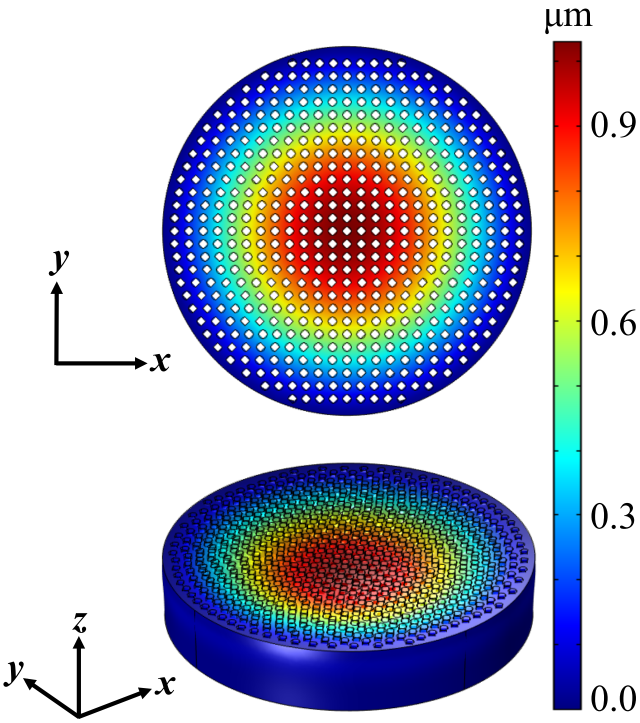

Figure 17. FEM uniform elastic compression simulation of *Coscinodiscus sp.* diatom models. Bottom figure shows a displacement distribution for frustules similar to those in nature (*D*=200 μm, *d*=4.8 μm) with a radial distribution with higher values localized at the center of the frustule. View above 3D model shows features of distribution without initial position.

Figure 18 shows the resultant properties using *Coscinodiscus sp.* diatom models with modified dimensions (*D*=200 μm, *d*=12 μm).

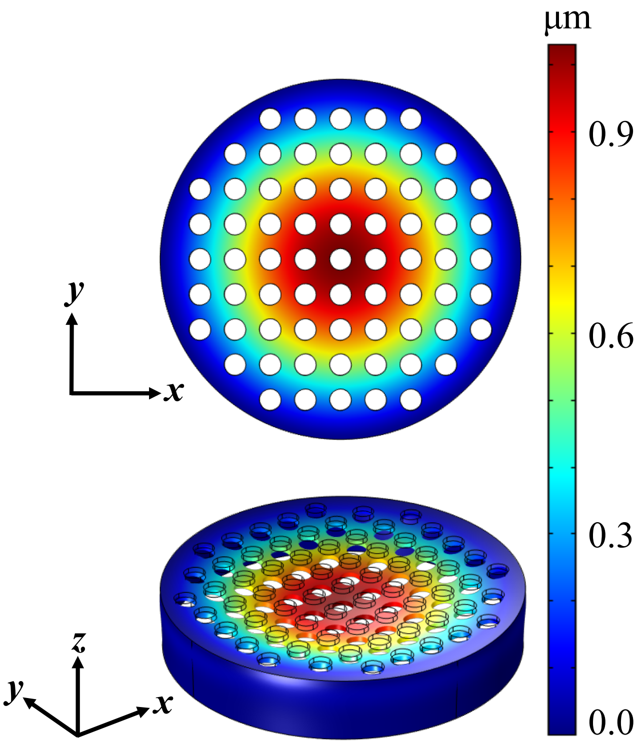

Figure 18. FEM uniform elastic compression simulation of *Coscinodiscus sp.* diatom frustules. Bottom figure displays a displacement distribution for a "modified" frustule when pore size *d* is increased, relevant for microtemplate applications (*D*=200 μm, *d*=12 μm). Results illustrate the extent of the displacement of the top surface, primarily in the center and decreasing radially outward toward the edge of the structure. Top view above 3D model shows detailed features elastic distribution without displacement.

3.4.2.1.2 Synedra sp.

Similarly, *Synedra sp.* diatom models were evaluated upon FEM uniform compression simulations. Results revealed this elongated frustule had higher stress concentrations at the top center of the valve, with a uniform distribution along the height of the structure decreasing from top to bottom. A similar diatom model with a smaller slit width was also evaluated for comparison. Similar displacement distributions are noted on these diatom models, mainly in the center of the top surface around ribs and decreasing toward the remaining structure (Figure 19, top and bottom).

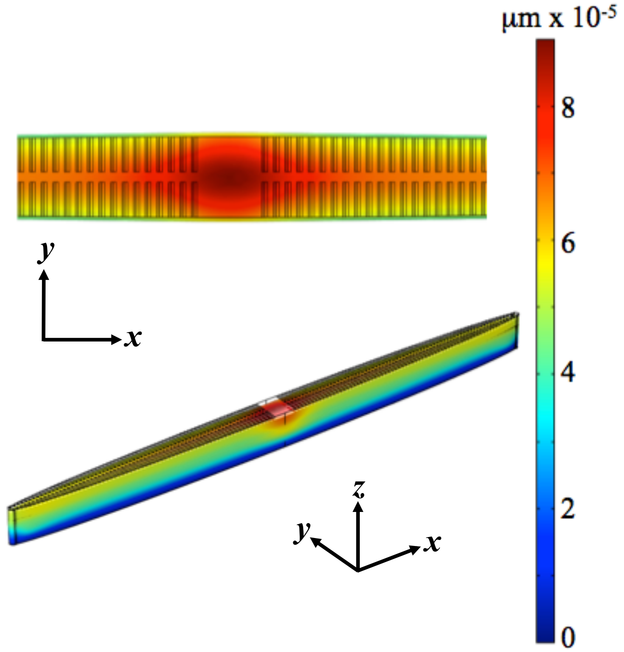

Figure 19. FEM uniform elastic compression simulation of *Synedra sp.* diatom models displaying displacement distributions. Bottom figure shows a displacement distribution of the top surface for frustules typically found in nature (*l*=162 µm, *w*=8 µm, *s*=0.54 µm, *t*=0.60 µm). Displacement distribution was noted mainly in the center of the top surface around ribs and decreasing toward the remaining structure. Close-up view above 3D model shows detailed features of distribution without initial position.

In addition, uniform compression simulations were pursued on pennate *Synedra sp.* diatom models created by modifying the original dimensions of the models as shown in Figure 20. The slit width was decreased (*l*=162 µm, *w*=8 µm, *s*=0.135 µm), while keeping the rib thickness constant (*t*=0.60 µm). As a result, there was substantial number of slits and ribs in these models.

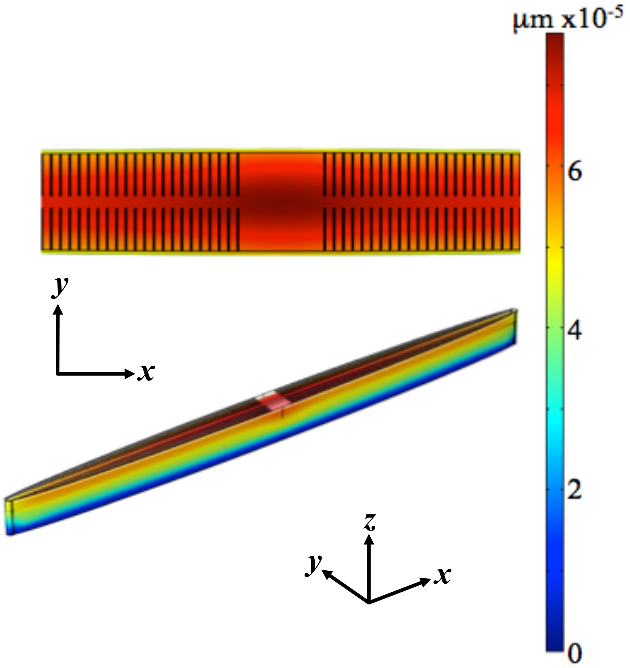

Figure 20. FEM uniform elastic compression simulation of *Synedra sp.* diatom frustules. The dimensions of the bottom model has been modified to evaluate the effect of decreasing slit width (*l*=162 μm, *w*=8 μm, *s*=0.135 μm), keeping the rib thickness constant (*t*=0.60 μm) and thus increasing the number of slits and ribs. Displacement distribution is similar as those found previously in Figure 19, mainly in the center of the top surface around ribs and decreasing toward the remaining structure. View above the 3D model shows features of the modified frustule.

3.4.2.1.3 F. kerguelensis

Lastly, the evaluation of the *F. kerguelensis sp.* diatom frustule model was pursued via FEM simulations to predict its mechanical properties as illustrated in Figure 21. Frustule models with dimensions and pore sizes as in nature and those with largest pore size were analyzed. The displacement distributions showed concentrated displacements at the top center of the frustule increased faster along the longitudinal axis than in the direction of the transversal axis.

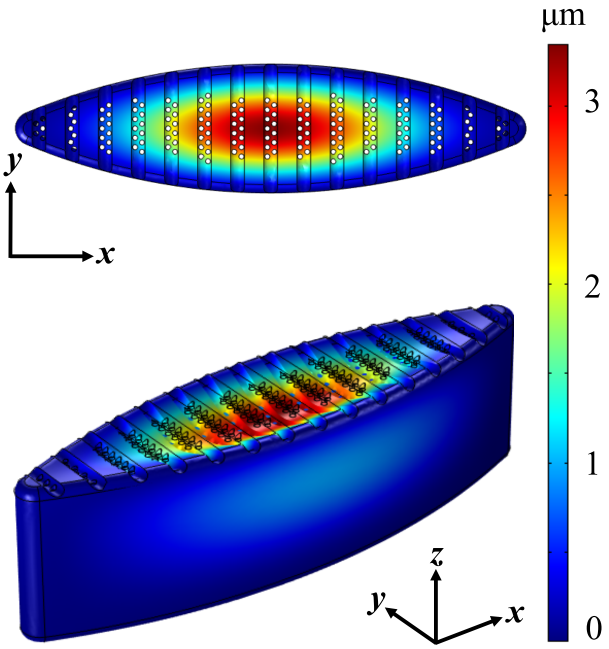

Figure 21. FEM uniform elastic compression simulation of pennate *F. kerguelensis* diatom models. Bottom figure shows a displacement distribution for a model with dimensions and pore sizes as in nature (*l*=30 µm, *w*=7.83 µm, *d*=0.3 µm) [1]. Close-up view (top) depicts structural details of a displacement distribution without initial position.

Results from *F. kerguelensis* diatoms with modified dimensions were analyzed (*l*=30 µm, *w*=7.83 µm, and *d*=0.7 µm) under uniform compression loads as shown in Figure 22.

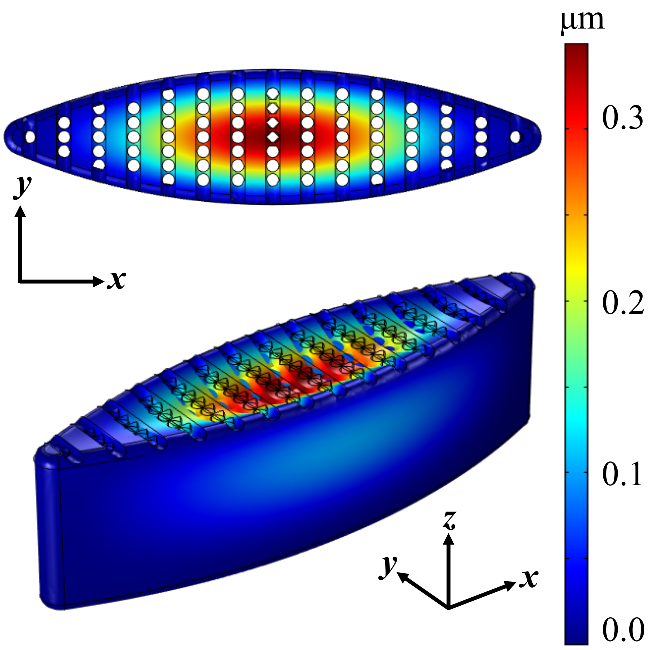

Figure 22. FEM uniform elastic compression simulation of pennate *F. kerguelensis* frustules. Bottom image shows a displacement distribution for a "modified" model with dimensions *l*=30 µm, *w*=7.83 µm, and pore diameter *d*=0.7 µm. Results indicated significantly lower displacement of the top surface compared to the equivalent model as found in nature (Figure 21), mainly in the center and decreasing toward the remaining structure. View above 3D model illustrates distribution details.

3.4.2.2 von Mises stress distributions

In addition to the displacement distribution analyzed in the previous section, the von Mises stress distribution was evaluated on 3D diatom models to understand their dependence on frustule morphology. Figures 23-28 show the corresponding von Mises stress distribution for the *Coscinodiscus sp.*, *Synedra sp.*, and the *F. kerguelensis* diatom models respectively.

3.4.2.2.1 Coscinodiscus sp.

The stress distribution of the centric *Coscinodiscus sp.* was evaluated on a frustule with identical dimensions as those found in nature (*D*=200 µm, *d*=4.8 µm). The stress values were modest in the center of the frustule surface. In addition, higher stress values were located around the edge immediately below the top face of the frustule as shown in Figure 23 (side view).

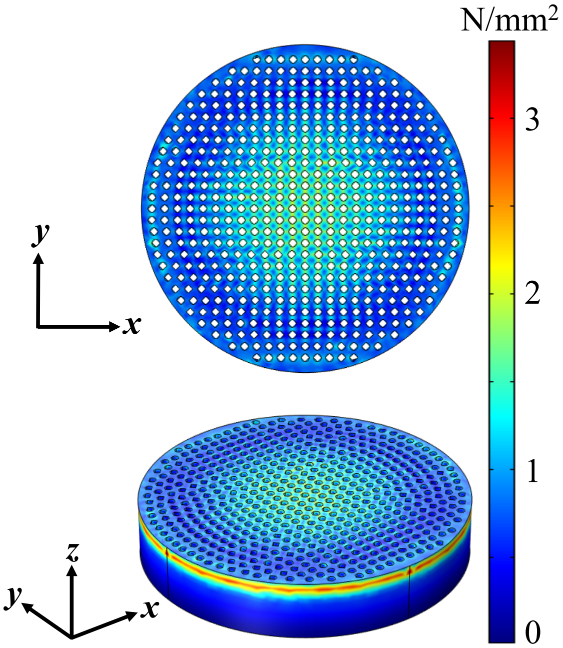

Figure 23. FEM uniform elastic compression simulation of *Coscinodiscus sp.* diatom models displaying stress distributions (top and side view) as those found in nature (*D*=200 µm, *d*=4.8 µm).

The stress distribution of a "modified" diatom model showed in Figure 18 was evaluated under uniform compression, obtaining a small stress distribution in the center of the diatom model (top surface). In addition, a well-defined circular ring around the girdle band of the structure was found.

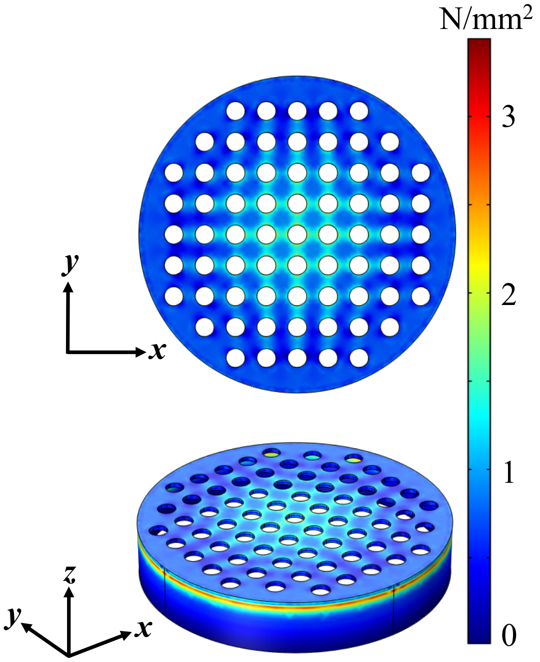

Figure 24. FEM uniform elastic compression simulation of *Coscinodiscus sp.* diatom frustules. The pore size *d* is enlarged (for "modified" diatoms), relevant for microtemplate applications (*D*=200 μm, *d*=12 μm). Results display a centric concentrated stress distribution on the top surface, and the highest stress values around the girdle band of the model.

3.4.2.2.2 Synedra sp.

Models of the pennate *Synedra sp.* frustule created with actual dimensions gathered via SEM imaging (*l*=162 μm, *w*=8 μm, *s*=0.54 μm, *t*=0.60 μm) were evaluated under compressive loads. On the top surface, larger stresses were located longitudinally and concentrated at the half of the width. Additionally, the larger stress concentration on the structure was located at the bottom side while decreasing in *z*-direction.

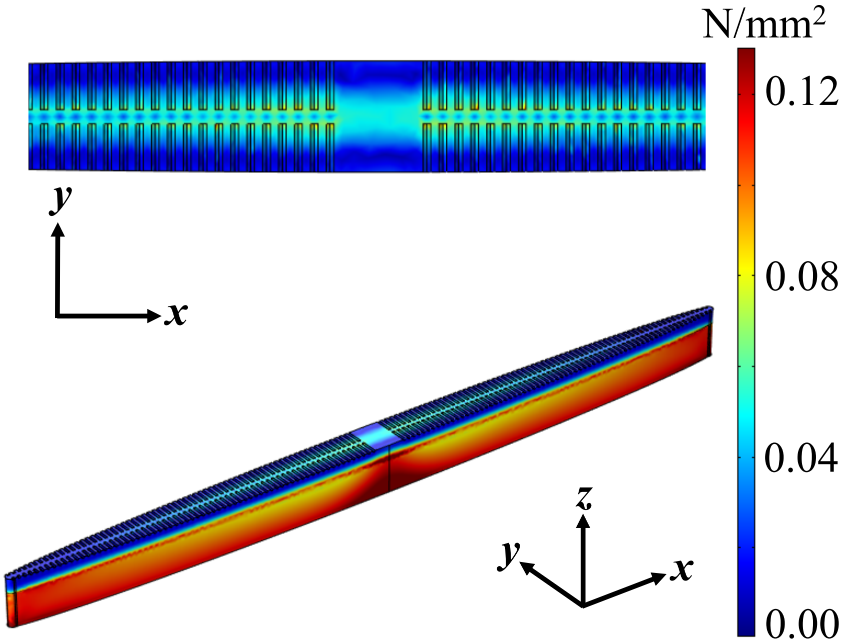

Figure 25. FEM uniform elastic compression simulation of *Synedra sp.* diatom models showing stress distributions of the top surface for frustules typically found in nature (*l*=162 µm, *w*=8 µm, *s*=0.54 µm, *t*=0.60 µm).

In Figure 26, a uniform stress distribution of a pennate *Synedra sp.* diatom is shown under compressive loadings. The dimensions of the model were modified as in Figure 20, keeping the rib thickness constant and decreasing the slit width. The stress distribution was found to be linear incremental along the *z*-axis from top to bottom.

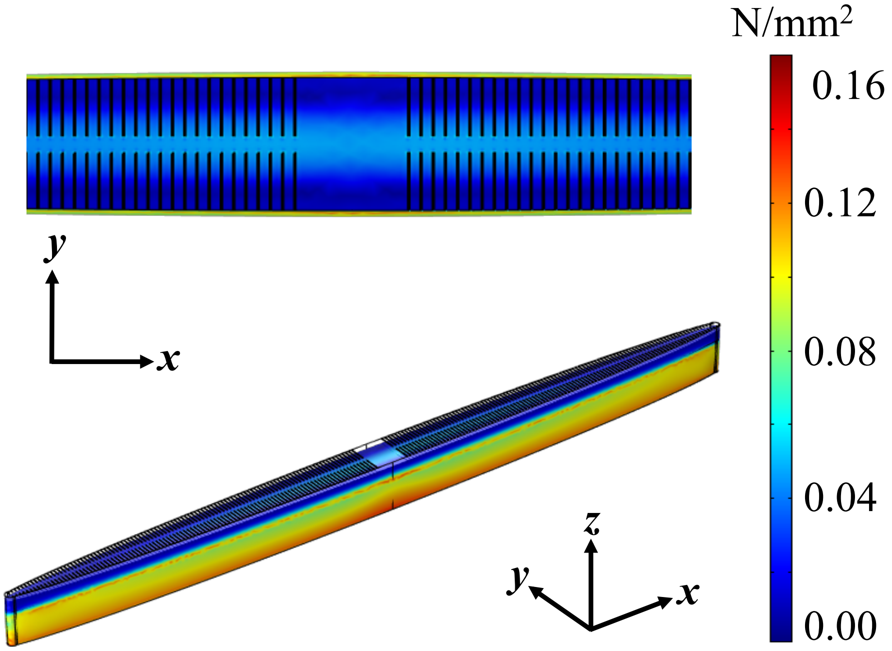

Figure 26. FEM uniform elastic compression simulation of *Synedra sp.* diatom frustules. It was observed low stress distributions in the "modified" diatom frustule top surface, while the higher stress concentrations were located at the bottom of the frustule. A close-up view of the top frustule showed a very uniform stress distribution. Dimensions of the "modified" frustule are: l=162 µm, w=8 µm, s=0.135 µm, and t=0.60 µm.

3.4.2.2.3 F. kerguelensis

Figure 27 shows stress distributions for models with dimensions and pore sizes as in nature (l=30 µm, w=7.83 µm, d=0.3 µm). The maximum stresses were located at the center and decreasing toward the remaining structure, which is similar to previous pennate diatom but with definitely higher stress values.

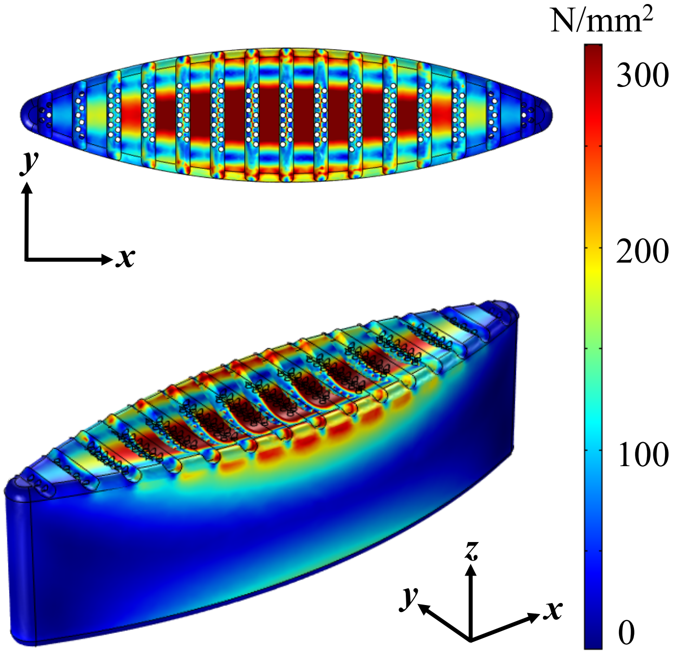

Figure 27. FEM uniform elastic compression simulation of pennate *F. kerguelensis sp.* diatom models for those found similarly in nature (l=30 µm, w=7.83 µm, d=0.3 µm) [1].

Results for the *F. kerguelensis* diatoms are presented in Figure 28, which shows the calculated properties using frustule models with modified dimensions (l=30 µm, w=7.83 µm, pore sizes d=0.7 µm). The higher stresses were mostly concentrated at the center of the top valve of the frustule and its edges. However, a medium range stress values of around 150 N/mm^2 were found at the bottom of the frustule where the fixed displacement boundary condition was enforced.

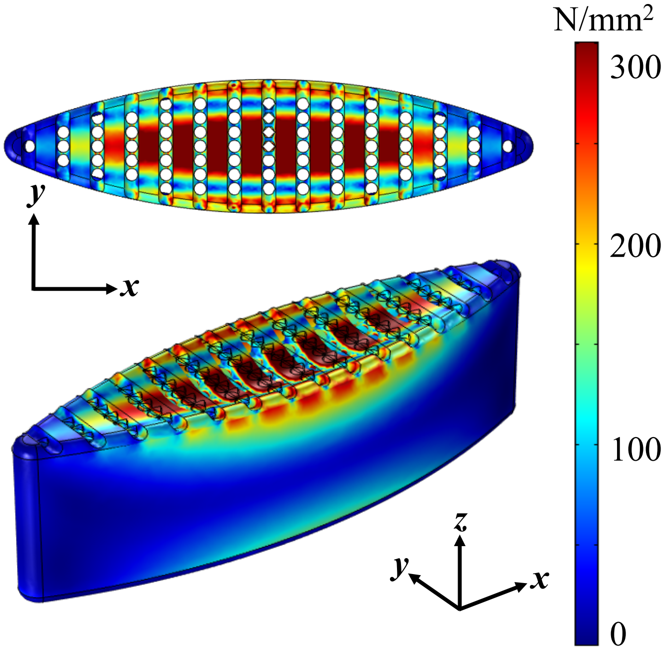

Figure 28. FEM uniform elastic compression simulation of pennate *F. kerguelensis* diatom frustules. Simulation predicted stress distributions in the center of the top valve of the "modified" frustule are similar to those found in nature (Figure 27), particularly near the center and edges, but with a higher maximum stress level. Dimensions for this "modified" frustule are: l=30 µm, w=7.83 µm, and d=0.7 µm.

A summary of data and predicted properties of all diatom models is included in Table 3.

Table 3. Experimental and simulated data from real and "modified" diatom frustule models.

Diatom Species	Number of pores (N) or slits (s)	Pore Diameter (d) or slit width (s) (µm)	Maximum Displacement (µm)	Maximum von Mises Stress (N/mm^2)
Coscinodiscus	2,112	0.60	0.94	4.4
Synedra	146	0.54	7.6 E-5	0.4
F. kerguelensis	163	0.30	0.35	1,595

3.5. Effect of porosity on selected mechanical properties

Assumptions: The porosity of diatom frustule models was increased by either augmenting the pore diameter or by adding extra pores. The number of pores added was set as the maximum pores that fit in the structure without causing broken features (e.g. ribs or edges). It was assumed that the overall frustule porosity in 3D models was a good representation of potential modified frustules. Also, the FEM simulations were assumed to be accurate to represent the effects of porosity on mechanical properties when the porous created had the same arrangement, or when the enlarged porous maintained the original location. For the *F. kerguelensis* diatom specie, the mechanical properties reported by Hamm and collaborators were adopted as starting point for FEM simulation of this specie and further comparison against other centric and pennate diatom species.

To estimate the effect of porosity (e.g., pore diameter *d* and number of pores *N*), several diatom models with specific dimensions (Eq. 5) were created and their mechanical properties were analyzed upon uniform compression simulations.

Changes in pore diameter and pore size were monitored under identical compression loading conditions and are described in Figure 29. In both cases a monotonic increment of the von Mises stress, displacement, and strain energy was observed, indicating that there is a direct correlation between the porosity and the mentioned mechanical properties. Figure 29(*a*) shows the resultant properties using *Coscinodiscus sp.* diatom models similar to those found in nature (*D*=200 μm, *E*=2.3 GPa) with increasing pore diameter, while keeping the number of pores constant (*N*=61). Figure 29(*b*) reveals the calculated properties for identical centric diatom models (*D*=200 μm, *E*=2.3 GPa) with increasing number of pores, and maintaining pore diameter constant (*d*=9.6 μm).

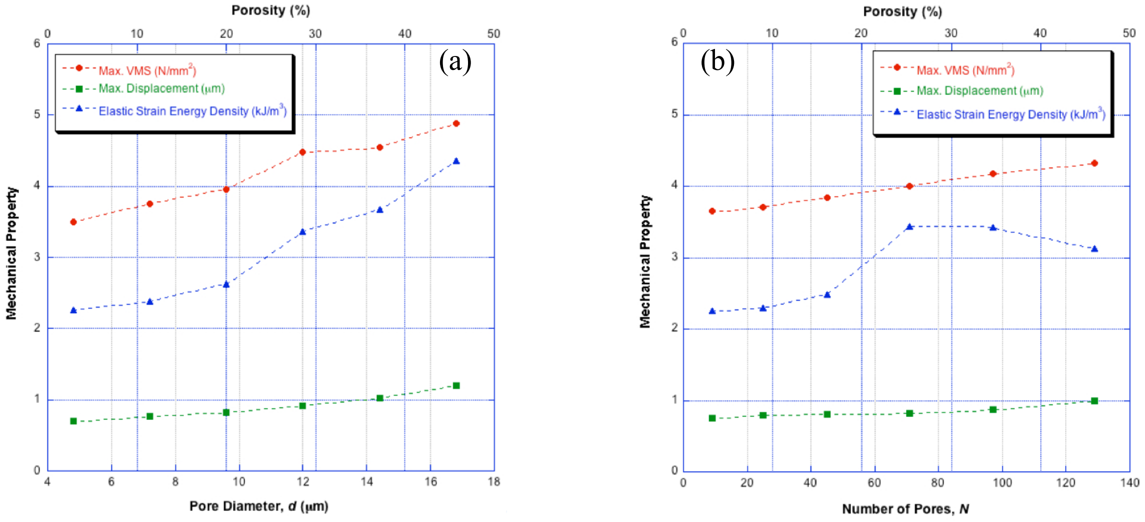

Figure 29. Effect of (*a*) pore diameter and (*b*) number of pores on selected mechanical properties for *Coscinodiscus sp.* diatom models upon FEM uniform elastic compression simulations.

In Figure 30, the sizes of the pores in the diatom frustule were varied to evaluate their effect on the mechanical behavior of *F. kerguelensis* models. The strain energy presented a monotonic increase as the porous size was increased, while for the displacement and von Mises stress an overall increment was reached.

Results for the *F. kerguelensis* diatoms are presented in Figure 30(*a*), which show the calculated properties using frustule models similar to those in nature (l=30 μm, E=22.4 GPa [1]) while keeping the number of pores fixed (N=77). Figure 30(*b*) illustrates the findings for analogous diatom models (l=30 μm, E=22.4 GPa [1]) with a constant pore diameter (d=0.4 μm).

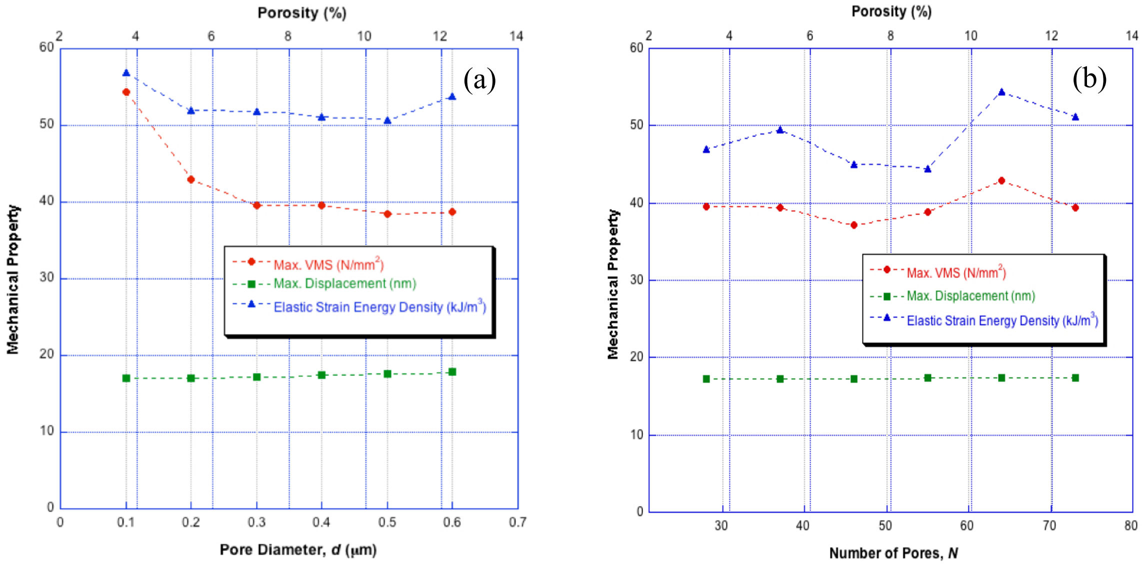

Figure 30. Role of (*a*) pore diameter and (*b*) number of pores on selected mechanical properties for *F. kerguelensis* diatom models upon FEM uniform compression simulations for comparison.

3.6 Summary

In this chapter, C*oscinodiscus sp.* diatom samples were well characterized via SEM techniques prior to nanoindentation experiments in terms of frustule morphology and hierarchical structure. SEM micrographs show characteristic diatom frustule morphology and highly ordered pore arrangement as reported before [11-13]. In addition, SEM imaging revealed that these centric diatom frustules have top surfaces made of a few layers of ordered mesh-like porous structures. SEM characterization of the pennate *Synedra sp.* diatom prior to nanoindentation revealed an elongated frustule containing valve surfaces with distinctive lateral longitudinal slits (s ~ 2 μm). These observations are in agreement with expected structures from aqueous microorganisms that use their small pores for nutrient transport and virus protection.

Analysis of the nanoindentation test results in this study indicates that the *Coscinodiscus sp.* diatom frustules show considerably lower Young's moduli values (1.11-10.59 GPa) compared with that of bulk silica glass (73.1 GPa). Yao *et al.* [2] measured lower *E* values (0.59-2.77 GPa) for this diatom species frustule using similar ambient nanoindentation conditions. The difference in Young's moduli reported here compared to that work may be explained by the larger number of diatoms tested in this study (Tables 1 and 2), allowing for additional statistical analysis and increased confidence in the reproducibility of the nanoindentation data. The results in this study indicate that a large elastic modulus variation exists for *Coscinodiscus sp.* diatom frustules, likely related to each specific frustule dimension and associated layered structure. In this study, the *Coscinodiscus sp.* frustule diameters tested were small (*D* varied from 7-37 μm) which fall within the previously described large and broad set of possible frustule sizes (*D* typically from 70-250 μm). Frustule size is determined by nutrient availability and silica deposition conditions, which are specific to the habitat of particular species.

Further examination of the nanoindentation experimental results in this study reveals that the *Synedra sp.* diatom frustule shows significantly higher Young's moduli values (13.7-18.6 GPa) compared to those of *the Coscinodiscus sp.* diatom frustules. These results are still low compared to that of bulk silica glass. These nanoindentation data on the *Synedra sp.* are reported for the first time. A smaller number of nanoindentation measurements from a *Synedra sp.* diatom frustule were obtained in this study, because the results were found to be reproducible (Table 2). The variation in the mechanical properties of the diatom frustules may be related to different factors affecting their measurement, including the position of the indenter on the sample, the flatness of samples, deviations in density of the biosilica material, frustule porosity, and type of indentation performed.

The simulation techniques in this study involved the validation of the nanoindentation conditions and reproduction of experimental displacement values per diatom species. Since the nanoindentation simulations reproduced well the experimental behavior, a similar method was used to simulate uniform compressions on the diatom frustules in the elastic region. Particularly, the FEM nanoindentation simulation reported in Figure 16 showed a good agreement for small loads, with slight divergence from experimental data when higher loads are applied. The linear trend in the elastic region will change, depending on the indenter tip geometry and model material, among other factors.

The selection of the pore and slit sizes varied depending on the diatom model. For the centric diatom frustules (*Coscinodiscus sp.)*, the "modified" model aimed to evaluate mechanical behavior for the largest possible pore size (with converged stresses) to investigate its effect on future fabricated structures where large *d* values may be desired. For the pennate diatoms (*Synedra sp.* and *Kerguelensis sp.*), specific slit widths (*s*) and pore diameters (*d*) were used respectively, based on potential nano- and microtemplate applications.

Analysis of the FEM simulations in this study reveals that the *Coscinodiscus sp.* diatom frustules show distinct displacement and uniform stress distributions similar to those found in nature. When the pore size is adequate for potential microtemplate applications, a comparable displacement distribution but a lower stress distribution around the sides of the frustule structure are observed. This implies that increasing the pore diameter (*d*) in this diatom species (or similar diatom-inspired structures) can lead to a robust frustule that retains its ability to bend (i.e. displacement distribution) while distributing lower stresses (i.e. von Mises stress distribution) in critical areas such as the pores and sides compared to the stresses found in nature.

Synedra sp. diatom frustules evaluated in this work using SEM micrographs prior to nanoindentation tests confirm their elongated diatom frustule morphology and detailed valve surface microstructures with lateral longitudinal slits. In addition, analysis of the nanoindentation results in this study reveals that the *Synedra sp.* diatom frustules show significantly higher Young's moduli values (13.7-18.6 GPa) compared to those of the *Coscinodiscus sp.* diatom frustules. These results are still low compared to that of bulk silica glass. A small number of nanoindentation measurements from a *Synedra sp.* diatom frustule were obtained in this study, and results were found to be reproducible (Table 2). The smaller elastic modulus variation observed in the *Synedra sp.* diatom frustule measurements is attributed to reduced statistics.

Analysis of the FEM simulations in this study shows that the *Synedra sp.* diatom frustules show less uniform displacement and stress distributions in frustules compared to the centric diatoms. When the slit width (*s*) is decreased for potential nanotemplate applications [14-15], similar displacement distributions are calculated but a more uniform (and lower) stress distribution around the ribs and sides of the frustule structure is observed. This means that fabricating a frustule structure with these characteristics can lead to a versatile porous structure, one which retains its ability to bend, but undergoes lower stresses in critical areas such as slits, ribs and frustule sides compared to the diatom species in nature. Success in this effort would depend on the resolution of the fabrication technique (e.g., etching) required to create ultrathin slit widths and other necessary nanotemplate geometries [16-17].

The effect of porosity on the mechanical properties upon uniform compression simulations was evaluated in this study for specific diatom frustules (*Coscinodiscus sp.* and *F. kerguelensis*) containing pores (Figures 29-30). The *Synedra sp.* frustules were not included in this analysis due to their complex valve surface microstructures including slits, but no pores. As pore diameter increases (Fig. 29(*a*)), *the Coscinodiscus sp.* frustule showed increasing trends for the von Mises stress, displacement and elastic strain energy density values. Similar overall trends are observed for this frustule when the number of pores *N* increases (Fig. 29(*b*)). These findings indicate this frustule morphology is fairly deformable, with an approximately linear relationship between the porosity and the von Mises stress often used as a failure criterion in studies of solids [18-19]. In contrast, the *F. kerguelensis* frustule exhibited more complex trends as the pore diameter and number of pores varied. Overall, trends show a decrease and leveling off (i.e. quickly becoming constant) of von Mises stress and elastic strain energy density levels as pore diameter increases, while displacement values remain unchanged (Fig. 30(*a*)). Similar leveling off of these mechanical traits is observed for the case of an increasing number of pores. It is noteworthy to mention that the simulated mechanical property values of the *F. kerguelensis* frustules were significantly larger (an order of magnitude) compared to those of the *Coscinodiscus sp.* frustules. The large variation in the mechanical properties of these frustules is related to different factors affecting the simulations, including the diatom morphology, frustule shape, experimentally-reported Young's moduli, pore diameter and type of finite element mesh used. Regarding the Young's modulus reported for each diatom species, the broad variation was expected because of the inverse correlation between the elastic modulus and displacement of structures under compression in FEM simulations.

Examination of additional FEM simulations in this study indicates that the "modified" *F. kerguelensis* diatom frustule shows a distinct displacement distribution yet a similar stress distribution compared to diatoms in nature. In fact, when the pore size (*d*) is increased for possible microtemplate applications, a significantly lower displacement distribution around pores and sides of the frustule is calculated. This implies that fabrication of frustule structures with such morphological characteristics may effectively lead to less rigid structures than described earlier for the *Synedra sp.* frustule. For the *F. kerguelensis* frustule, increasing pore size can lead to a decreased ability to bend, probably due to its intricate porous structure, while retaining its ability to sustain stress levels (in pores and frustule sides) compared to the diatom in nature. The evaluated pore size is within the resolution of current fabrication methods, and additional systematic and integrated studies are needed for application purposes.

Experimental stiffness values and SEM information, used to uniquely and precisely define each diatom frustule model, efficiently facilitate the study of their material properties via FEM simulations. Furthermore, simulated load-displacement profiles are found to be well validated upon comparison with experiments. Results show that these frustule morphologies differ in their mechanical behavior under uniform compression conditions. In particular, this study reveals distinct displacement and von Mises stress distributions depending on the diatom species, properties and characteristic pore diameter or slit width.

3.7 References

1. Hamm, C.E., Merkel, R., Springer, O., Jurkojc, P., Maier, C., Prechtel, K., and Smetacek, V. Architecture and material properties of diatom shells provide effective mechanical protection. *Nature* **421**, 841-843 (2003).

2. Yao, S., Subhash, G. and Maiti, S. Analysis of nanoindentation response of diatom frustules. *Journal of Nanoscience and Nanotechnology* **7**, 4465-4472 (2007).

3. Garcia, A., Sen, D. and Buehler, M. Hierarchical silica nanostructures inspired by diatom algae yield superior deformability, toughness, and strength. *Metallurgical and Materials Transactions A* **42**, 1-9 (2011).

4. Losic, D., Short, K, Mitchell, J.G., Lal, R., and Voelcker, N.H. AFM nanoindentations of diatom biosilica surfaces. *Langmuir* **23**: 5014-5021 (2007).

5. Kröger, N. and Poulsen, N. Diatoms-from cell wall biogenesis to nanotechnology. *Annual Review of Genetics* **42**, 83-107 (2008).

6. Losic, D., Pillar, R., Dilger, T., Mitchell, J., and Voelcker, N. Atomic force microscopy (AFM) characterisation of the porous silica nanostructure of two centric diatoms. *Journal of Porous Materials* **14**, 61-69 (2007).

7. Diaz Moreno, M., Ma, K., Schoenung, J., and Dávila, L.P. The hierarchical porous structure and mechanical properties of diatoms: an integrated approach toward engineered nanotemplate. Submitted (2015).

8. Almqvist, N. *et al*. Micromechanical and structural properties of a pennate diatom investigated by atomic force microscopy. *Journal of Microscopy* **202**, 528-532 (2001).

9. Ki, J. S. *et al.* Comprehensive comparisons of three pennate diatoms, *Diatoma tenuae*, *Fragilaria vaucheriae*, and *Navicula pelliculosa*, isolated from summer Arctic reservoirs (Svalbard 79°N), by fine-scale morphology and nuclear 18S ribosomal DNA. *Polar Biology* **32**, 147-159 (2009).

10. Oliver, W.C. and Pharr, G.M. An improved technique for determining hardness and elastic modulus using load and displacement sensing indentation experiments. *Journal of Materials Research* **7**, 1564-1583 (1992).

11. Gordon, R., Sterrenburg, F., and Sandhage, K.A Special Issue on Diatom Nanotechnology. *Journal of Nanoscience and Nanotechnology* **5**, 1-178 (2005).

12. Gordon, R., Losic, D., Tiffany, M.A., Nagy, S.S., and Sterrenburg, F.A.S. The glass menagerie: diatoms for novel applications in nanotechnology. *Trends in Biotechnology* **27**, 116-127 (2009).

13. Hildebrand, M., Doktycz, M., and Allison, D. Application of AFM in understanding biomineral formation in diatoms. Pflügers Archi EJP **456**, 127-137 (2008).

14. Belegratis, M.R., Schmidt, V., Nees D., Stadlober, B., and Hartmann, P. Diatom-inspired templates for 3D replication: natural diatoms vs. laser written artificial diatoms. *Bioinspiration and Biomimetics* **9**, 0160041-11 (2014).

15. Todd, T. *et al*. Iron oxide nanoparticle encapsulated diatoms for magnetic delivery of small molecules to tumors. *Nanoscale* **6**, 2073-2076 (2014).

16. Bao, Z. *et al.* Chemical reduction of three-dimensional silica micro-assemblies into microporous silicon replicas. *Nature* **446**, 172-175 (2007).

17. Pérez-Cabero, M., Puchol, V., Beltrán, D., and Amorós, P. Thalassiosira pseudonana diatom as biotemplate to produce a macroporous ordered carbon-rich material, *Carbon* **46**, 297-304 (2008).

18. Bower, A.F. Applied mechanics of solids. *CRC/Taylor & Francis*. Boca Raton, Florida: 2010. p 47-49.

19. Structural Mechanics User's Guide. *Comsol Multiphysics*. COMSOL, Palo Alto, California, 2013.

CHAPTER 4: AFM-BASED NANOINDENTATION AND FEM SIMULATIONS

4.1 Experimental evidence

Mechanical analysis and characterization of diatom structures have been pursued mainly using atomic force microscopy (AFM), nanoindentation and scanning electron microscopy (SEM) imaging techniques. Initial studies conducted by Higgins *et al.* [1] focused on the topography and mechanical properties of adhesive mucilages secreted by the *Craspedostauros australis* diatom species using the AFM technique. A soft and cohesive outer mucilage layer was found, encasing most of the frustule. Subsequently, Hamm *et al.* [2] investigated the mechanical protection offered by the frustule using needle loading tests on several species, discovering an inverse relationship between the size of the frustule and the force required to break it. Later, *in vivo* studies of several diatom species were performed by Higgins *et al.* [3] using AFM experiments to determine morphology features of the diatom frustule. Losic *et al.* [4] analyzed morphology via SEM and performed AFM-based nanoindentation, mapping the frustule of the *Coscinodiscus* diatom species, and finding that the elastic modulus varied widely (1.7-15.6 GPa) depending on porosity, thickness and pore size. In further studies, Losic *et al.* [5] compared morphological features of *Coscinodiscus* versus *Thalassiosira eccentric* species, including the organization of porous silica layers, topography, pore size, shape and density. Recently, Hildebrand *et al.* [6] investigated other regions in several diatom biostructures (*e.g.* valves, girdle bands and bristles) using AFM, enabling visualization of girdle bands at several scales and describing varied porous morphologies within the frustule.

From all previous studies, a variety of mechanical properties of biosilica diatom frustules based on nanoindentation have been reported. The challenges of measuring mechanical properties of diatom species experimentally are due to the differences existing between each species and sample preparation. A clear correlation between mechanical properties and diatom features (e.g. porosity, shape, thickness and pore size) has not yet been established. Therefore, robust modeling across different length scales is necessary to simulate the response of diatom frustules to deformation, in order to facilitate future biosilica nanotemplate design and fabrication. Associated experimental testing is also required to validate the accuracy of the modeling.

4.2 Previous calculations

In a combined experimental-simulation study, Hamm *et al.* [2] reported FEM simulation on the diatom structures of *Thalassiosira punctigera* species to study the strength of the diatom structure as protective armor against predators. In a recent study, Garcia *et al.* [7] performed molecular dynamic simulations of diatom-inspired nanoporous materials, investigating the effect of hierarchical nanoporous layers under tensile deformation. The results in that study showed a significant enhancement of the mechanical properties of the material, including superior deformability compared to brittle silica glass. The limited number of similar studies highlights the need to explore increased length scales via FEM analysis to calculate the properties of diatom frustules at the microscale.

4.3 Experimental section

The experimental study of centric and pennate diatom frustules via AFM was conducted using tapping (imaging) and contact (force spectroscopy) modes. Parameters such as scanning speed, points per line, and indentation depth were kept constant for both diatom species.

Assumptions: The surfaces of diatom frustules were assumed free of organic material and completely dried (no fluids like water), making the AFM imaging a true representation of the morphology of the frustule and the methodology for calculating the elastic modulus valid as it did not account for capillary forces. The AFM images and depth profiles reported were obtained from the first layer of diatom frustules (cribellum), as most of the frustules remained intact (three porous layers together) and the frustule and pore diameters found were in agreement with average reported data for those species. It was assumed that the center of the centric diatom frustule was the flattest and even part of the epitheca, so it was selected as initial location for AFM scans. This flat surface allowed a better AFM scan of the surface and gave the most optimal morphology of the frustule for calculating pore diameter and pore depth. The pillars reported in Figure 33 were referred as the inner part of the cribellum frustule, and their height as part of the thickness of the epitheca. The regular spacing and pillar diameter were close to the pore-to-pore distance and pore diameter of the cribellum, which reinforced this assumption. Nanopores found in the pennate diatom study between solid ribs indicate they replicate along all the structure in a similar arrangement, density and size. In addition, the AFM nanoindentation performed to the centric and pennate diatoms are assumed to have occurred only in the solid area of the frustule, and at a particular location (not slipping).

4.3.1 Morphology analysis via AFM

In sections 4.3.1.1 and 4.3.1.2, the topography investigation of two diatom species with different symmetry is presented, including the depth profile along the main morphology features of their frustules (e.g. pores, ribs, slits). These profiles provided additional insights into the detailed morphology of the well-arranged diatom structures as depicted in Figures 31-35.

4.3.1.1 Coscinodiscus sp.

AFM analysis of the *Coscinodiscus sp.* diatom frustule (using tapping mode) provides additional insights into the detailed morphology of its layered structure as depicted in Figure 31. The first layer of the centric diatom frustule evaluated via AFM exhibited a mesh-like pore structure, with an average pore diameter *d* of ~ 100 nm. A close view (Figure 31(*b*)) showed a hexagonal arrangement of the pores. Further AFM evaluation of the first layer (Figure 31 (*c*)) revealed an average pore depth of ~57 nm.

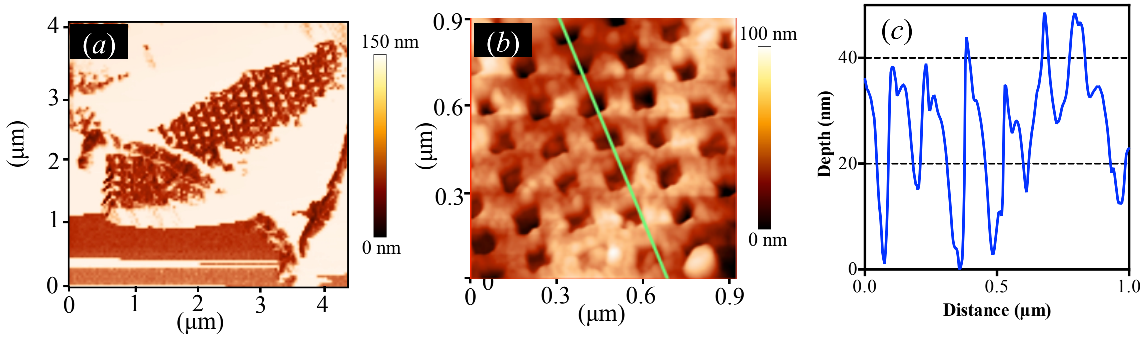

Figure 31. AFM image of a centric *Coscinodiscus sp.* diatom frustule displaying its ordered mesh-like porous structure (*a*) with an average pore diameter *d* of ~100 nm and a hierarchical layered structure (*b*), and its corresponding depth-distance profile (measured along a line shown in green) from the top layer of the frustule (*c*), revealing an average pore depth of ~57 nm.

Figure 32 shows a typical AFM image (in tapping mode) of a *Coscinodiscus sp.* diatom frustule, providing detailed surface morphology of its regularly arranged porous structure and associated depth profile. It is also known that the *Coscinodiscus sp.* frustule [5] consists of a hierarchical arrangement of three porous layers. In this study, the top layer (or cribellum) of the *Coscinodiscus sp.* frustule was measured to have an average pore diameter *d* of 320 nm and average pore depth of ~325 nm (Fig. 32(*a-b*)). The hexagonal pore pattern found via SEM images (Fig. 10(*a-b*)) was even more evident in AFM images (Fig. 32(*a*)), with pore-to-pore distance of ~1 μm. The porosity was calculated 46.7 % as shown in Figure 32. Initially, a large scan was obtained (30x30 μm) and as the surface of interest was more evident a smaller scan was performed (6x6 μm). The 3D view of the diatom cribellum surface suggests potential uses in nanolithography and nanotemplate applications (Fig. 32(*c*)).

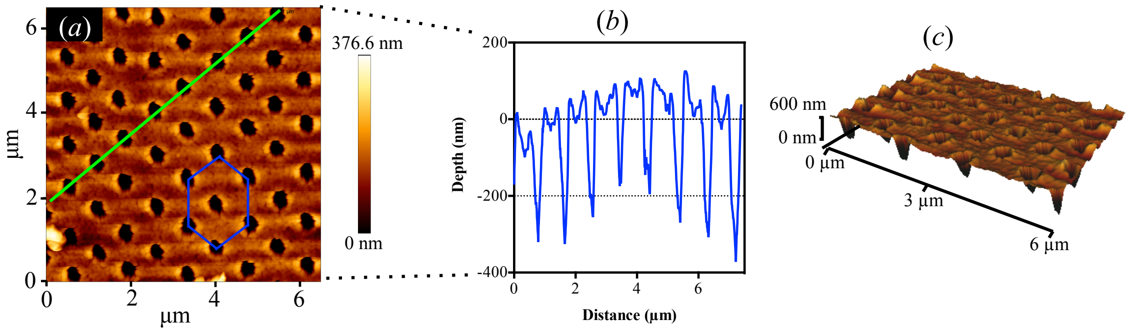

Figure 32. AFM image of the cribellum (first outer layer) surface of a *Coscinodiscus sp.* diatom frustule and related data (*a-c*) showing an evenly distributed porous layer (*a*) forming a hexagonal pattern shown in blue, the depth-distance profile (*b*), measured along the green line, with an average pore depth of ~325 nm, and a 3D view of the cribellum topography (*c*).

AFM evaluation allowed the high-resolution study of morphological features such as pore depth and frustule roughness (via 3D topography view), which prompts discussion of how these specific structures might be used for potential nanotechnology applications, by using either real diatom frustules or similar bio-inspired structures.

In addition, Figure 32 reveals very organized arrays of pores, which is significant since they can be used for nanotechnology applications [8] due to their repeatable micro-scale pattern as well as their shallow pore depth (~325 nm). This is of particular relevance for applications that require a platform for deposition of nanomaterials at specific locations [9], as well as thin-film deposition (e.g. pore tuning by depositing thin layers of materials) [9]. The average pore diameter measured in this study via AFM for the *Coscinodiscus sp.* frustule was six times larger than the reported value for similar centric diatoms [5], due to the typical high variability of frustule sizes in nature, even within similar diatom species as reported elsewhere [10].

Representative 3D views of these centric diatom surfaces confirmed they are not flat, and their roughness identified using AFM allows further understanding of the requirements for applications such as nanolithography. In a recent study, diatom frustules have been suggested as 3D molds for nanolithography applications [11], and the AFM 3D views obtained in this study show that potential through the replicable 3D nanofeatures as shown in Fig. 32(c).

Further AFM imaging of the back surface of a frustule cribellum depicts a hexagonally arranged set of hollow pillars of about 100 nm in height with inner perforations of 50 nm in depth as illustrated in Figure 33. Pillars are equally spaced with a pillar-to-pillar distance of ~1 μm measured from center to center. The observed nanopillar arrays (Fig. 33(*b*)) could be useful as a well-defined mask for growing nanopillars at precise locations, avoiding misalignment in the nanopillar growth process, a common challenge in their fabrication [12-13]. The small pore size observed (~50 nm) and equidistant separation (~1 μm) could be used for creating arrays of gold nanopillars even smaller than those accomplished for electrophysiological stimulation [14], increasing surface area thus reducing electrode impedance, which is desirable for cell stimulation. In addition, the use of this biological template (centric diatom) could help to improve the resolution of deposited gold nanopillar arrays, currently carried out using low-resolution alumina porous templates [15].

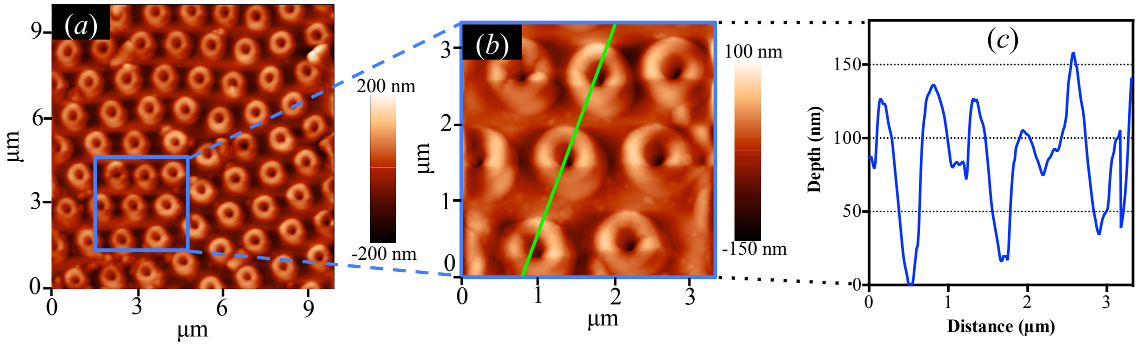

Figure 33. AFM image of the back surface of a frustule cribellum of a *Coscinodiscus sp.* diatom and associated data (*a*-*c*), showing distinct hollow pillars (*a*) of approximately 100 nm height (*b*). The depth-distance profile (*c*), measured along the green line in (*b*), reveals these hollow pillars have an average pore depth of 50 nm.

Characterization of the diatom internal surfaces (Fig. 33(b)) is important as it describes how centric frustules are structurally reinforced, and it opens varied possibilities to design similar bio-inspired structures to mimic the flexible yet strong mechanical response of lightweight porous structures. The material surrounding the pillars (Fig 33(*b*)) likely contributes to the mechanical strength of the frustule, while reducing density due to the hollow geometry. This design of nature allows increasing strength of frustule locations where fracture could potentially occur (pores) under expected environmental loads, without incurring higher energy building requirements.

Furthermore, the distance between the cribellum and the cribrum (next frustule layer underneath) and the areola (third and last frustule layer with larger pores) represents the bottom of the pillars (height ~325 nm) while in other studies this interlayer thickness has been reported to be approximately 250 nm [5]. The difference (30%) between the observed and the reported values is in agreement with the variation expected within similar diatom species grown under different environmental conditions. The exposed pillars in this study are small in height (~100 nm) compared to the overall epitheca thickness of ~1μm, and they likely contribute to the hierarchical reinforcement mechanism used by diatoms to strengthen their frustule while remaining lightweight.

Typical depth profiles as shown in Fig. 33(*c*) reveal pillars on the average have dimensions of ~100 nm height and hollow depth of ~50 nm, in agreement with reported values by independent studies [5] of ~200 nm in total. In addition, cross sectional SEM images [5] of the centric diatom three-layered (cribellum-cribrum-areola) frustule demonstrated in forms of peaks the pillars reported in Fig. 33(*b*). These pillars could lead to the design of advanced diatom-inspired structures that are both stronger and lighter than currently available, due to their hollow arrangements, thus significantly reducing fatigue failure due to cyclic compression-tension loads.

4.3.1.2 Synedra sp.

AFM morphology evaluation of various pennate *Synedra sp.* diatoms indicated that this elongated frustule does not have a layered structure but contains an ordered arrangement of slits (and ribs) instead, with an average slit depth of ~71 nm, average slit width *s* of ~ 400 nm, and rib thickness of 500 nm on average as shown in Figure 34. AFM images also revealed a central solid region along the longest axis of the frustule (Fig. 34(*b*)), dividing the slits and ribs in two sections symmetrically.

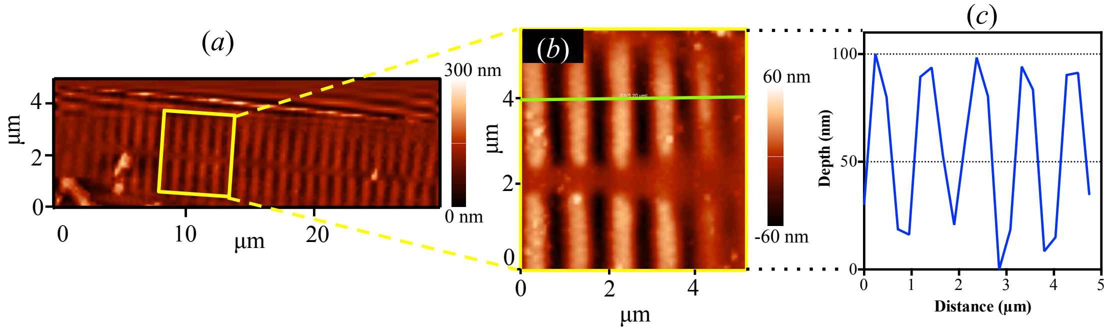

Figure 34. AFM image of the outer surface of a *Synedra sp.* diatom frustule and corresponding data (*a-c*), displaying its distinct rib structure (*a*) with an average slit width *s* of ~400 nm and a rib thickness *t* of approximately 500 nm (*b*). Depth-distance profile measurements (*c*), following a green line along the top of the frustule (*b*), indicate an average slit depth of ~71 nm.

Diatoms frustules are known to be responsible for cell integrity and protection from predators [2]. AFM analysis of pennate diatoms in this study reveals unique construction of their frustules compared to the centric diatoms. Earlier investigations on the morphology of pennate diatoms have reported that these diatoms use raphes to move over surfaces [16].

Examination of pennate frustules via AFM imaging reveals a significantly different siliceous structure (Fig. 34) compared to the centric species (Fig. 32). A symmetric group of ribs equally spaced along the longest axis of the frustule gives the reinforcement required to keep the frustule rigid. Contrary to the hierarchical and radial reinforcements of centric diatoms (Fig. 32), pennate diatoms base their architectural integrity on a large arrangement of small features (ribs and slits), which are perpendicular to the longest axis of the frustule structure and with no porous layers. In addition, a solid region in the center of the frustule of ~10 μm length was observed, which potentially reinforces the epitheca structure and helps distribute stresses along the longest axis of the frustule while minimizing the impact of varying tensile and compression loads. Architectures such as that exhibited by the pennate diatom (Fig. 34(a-b)), with evenly spaced ribs and slits, are expected to efficiently dissipate stresses sustained under naturally occurring loads.

The observed longitudinal spine likely acts as structure-stabilizer and prevents crack propagation along the longest axis of the frustule. The solid region in the center of the structure is critical to confer higher mechanical properties when compared with other structures, while remaining lightweight. These findings are in agreement with previously reported investigations of related pennate diatom species [17] where morphological features (ribs) conferred *Navicula sp.* similar mechanical properties as in the case of the *Synedra sp.* presented in this study.

Due to the presence of ordered micro-slits and ribs in the epitheca structure of elongated frustules, pennate architectures could be useful in applications such as photovoltaic and energy storage devices where their unique features could be replicated [18]. In addition, pennate diatom frustules have been proposed to serve as a substrate material of another metal oxide material (e.g TiO_2 or GeO_2) by adding those materials within the diatoms' micro-features to create dye-sensitive solar cells or electroluminescent devices [18].

Given the high spatial resolution of AFM imaging, a close-up AFM image of the top surface of a *Synedra sp.* diatom frustule (Figure 35) further exposed that there is a set of pores in the concave region between the ribs (Fig. 35(*a*)) for which a distinct depth profile was obtained (Fig. 35(*c*)). The approximate diameter and depth of those ordered pores were 100 nm and 10 nm respectively. These pores were located between the reinforced ribs, which indicates their potential use for filtering out hazardous organisms while keeping the structure flexible and strong.

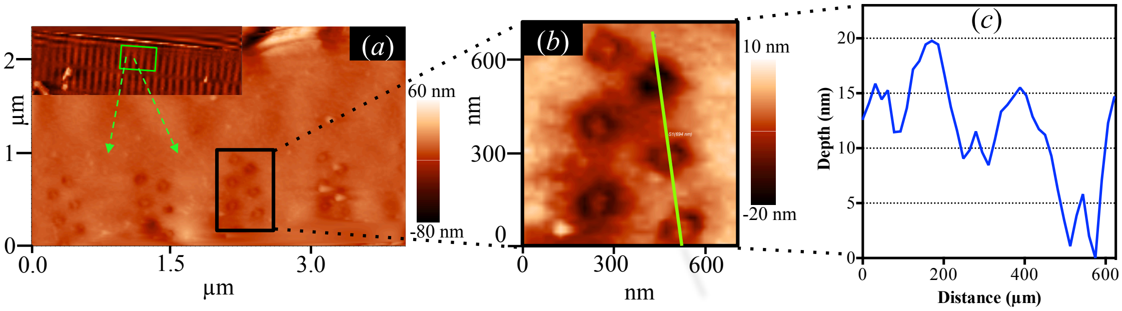

Figure 35. AFM image of a *Synedra sp.* diatom frustule and its corresponding depth-distance profile (*a*-*c*), displaying ordered pores in the top valve (*a*). Pores are located within the ribs (as shown within a black box), in the lower region of the concave areas (*b*), with pore diameters ~100 nm. Depth profile (*c*) shows an average pore depth of approximately 10 nm, measured along the green line in (*b*).

AFM imaging in this study permitted measurement of varied nano-features such as pore diameter (~100 nm) as shown in Fig. 35(*b*), as well as ribs and slits for the pennate diatom. The nanopores located between the ribs indicated that this arrangement is likely a more favorable pore distribution for this type of reinforcement. In addition, the pseudo hexagonal pore arrangement (Fig 35(*b*)) is expected to contribute to the reduction of any crack propagation in the frustule structure (e.g. by growth and coalescence of nanopores) in a similar fashion reported for synthetic amorphous silica nanostructures [19]. This finding indicates that this particular nanopore arrangement observed in pennate diatom frustules is probably efficient for reducing frustule weight while minimizing stress distributions around the pore for biological protection, as reported in other studies for similar pennate diatoms [7,10-20].

In addition, the characteristic average pore depth (Fig. 35(*c*)) for pennate diatoms was 30 times smaller than the equivalent value measured for centric diatoms, despite the fact that both species registered similar epitheca thickness (~1 μm) [2,5]. Also, the pore diameter-to-pore depth ratio between the two diatom species was consistent with previous reported studies [10,21]. The size and location of the pores displayed by the pores in the pennate diatoms (Fig. 35(*a*-*c*)) are of relevant importance in nanotemplate applications for depositing semiconducting nanocrystals or as reaction vessels with small features than prior approaches via laser-embossing of Si substrates [22].

The variation observed between SEM-measured and AFM-measured dimensions in the diatom frustules investigated in this work (e.g. pore diameter, rib thickness and slit width) can be attributed to different factors, including intrinsic technique resolutions, imaging dissimilar frustules in each characterization technique and frustule morphology. The high variability of frustule sizes in nature, even within similar diatom species, is a common challenge in diatom research [10] and thus variation within the imaged frustules was expected.

4.3.2 AFM-based nanoindentation experiments

AFM-based nanoindentations were performed on several centric and pennate diatom frustules under similar experimental conditions to measure their mechanical properties. To determine the mechanical properties of individual diatom frustules, AFM-based nanoindentations were carried out on different locations of the top frustules, selected from AFM images taken previously. The AFM images permitted the selection of a nanoindentation location near a morphology feature of interest (e.g. pore, slit, rib) for further evaluation. Additionally, several nanoindentation locations were obtained simultaneously for a given frustule, leading to improved statistical results, since potential sources of variability were significantly reduced (e.g. moving sample between imaging and nanoindentation mode, potential tip breakage, and human error).

4.3.2.1 AFM Nanoindentation: load-displacement curves and Young's modulus analysis

In order to determine the mechanical properties of individual diatom frustules, AFM-based nanoindentations were carried out on different locations of the frustules based on AFM images taken prior to the indentation experiment.

AFM images permitted to define a nanoindentation location close to a frustule feature of interest (e.g. pore, slit, rib). Additionally, several nanoindentation locations were selected simultaneously from an AFM image, which translated in more accurate locations and less interference with potential moving of the sample between imaging and nanoindentation mode.

4.3.2.1.1 Coscinodiscus sp.

Figure 36 displays representative load vs. displacement curves showing indentation locations on the top valve of *Coscinodiscus sp.* frustules. Nine indentations were performed in each frustule, at various locations of the frustule, to obtain an average Young's modulus E value. The average Young's modulus E_{avg} of the centric frustules was 21.5 GPa, calculated from a set of over one hundred AFM nanoindentations. This average value is considerably larger (~5x) than that reported via ambient nanoindentation [23], yet smaller than bulk silica glass (73 GPa) as summarized on Table 4. The difference in Young's moduli reported here compared to the prior work can be explained by the localized nature of AFM measurements (tip radius ~20 nm captures small property variations within a frustule). The robust statistical analysis due to the high number of indentations tested in this study allows increased confidence in the reproducibility of the AFM nanoindentation data.

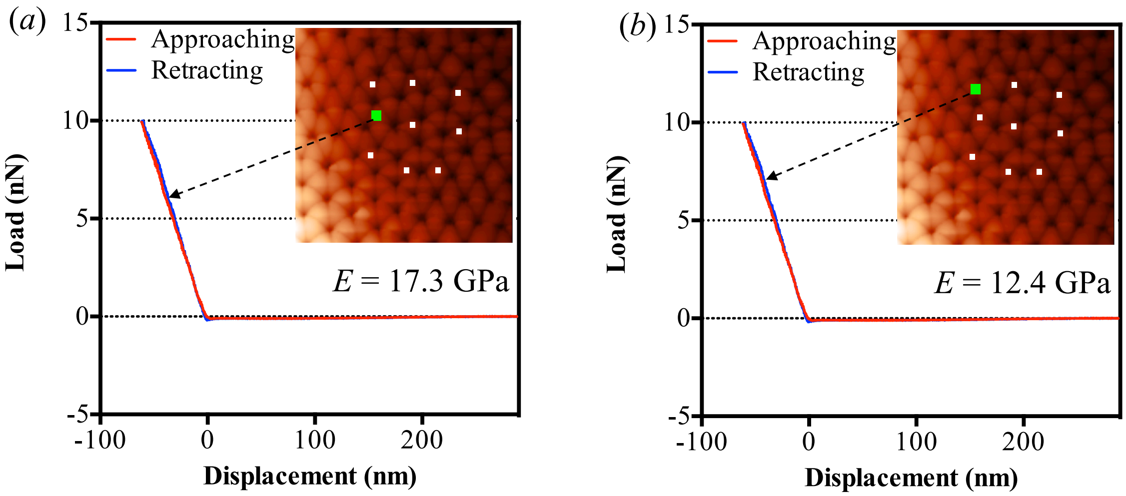

Figure 36. AFM nanoindentation force curves for representative *Coscinodiscus sp.* diatom frustules (*a-b*), displaying associated approaching (red line) and retracting (blue line) curves. AFM images of the outer surfaces of these frustules contain several indentations, shown as colored dots (green indicates precise locations where individual force curves were obtained). Young's modulus measurements were found to be greater (~7x) on average than those obtained via ambient nanoindentations [23], but smaller than bulk silica glass (73 GPa).

Table 4. Summary of selected nanoindentation results for *Coscinodiscus* centric diatom specie via AFM-based nanoindentations.

Experiment ID	E (GPa)
C5	21.2
C6	21.55
C7	23.83
C8	26.24
C9	29.4
C10	33.03
C11	39.56
C12	25.44
C13	29.41
C14	40.61
C15	13.59
Mean	21.52
Standard deviation	12.53

In previous studies, Young's moduli of similar centric species have been reported to vary from 3.4 ± 1.4 to 15.6 ± 5.1 [5] GPa, and even lower 0.11-1.7 GPa [24], which further reinforces the knowledge that the mechanical properties of centric diatom frustules change broadly depending on factors such as indentation location, frustule morphology and loads among others. This variation in Young's modulus within a frustule is related to the biomineralization process that occurs when diatoms absorb silicon from the environment, distribute it within the cell, and convert it into intricate silica nanostructures [25-26]. This mechanical property difference between biomineralized and synthesized materials is also observed in other hierarchical materials such as cortical bone, where its elastic modulus is ~15.7 ± 3.5 GPa [27] while the synthetic form of its major component (calcium phosphate) ranges from 70-120 GPa [28]. Centric diatom frustules are mechanically comparable to other man-made materials such as porous silicon for which the elastic modulus ranges from 8.1 to 22.3 GPa, suggesting diatoms as an inexpensive and biocompatible alternative for drug delivery applications, where porous silicon is currently being used [29].

Furthermore, the robust and systematic procedure for testing and processing the data obtained from AFM nanoindentations in diatom frustules developed here reduces the potential human error from sample preparation to data acquisition and analysis, which is critical when large spatial variations of mechanical properties are observed.

Extensive examinations of pre- and post-AFM nanoindentation results (Fig. 37) indicated that the frustule topography was noticeably modified by the indenter, allowing increased confidence in the reproducibility of the AFM nanoindentation data, and confirming centric frustules endured plastic deformation only, as indicated by the depth profiles shown Fig. 37(*b*) and Fig. 37(*d*). The verification of the permanent deformation was important to accurately define the materials property calculation method based on the elastic-plastic behavior of the structure and the appropriate contact mechanics model [30].

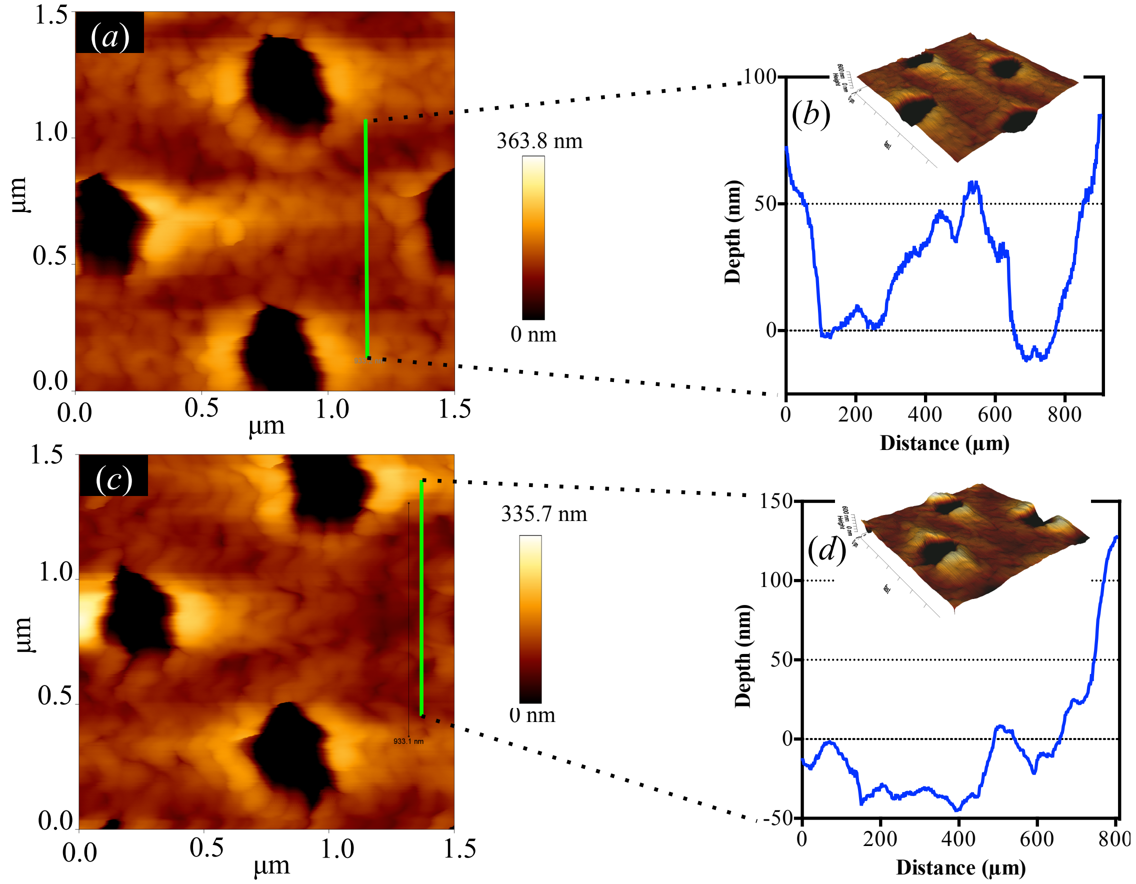

Figure 37. AFM images of a *Coscinodiscus sp.* diatom frustule section displaying before (*a*) and after (*c*) indentation imaging, and related depth profiles (*b*) and (*d*), measured along the green lines in the respective images. A cross-sectional image of the frustule shows changes in surface morphology and indentation depth in each case: before (*b*) and after (*d*) indentation.

In addition, the 3D cross-sectional images of the centric diatom generated by AFM (Fig. 37(*b*) and 37(*d*)) could be used to determine the amount of deformation caused on the diatom surface under varied loads, which could be helpful for future increasingly realistic 3D *in-situ* nanoindentation experiments.

4.3.2.1.2 Synedra sp.

Similar AFM nanoindentation experiments were carried out on several locations of the top surfaces of elongated *Synedra sp.* diatom frustules, resulting in distinct load vs. displacement curves. These curves allowed the calculation of the Young's modulus of a pennate frustule via curve analysis as described earlier in the Methodology section.

Figure 38 shows typical load vs. displacement curves upon AFM nanoindentations of a *Synedra sp.* diatom frustule. Nine indentations were achieved at varied locations in the same frustule, on the ribs of the epitheca (i.e. likely the most reinforced part of the frustule and the highest features of the valve). The average Young's modulus E_{avg} of the pennate *Synedra sp.* frustule was calculated to be 26 GPa using a set of over forty force curves as described in Table 5. This average value is about 1.5x higher than the obtained via ambient nanoindentation [23], and its large standard deviation is a consequence of the different rib locations tested across the frustule. These results remain significantly lower than that of bulk silica glass. Previously reported elastic moduli for pennate species varied from 0.54-0.76 MPa for *Pinnularia viridis* [31], 7-100 GPa for *Navicula sp.* [17], and 100 kPa for live diatoms [32]. The low elastic modulus of live diatoms is the effect of the stress-induced mobility of water molecules that results in an increased strain rate for hydrated amorphous silica glass [33-34]. The large variation in the mechanical properties of diatoms among the studies reported to date highlight the need to develop a robust and methodic procedure to prepare, test, and analyze AFM nanoindentations for varied diatom frustules, such as the one presented in this study. Several pennate diatom species have been studied via AFM tapping and contact modes, yet both AFM imaging and nanoindentation results for the *Synedra* diatom species simultaneously are reported here for first time, to the authors' knowledge.

The variation in Young's modulus for this diatom species can be attributed to different factors such as the complex frustule morphology and unique slit and rib structure, and changes in density in the diatom frustule. The higher elastic modulus of the pennate frustule is hypothesized to be due to its highly reinforced structure and lower porosity, compared to the centric diatom studied, even at similar deflections. This observation raises the possibility that certain diatom frustule architectures could be more favorable for optimizing silica density at particular deposition locations. One of the causes of this behavior is biogenic-silica formation, driven by the precipitation of multiple layers of silica nanospheres (~10-100 nm diameter), which are more efficiently packed in the pennate frustule rather than in the centric geometry. These highly dense designs will have improved mechanical properties and subsequently their ability to respond to mechanical loads from the environment will be superior to the frustules with less efficiently packed silica.

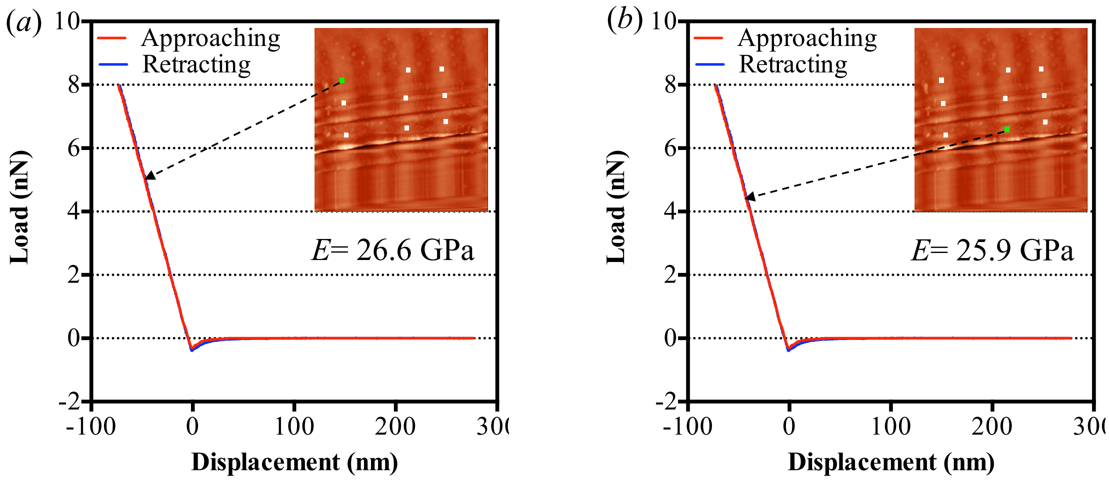

Figure 38. AFM nanoindentation load curves for a characteristic *Synedra sp.* diatom frustule (*a-b*) show localized indents, on the rib section, as indicated by arrows for specific locations. AFM images of the pennate diatom frustule show various indentations, displayed as green dots. Young's modulus values for areas tested are significantly higher on average (~1.2x) than equivalent values measured for centric diatoms, but lower than bulk silica glass (73 GPa). Additionally, *E* measurements are found to be greater by 1.5x on average than those obtained via ambient nanoindentations [23].

Table 5. Experimental data measured from selected diatom frustules in this study for *Synedra* pennate diatoms using AFM-based nanoindentations.

Experiment ID	E (GPa)
P1	36.4
P2	11.6
P3	31.2
P4	33.7
P5	20.7
P6	18.3
P7	26.6
P8	25.9
P9	23.6
P10	20.3
P11	31.4
Mean	26.04
Standard deviation	11.96

Given their more resilient mechanical properties (compared to centric diatoms), pennate diatom frustules are ideal for drug delivery device applications as studied by several research groups [35]. The surface modification of pennate diatom frustules have allowed achievement of larger drug loadings of up to 22% (*w*/*w*) [35] and controlled slow release with in vitro capabilities, while taking advantage of the low-cost and biocompatible silica frustules [36].

4.4 Simulation section

Based on the SEM and AFM images obtained in the experimental section, hierarchical 3D centric models were constructed to replicate the three-layer composition of the diatom frustules and evaluate their role on diatoms' mechanical behavior. Subsequently, FEM simulations were carried out on those structures with varied cross sectional areas.

Assumptions: In the next FEM study, it was assumed that the three major porous layers of the epitheca could be simulated accurately to represent a real diatom epitheca frustule. Also, it was assumed that 8-fold symmetry applied (one eight was simulated) and that half of the centric valve could be used to denote the most important parameters to study diatom frustule mechanical behavior. The close agreement between experiment and the 3D nanoindentation simulation of a centric diatom was assumed to validate the uniform compression simulations carried out on an eight of a frustule. The calculated von Mises stress (compared to the yield strength of bulk silica) was defined as a valid failure criteria despite the fact that diatom frustules' Young's modulus differed largely from the reported values for bulk silica.

4.4.2 FEM simulations of hierarchical nanostructures

As described previously (Methodology section) uniform compression simulations of centric diatom models only were carried out to predict the role of the hierarchical structures on the mechanical properties of these diatom frustules. In particular, one eighth of the 3D hierarchical three-layered epitheca model was uniaxially compressed along the *z*-direction with loads ranging from 2.5 to 10 mN. Tetrahedral mesh elements were used with higher element density around the pores of each siliceous shell layer in the frustule. In addition, another set of hierarchical porous layers was created with an "I-beam" cross sectional area using SEM images. Such models are more realistic than the simple stack of porous layers as it is a characteristic feature in the centric diatom frustule.

The simulation techniques in this study included the verification method previously reported for diatoms [23], based on the comparison of experimental and simulation nanoindentation data. Since the nanoindentation simulations reproduced well the experimental behavior in the elastic region, a similar method was used to simulate uniaxial compression on several hierarchical centric epitheca valves.

4.4.2.1 Coscinodiscus sp. with stacked cross sectional area

Figure 39 illustrates the resultant displacement and von Mises stress distributions on a 3D epitheca section when a uniaxial load p of 10 mN is evenly applied on its top porous layer. Relatively large variations occur in both displacement and stress distributions along the load (z-) direction.

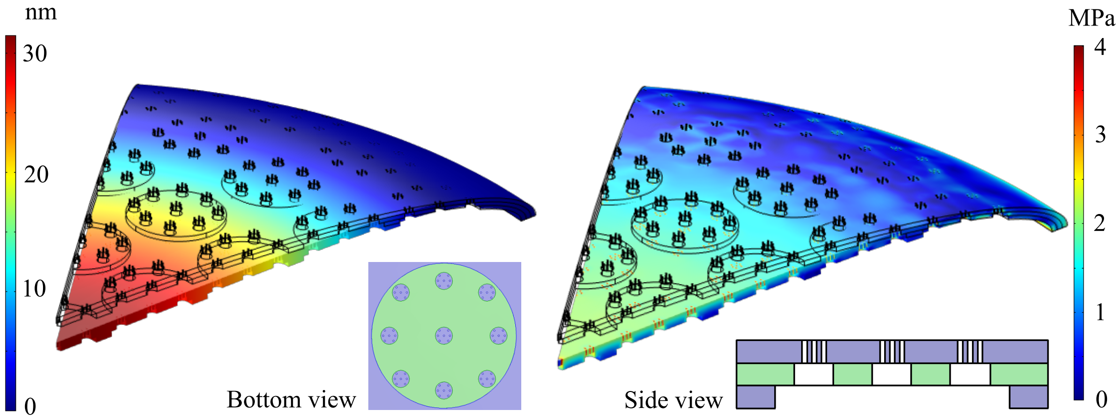

Figure 39. Displacement (left) and von Mises stress (right) distributions of a three-layered hierarchical diatom model under a uniaxial compression load of 10 mN. The higher displacement and stress concentrations were located at the very center of the structure, and decreased radially outward toward the edge of the frustule.

Figure 39 shows higher displacement and stress concentrations located at the center of the epitheca structure, which decreased radially outward. Relatively small deflections (or structural modifications) are evident in both displacement and stress distributions along the load direction. This behavior of the hierarchical model upon compression is favorable as it is probably an energy-efficient mechanism to distribute stresses while preserving its structural integrity and flexibility. The radial strain and stress distributions are valuable information not available experimentally that evidence the energy distribution mechanism of hierarchical biostructures. Current nanodevice fabrication efforts of hierarchical structures [37] and porous composites [38] could be benefited from minimizing premature failure under uniaxial loadings by adopting similar architectures as the ones displayed by diatoms. In addition, these results on centric diatoms demonstrated to be valuable for facilitating the study of the mechanical behavior of diatom frustules at different length scales.

The FEM displacement and von Mises stress distribution results for the centric diatom models present a valuable method of systematically studying diatom frustule mechanical behavior at different length scales.

4.4.2.2 Coscinodiscus sp. with "I-beam" cross sectional area

Similarly, a 3D model of a three-layered diatom frustule with "I-beam" junctions, connecting all layers, was simulated under compressive loads varying from 2.5 to 10 mN. Resultant displacement and stress distributions were found as depicted in Figure 40. In this case, the higher displacement and stress values were also found at the very center of the epitheca structure decreasing radially outward, but such levels were evenly distributed within the layers. These "I-beam" structural units located between the hierarchical porous layers (Fig. 40, side view), characterized via SEM [5], were found to be more deformable compared to the layered models without those connectors (Fig. 39).

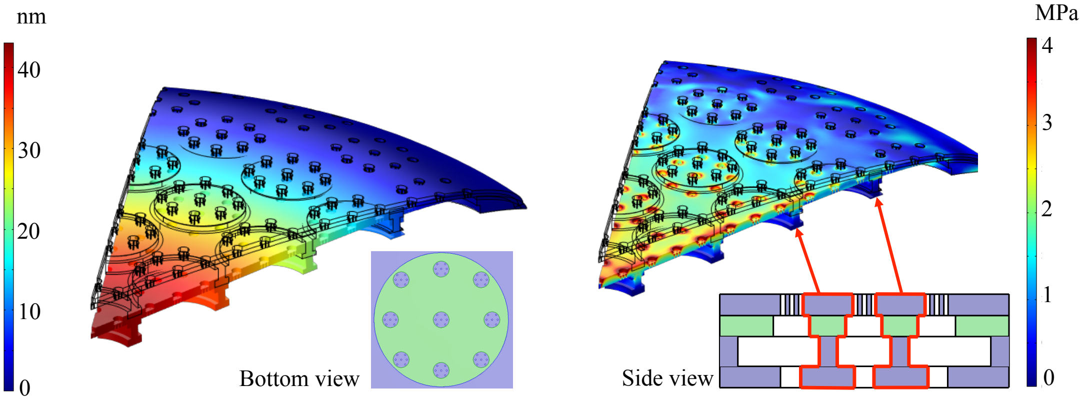

Figure 40. FEM displacement (left) and von Mises stress (right) distributions of another three-layered hierarchical diatom model with "I-beam" junctions between the siliceous porous layers. Load applied was 10 mN. The porous arrangements are stacked upon each other as observed in SEM images (Figure 1) and reported independently [5]. Both displacement (left) and stress (right) distributions varied radially as in Fig. 9, yet the structure is less deformable in this case.

Similar analysis of results in Fig. 10 shows the extent of the displacement and stress distributions of three-layered hierarchical epitheca models, containing "I-beams" connecting all layers, under similar compression simulations as before. These "I-beam" structural units located between the hierarchical porous layers (Fig. 10, side view), characterized via SEM [5], were found to be more deformable compared to the models without those connectors (Fig. 9).

Evenly distributed displacement and stresses were found within the porous layers. In comparison to the simple stack of three layers (Fig. 39), smaller deflections are evident in both displacement and stress distributions along the load direction. The response upon compression of this more structurally complex hierarchical model may be explained in terms of improved (or optimum) energy-efficient mechanisms to distribute stresses throughout the entire frustule, while maintaining its integrity and flexibility. To avoid potential simulation artifacts, the three porous layers were built in contact and the corresponding contact pairs were defined between neighbor layers.

Furthermore, Figure 40 revealed that higher displacement and stress concentrations are located at the center of the epitheca structure, decreasing radially outward. Similar radial von Mises stress distributions were independently reported recently [39], showing a preferential low stress concentration in the areas around the pores where cracks could grow faster. This design of nature is likely optimized to efficiently distribute stresses across the multiple porous layers to minimize larger stress concentrations at the most structurally vulnerable locations (e.g. pores).

Additionally, a parametric analysis of the uniaxial load was carried out to identify the effect of load increments on the mechanical response of the centric epitheca frustule, as shown in Figure 41. The pennate frustules were not included in this analysis due to their non-hierarchical structures. The constructed cross-sectional epitheca models, each made of three stacked porous layers with and without "I-beam" structural units, were investigated upon compression to evaluate the effect of the 'I-beam" junction commonly found in real diatom frustules. Results were compared with a simple stacking of three solid siliceous layers (i.e. without either "I-beams" or pores).

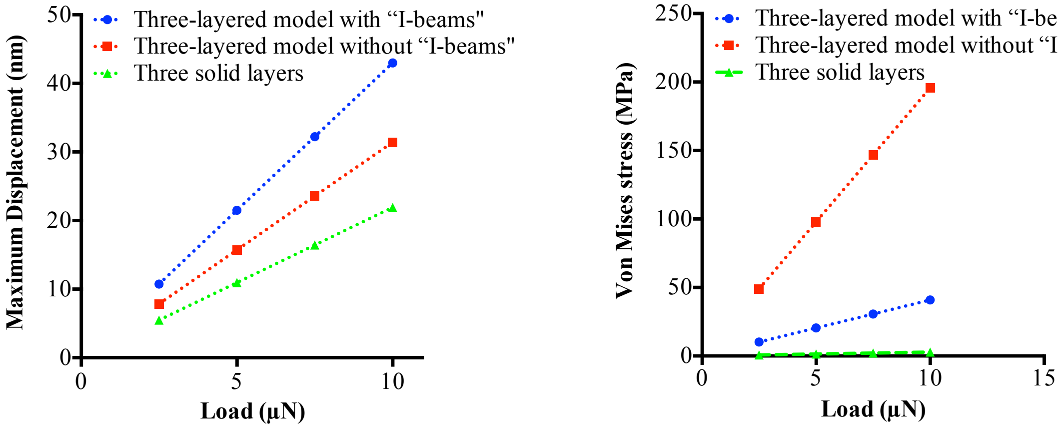

Figure 41. Maximum displacement (left) parametric study and von Mises stress (right) analysis of the three-layered epitheca model with "I-beam" structural units (blue dotted line), another equivalent three-layered model without the "I-beam" units (red dotted line), and a three-layered solid model without pores or "I-beam" junctions (green dotted line). This allows the study of the role of the unique cross-sectional structure present in real centric diatom frustules.

The role of the "I-beam" structural units in the mechanical response of varied hierarchical epitheca valves for centric diatoms was evaluated in this study (Fig. 41). The pennate frustules were not included in this analysis due to their non-hierarchical structures.

The parametric load study results in Fig. 41 supported the existence of an "ideal" (or optimum) design of diatom frustules when a three-layered porous model, another three-layered porous model with "I-beam" connectors, and three-layered solid model were compared under similar load conditions. As "I-beams" are introduced (blue), the *Coscinodiscus sp.* epitheca frustule shows higher flexibility (37% greater) than the simple three-layer stacked model (red), resulting in less overall stress in the epitheca structure. In addition, the insertion of pores on a layered structure (red) proved to allow larger displacements compared to similar solid structure (green) with almost 1.5 times the change in slope, while causing a considerable increase in the stress obtained, possibly due to higher localized stresses around the porous structures which correlates to a slope change of almost 70x. In a similar fashion, the model with "I-beams" (blue) almost doubled the slope value of the displacement when compared with a solid version (green), and exhibited roughly a 14x difference in slope values in terms of von Mises stress, making the "I-beams" model prone to failure without reaching failure.

It was also observed that the hierarchical model resembling real epithecas (blue) displays the greatest displacement and the least stress simultaneously, representing a highly deformable and robust structure. Findings in this study regarding the hierarchical models response to compression suggest that optimal designs for these (and other similar) microporous architectures possibly exist. The hierarchical structures in this work predict exceptional mechanical properties not reachable by simpler structures, and implies potential mechanisms for 3D construction of diatom frustules by mimicking real diatom structures as discussed in recent studies [40-42]. Additional systematic studies using experiments and simulations will be needed to confirm these predictions.

4.5 Summary

This study investigated the shell structure and mechanical properties of *Coscinodiscus sp.* and *Synedra sp.* diatom frustules using a combination of AFM nanoindentation and FEM simulation. Distinct features such as ribs and slits were encountered on the frustule of *Synedra sp.* and those were in good agreement with previously reported information.

The sample preparation method for AFM imaging and nanoindentation has been found to be highly suitable for efficient frustule distribution with improved adhesion characteristics compared to previous methods reported in the literature. AFM calibration was found to be critical toward obtaining accurate and reproducible images and nanoindentation data. Multiple AFM nanoindentations were successfully accomplished on selected frustules with high accuracy and reproducibility. AFM nanoindentation results indicate the elastic moduli of centric and pennate diatom frustules varied largely in value, and that they are significantly larger on average compared to those reported via ambient nanoindentation [23]. The difference in Young's moduli reported here compared to the ambient nanoindentation work has been identified to be due to the variability of diatom dimensions, sample preparation differences and related nanoindenter tip dimensions (which lead to dissimilar resolutions) among others.

The examination of pennate frustules via AFM imaging revealed a very different detailed construction of the diatom frustule from the centric diatom. A very symmetric group of ribs equally spaced along the longest axis of the frustule gives the reinforcement required to keep the frustule in place. The solid area in the center of the structure is critical to confer higher mechanical properties when compared with other structures while remaining lightweight.

A smaller scan area in one of the regions between slits in a pennate diatom showed a very small set of nanopores of approximately 100 nm in diameter. These pores were located between the reinforced ribs, which indicate its use for filtering different potential dangerous organisms while keeping the structure flexible and strong.

The multiple nanoindentation locations selected in the solid areas of the diatom frustule was important to capture small variations of the mechanical properties depending on the density of the silica material. The loads vs. displacement curves obtained from single indentations were analyzed and the mechanical properties were extracted according to the methods mentioned earlier. The average elastic modulus showed very low values when compared to bulk silica, which was unexpected but in agreement with other reports with similar and different measurement techniques.

Analysis of pre and post AFM indentation images indicated that the frustule topography was modified by the indenter, validating the methodology used in this study and probing at the set load the frustules went under elastic deformation only.

Similar analysis of AFM nanoindentations for pennate diatoms were carried out and their mechanical properties were calculated showing a higher elastic modulus due to his highly reinforced structure and lower porosity compared to the centric diatom studied, even at similar deflections.

The centric epitheca morphology was further investigated using SEM and AFM data through 3D CAD modeling. Each epitheca model was defined as a dome-shaped hierarchical assembly of three porous silica layers with connecting structural units ("I-beams"), which represent a real centric frustule structure as reported independently before [5]. This 3D hierarchical epitheca model of a real centric frustule was used to evaluate its role in the mechanical response of the overall frustule, and to investigate the microstructure-property relationships via FEM simulations to predict mechanical responses not easily measurable in the laboratory.

Due to the high variability in diatom dimensions with nanoscale features, future studies should enhance further the experimental methodology proposed in this work. A possible route is by selecting similar frustules (e.g. size) for a given diatom species, labeling them and performing SEM and subsequently AFM to ensure the exact same frustule regions are characterized. This will more precisely describe the morphological features of interest, which could help guide the selection of nanoindentation areas and for comparison purposes among various diatom frustules.

Regarding AFM imaging, future work could include various scanning areas of the diatom frustules, which will be limited by the number of AFM tips available. Further exploration of the use of the 3D views obtain from AFM imaging will likely contribute to identifying supplementary data or new features that could help describe completely the exact nature of pennate diatoms in particular. This will fill the gap of knowledge currently present on these elongated diatom species and potentially advance faster device design and nanotechnology applications.

4.6 References

1. Higgins, M.J., Crawford, S.A., Mulvaney, P., and Wetherbee, R. Characterization of the adhesive mucilages secreted by live diatom cells using atomic force microscopy. *Protist* **153**, 25-38 (2002).

2. Hamm, C.E., *et al.* Architecture and material properties of diatom shells provide effective mechanical protection. *Nature* **421**, 841-843 (2003).

3. Higgins, M.J., Sader, J.E., Mulvaney, P., and Wetherbee, R. Probing the surface of living diatoms with atomic force microscopy: The nanostructure and nanomechanical properties of the mucilage layer. *Journal of Phycology* **39**, 722-734 (2003).

4. Losic, D., *et al.* AFM Nanoindentations of diatom biosilica surfaces. *Langmuir* **23**, 5014-5021 (2007).

5. Losic, D., *et al.* Atomic force microscopy (AFM) characterisation of the porous silica nanostructure of two centric diatoms. *Journal of Porous Materials* **14**, 61-69 (2007).

6. Hildebrand, M., Doktycz, M.J., and Allison, D.P. Application of AFM in understanding biomineral formation in diatoms. *European Journal of Physiology* **456**, 127-137 (2008).

7. Garcia, A. and M. J. Buehler. Bioinspired nanoporous silicon provides great toughness at great deformability. *Computational Materials Science* **48**, 303-309 (2010).

8. Kröger N. and Poulsen N. Diatoms, from cell wall biogenesis to nanotechnology. *Annual Review of Genetics* 42, 83-107 (2008).

9. Gutu, T., Gale, K. G., Jeffryes, C., Wei, W., Chih-hung, C., Rorrer, G.L., and Jun, J. Electron microscopy and optical characterization of cadmium sulphide nanocrystals deposited on the patterned surface of diatom biosilica. *Journal of Nanomaterials* **2009**, 1-7 (2009).

10. Ki, J.S. *et al.* Comprehensive comparisons of three pennate diatoms, *Diatoma tenuae*, *Fragilaria vaucheriae*, and *Navicula pelliculosa*, isolated from summer Arctic reservoirs (Svalbard 79°N), by fine-scale morphology and nuclear 18S ribosomal DNA. *Polar Biology* **32**, 147-159 (2009).

11. Losic, D., Mitchell, J.G. and Voelcker, N.H. Diatomaceouslessons in nanotechnology and advanced materials. *Advanced Materials* **21**, 2947-2958 (2009).

12. Bie, L.-J. *et al.* Nanopillar ZnO gas sensor for hydrogen and ethanol. *Sensors and Actuators B* **126**, 604-608 (2007).

13. Kojtari, A., Carroll, P.J., and Ji, H.-F. Metal organic framework (MOF) micro/nanopillars. *CrystEngComm.* **16**, 2885-2888 (2014).

14. Nick, C., Quednau, S., Sarwar, R., Schlaak, H.F. and Thielemann, C. High aspect ratio gold nanopillars on microelectrodes for neural interfaces. *Microsystem Technology* 20, 1849-1857 (2014).

15. Wolfrum, B., Mourzina, Y., Mayer, D., Schwaab, D. and Offenhäusser, A. Fabrication of large-scale patterned gold nanopillar arrays on a silicon substrate using imprinted porous alumina templates. *Small* 2, 1256-1260 (2006).

16. Gebeshuber, I.C. *et al.* Atomic force microscopy study of living diatoms in ambient conditions. *Journal of Microscopy.* **212**, 292-299 (2003).

17. Almqvist, N., Delamo, Y., Smith, B.L, Thomson, N.H., Batholdson, A., Lal, R., Brzezinski, M. and Hansma, P.K. Micromechanical and structural properties of a pennate diatom investigated by atomic force microscopy. *Journal of Microscopy.* 3, 518-532 (2001).

18. Jeffryes, C. *et al.* The potential of diatom nanobiotechnology for applications in solar cells, batteries, and electroluminescent devices. *Energy & Environmental Science* **4**, 3930-3941 (2011).

19. Rountree C.L. *et al.* Atomistic aspects of crack propagation in brittle materials: Multimillion atom molecular dynamics simulations. *Annual Review of Materials Science.* **32**, 377-400 (2002).

20. Hamm, C.E. The evolution of advanced mechanical defenses and potential technological applications of diatom shells. *Journal of Nanoscience and Nanotechnology* **5**, 108-119 (2005).

21. De Stefano, L. *et al.* Interfacing the nanostructured biosilica microshells of the marine diatom Coscinodiscus wailesii with biological matter. *Acta Biomaterialia* **4**, 126-130 (2008).

22. Barton, J.E. and Odom, T.W. Mass-limited growth in zeptoliter beakers: A general approach for the synthesis of nanocrystals. *Nano Letters* **4**, 1525-1528 (2004).

23. Diaz Moreno, M., Ma, K., Schoenung, J., and Dávila L.P. The hierarchical porous structure and mechanical properties of diatoms: an integrated approach toward engineered nanotemplate. Submitted (2015).

24. Gebeshuber, I.C. *et al*. Diatom bionanotribology-biological surfaces in relative motion: their design, friction, adhesion, lubrication and wear. *Journal of Nanoscience and Nanotechnology* **5**, 79-87 (2005).

25. Kroger, N. and Sumper, M. The biogeochemistry of silica formation in diatoms. In Biomineralization (ed. E. Baeuer- lein). Wiley, Weinheim, Germany, 151–170 (2000).

26. Hildebrand, M. Silicic acid transport and its control during cell wall silicification in diatoms. In Biomineralization (ed. E. Baeuerlein). Wiley, Weinheim, Germany, 171–188 (2000).

27. Zimmermann, E.A. *et al.* Fracture resistance of human cortical bone across multiple length-scales at physiological strain rates. *Biomaterials* **35**, 5472-5481 (2014).

28. Al-Sanabani, J.S., Madfa, A.A. and Al-Sanabani, F.A. Application of Calcium Phosphate Materials in Dentistry. *International Journal of Biomaterials* **2013** 1-12 (2013).

29. Santos, H.A. Porous silicon for biomedical applications. Elsevier. (2014).

30. Capella, B and Dietler, G. Force-distance curves by atomic force microscopy. *Surface Science Reports* **34**, 1-104 (1999).

31. Higgins, M.J., Sader, J.E., Mulvaney, P. and Wetherbee, R.. Probing the surface of living diatoms with atomic force microscopy: The nanostructure and nanomechanical properties of the mucilage layer. *J. Phycol.* **39**, 722-734 (2003).

32. Francius, G. *et al*. Nanostructure and nanomechanics of live Phaeodactylum tricornutum morphotypes. *Environmental Microbiology* **10**, 1344-1356 (2008).

33. Ito, S. and Tomozawa, M. Dynamic fatigue of sodium-silicate glasses with high water content. *Journal of Colloidal Physics* **43**, c9-611-c9-614 (1982).

34. Le Parc, R., Levelut, C., Pelous, J., Martinez, V. and Champagnon, B. Influence of fictive temperature and composition of silica glass on anomalous elastic behaviour. *Journal of Physics: Condensed Matter* **18**, 7507 (2006).

35. Aw, M.S. Simovic, S., Yu, Y., Addai-Mensah, J. and Losic, D. Porous silica microshells from diatoms as biocarrier for drug delivery applications. *Powder Technology*. **223**, 52-58 (2012).

36. Bariana, A., Aw, M.S., Kurkuri, M. and Losic, D. Tuning drug loading and release properties of diatom silica microparticles by surface modifications. *International Journal of Pharmaceutics* **443**, 230-241 (2013).

37. Yu, X. *et al.* Green sacrificial template fabrication of hierarchical MoO_3 nanostructures. *CrystEngComm* **16**, 3935-3939 (2014).

38. Yoon, J.S. *et al.* Wetting characteristics of the anodic aluminum oxide template and fabrication of cracks using ultraviolet curable resin solution. *Applied Physic Letters* **104**, 091603-1-4 (2014).

39. Lu, J., Sun, C. and Wang, Q.J. Mechanical simulation of a diatom frustule structure. *Journal of Bionic Engineering* 12, 1 (2015).

40. Martin, J., Martin-Gonzales, M., Fernandez, J. and Caballero-Calero, O. Ordered three-dimensional interconnected nanoarchitectures in anodic porous alumina. *Nature Communications* 5, 1-9 (2014).

41. Dongchan, J., Meza, L.R. Greer, F. and Greer, J.R. Fabrication and deformation of three-dimensional hollow ceramic nanostructures. *Nature Materials* 12, 893-898 (2013).

42. Meza, L.R., Das, S. and Greer, J.R. Strong, lightweight, and recoverable three-dimensional ceramic nanolattices. *Science* 12, 1322-1326 (2014).

CHAPTER 5: CONCLUSIONS AND RECOMMENDATIONS

5.1 Conclusions

The approach of coupling experimental and simulation methods used in this study reproduces satisfactorily the conditions observed in testing of real diatoms and provides insights about their structure-property relationships for predictive studies and design.

High-resolution microscopy (SEM and AFM) reveals two distinct diatom species structures. Centric frustules (*Coscinodiscus sp.*) were comprised of porous layers. Pennate diatoms (*Synedra sp.*) consist of elongated valve surfaces with lateral ribs and slits. These results particularly expose the large variability in nature of diatom frustule dimensions (e.g. frustule or pore diameter), even within a given species. A methodical procedure of diatom frustule sample preparation and characterization prior to experimentation is hence presented in this work. The benefit of using these techniques is the ability to obtain improved and more reproducible measurements than those obtained using conventional sample preparation and single microscopy usage (SEM or AFM only).

A systematic procedure can be used to evaluate the mechanical properties of diatom species via ambient nanoindentation experiments and predictive FEM simulations. The ambient nanoindentations revealed remarkable size-dependent Young's moduli and hardness, mainly due to dominant porosity and frustule morphology. Nanoindentation measurements for the centric *Coscinodiscus sp.* frustules indicate a range of E and H between 1.11-10.59 GPa and 0.10-1.03 GPa, respectively. Nanoindentation results for the *Synedra sp.* frustules show significantly higher E and H values ranging between 13.7-18.6 GPa and 0.85-1.41 GPa, respectively. The combination of a mechanically resistant frustule with high aspect ratio and rib-slit structure contributes to their mechanical robustness compared to the centric (*Coscinodiscus sp.*) frustules by efficiently distributing stresses along the longest axis of the structure, while taking advantage of their highly reinforced structure as demonstrated in Chapter 3.

3D CAD diatom models (flat-shaped, single layer epitheca) can be successfully applied to simulate the experimental mechanical response of diatom frustules, and to design diatom-inspired structures. FEM simulations of these diatoms highlight details of the effect of a uniform compression load on diatom frustule deformation. Simulation results show that the frustules investigated (*Coscinodiscus sp., Synedra sp. and F. kerguelensis*) differed notably in their mechanical behavior under uniform compression.

For centric (*Coscinodiscus sp.*) frustules, centralized and decreasing radially outward compressive strains and modest von Mises stress distributions are predicted. For pennate (*Synedra sp.*) frustules, compression conditions result in uniform elevated strains and von Mises stress distributions when compared to centric diatoms. Modifying morphological variables (e.g. pore diameter or slit width) in the frustules investigated in this study show improved structures, either with higher deformability or lower threshold for sustaining stress distributions around critical areas, such as frustule edges. A similar experimental-simulation approach allowed the analysis of the mechanical properties of another pennate (*F. kerguelensis*) frustule with characteristic pores, instead of slits. The benefits of modeling these diatom frustules include the ability to perform simpler simulations that require shorter computing times compared to those pursued typically (e.g. with much frustule structure details that lead to limited calculations). The advantages of the FEM simulations include the ability to study real diatoms in a cost- and time-efficient fashion, isolate features that are not readily measurable in experiments and investigate relevant conditions for specific applications (e.g. nanotemplates).

The implications of the relationships between mechanical properties vs. porosity examined in this study of diatoms are multi-fold. These include the ability to identify superior deformability (or stress-resistance) of similar diatom-inspired structures, investigate the role of the layered structure characteristic of a centric diatom frustule, incorporate advanced structural mechanical analysis for the study of hierarchical layers, design tailored properties for desired geometries, and map strategies for the fabrication of nanostructures and nanodevices.

Nanomechanical testing and simulation-based prediction of von Mises stress distributions in diatom frustules can help guide fabrication efforts, for example by guiding the calculation of the amount and location of nanomaterials to be deposited on porous nanotemplates. Applications subject to significant stress, such as in drug delivery via diatom frustule carriers, might be feasible with a structure similar to the pennate diatom (*F. kerguelensis*) as reported in this study. Most significantly, the results presented here could be applied to nanoparticle-encapsulated diatoms to deliver therapeutics, similar to those recently investigated by Todd *et al*. (2014). This research is important toward understanding hierarchical porous structures and developing advanced materials for a wide range of applications via controlled morphologies and structures.

AFM imaging was successfully used in this study to characterize diatom morphology including hierarchical layers, and pre- and post-AFM nanoindentations where systematic and robust sample preparation and data analysis were used. The high spatial resolution of AFM imaging proved to be useful in revealing depth profiles of porous layers of diatom frustules and accurate measurements of pore diameters. Special sample preparation (cross sectional areas) is required to access interconnected porous layers as reported by Losic *et al.* 2007.

The multiple AFM-based nanoindentations performed in this investigation demonstrate the effectiveness of this localized technique in analyzing biomineralized structures, where mechanical properties are region dependent. This high-resolution technique has the advantage of evaluating surface modifications before and after an indentation, which proved to be critical for verifying indentation locations, despite its low scan speed and small scan area.

The 3D CAD models created in this study, based on SEM and AFM images, are valuable representations of realistic diatom frustules that permit the prediction of mechanical behavior under uniaxial loadings (e.g. stress radially increasing for centric and longitudinally increasing for pennate diatoms), which is not experimentally available to date. The results reported here will help in determining potential applications such as nanomaterials deposition and drug delivery carriers in future research efforts.

The parametric loading study presented (Chapter 4) is a useful tool for evaluating the linear relationship of the von Mises stress of a section of a diatom frustule to the applied uniaxial load. Models with hierarchical structures and "I-beam" connectors reveal a more efficient mechanism to distribute stress at higher loads, suggesting these model types for bio-inspired design of nanodevices. The higher deformability exhibited by the frustule models with "I-beams" will be strategic for future device design based on brittle materials with hierarchical architectures.

By combining both experimental and simulation techniques, this study offers a unique and powerful approach to study diatoms and similar porous biosilica organisms. Selected nanomechanical experiments can be first used to obtain the species-dependent Young's modulus of the diatom of interest and to identify variables (e.g. porosity) that contribute to the overall behavior of the diatom frustule under compressive loads. Then, FEM simulations can be applied to more precisely investigate important structural features (e.g. pores, ribs and slits) depending on diatom morphology at a smaller length-scale.

The improved 3D CAD diatom models and FEM simulations presented here provide important insights into the nature of the structural modifications that occur in porous diatom frustules in the 0-10 mN load regime, as measured in prior studies (Losic *et al.* 2007, Yao *et al.* 2005). The hierarchical makeup of the centric frustule (porous layers connected with "I-beam" structural units) resulted in a unique structure where the overall frustule mechanical response is highly influenced by their internal configuration. The mechanical response of the centric frustule is found in this study to be associated mostly with the intrinsic hierarchical structure of diatoms (vs. the frustule material itself). This finding is consistent with experimental and theoretical results that have predicted the important role of the hierarchical nature of the diatom frustule under varied load conditions.

The mechanical studies reported on diatom frustules evidence large variability due to differences in testing techniques such as ambient nanoindentations (Yao *et al.* 2005), AFM nanoindentations (Losic *et al.* 2007), micro-glass needle compressions (Hamm *et al.* 2003). In addition, challenges in sample preparation and size-dependent mechanical behavior of diatoms need to be resolved by applying standardized protocols and increase the number of tests for reproducibility purposes.

In recent decades, theoretical and simulation investigations have increasingly been used as tools for producing fundamental scientific findings (Almqvist *et* al. 2002 , Losic *et al.* 2007, Hildebrand *et al.* 2008) and for making scientific studies practical. Despite this, the challenge remains to determine to what extent a simulation can be used to describe real physical systems and properties, even when a particular simulated property is in agreement with the real material property. As J.M. Haile stated "a simulation is not performed of a physical system but rather of a model of the physical system", thus no simulation can be assumed to precisely replicate a given physical system. Following J.M. Haile's well-known remark that "a simulation is not performed of a physical system but rather of a model of the physical system", thus no simulation can be assumed to precisely replicate a given physical system. A simulation can however reproduce remarkably well specific aspects or phenomena of a suitable model, thus the increasing use in scientific research. In order to get more realistic simulations, it is imperative to account for non-uniformities in the mechanical properties across the frustule and it could be challenging to define specific and small regions via FEM simulations. The best applications of the simulation methods in this work include studies focused on macroscale features (e.g. microfluidic devices) for which experimental data is available. This study contributed to current knowledge on diatoms by bridging the gap between current experimental and simulation.

The research results presented in this work on diatoms would vary in other relevant conditions (e.g. aqueous environments), for which advanced environmental studies have emerged (Higgins *et al.* 2003). Such efforts reveal that climatic factors affect the mechanical properties of diatom frustules, with implications for further research for applications in liquid media (e.g. interstitial fluid for drug delivery) as reported before (Le Parc *et al.* 2006, DeMaster 2004). The water content in the composition of diatoms in nature (biosilica glass) is observed to significantly decrease their frustule elastic modulus, even more than increased temperature, when analyzed via Brillouin scattering (Le Parc *et al.* 2006). In addition, the silicon content in the composition of diatom frustules (e.g. via absorption from the environment) is found important, as undersaturated conditions will cause partial dissolution of the frustule, thus reducing their elastic modulus (DeMaster 2004). These studies re-affirm that advancement in technology and methods is pivotal for innovation and research on additional properties and applications (e.g. microfluidics).

The overall contribution of this dissertation consists in applying experimental-simulation techniques in a different (and new) manner to characterize the micro- and nano-scale structure of porous diatom frustules at elevated compression loads, and to explore the role of porosity and hierarchical structures on the overall mechanical response of real diatoms. This study will help advance the current understanding of the structure-property relationships in porous materials for predicting and tuning future diatom-inspired silica designs (e.g. nanotemplates) and for future fabrication purposes.

5.2 Future work

The use of environmental SEM (ESEM) will help to image the diatom samples before ambient nanoindentations and without the necessity of adding coating materials to increase conductivity during SEM imaging (e.g. gold). The use of this technique will allow imaging mounted diatom samples before and after ambient nanoindentations to evaluate indentation marks and enhance further analysis of specific frustules. The investigation of fracture modes via *in situ* SEM will be advantageous in evaluating maximum loads before failure, as well as fracture modes of diatom frustules. In addition, *in-situ* SEM or AFM with appropriate sample preparation will allow experimental investigation of the role of porous layers and their interconnected "I-beams" (cross sectional areas) on the mechanical behavior of diatom frustules, and comparison with the predicted results presented in this work.

In future studies, the experimental evaluation of additional diatom species will be beneficial for investigating correlations between frustule symmetry and expected mechanical properties (e.g. comparative pennate vs. centric frustule strength). These tests should be quite feasible, assuming an ambient nanoindentation apparatus is readily available, since this technique is relatively simple and cost-effective compared to other nanoindentation methods (e.g. AFM nanoindentation). In addition, the use of varying loads will allow an added value of investigating the elastic-plastic behavior, and even failure modes in diatom frustules. It will be necessary also to increase the number of indentation locations on diatom frustules to inspect various spatial correlations on the mechanical behavior (e.g. tests along main symmetrical axis). Given the high spatial resolution of AFM-based nanoindentations it will be important to measure the contribution of each porous layer independently to the overall frustule mechanics.

Potential simulation efforts including the study of flat-shaped vs. dome-shaped top (epitheca) valves in centric frustules will be important to advance the current knowledge of the role of the convex surfaces that exist within intricate architectures in biological systems such as diatoms. The hierarchical nature of the centric diatom frustules have been investigated and compared well with prior measurements (Losic *et al.* 2007), future increasingly realistic diatom models and investigation of their mechanical properties could be enhanced further using techniques described in this study. The role of the "I-beam" structural units in the interconnected frustule layers will be key in the understanding of the mechanical response of the overall frustule.

Furthermore, experimental and simulation efforts (e.g. to examine the role of porosity on von Mises stress) will be needed to investigate diatom species-specific Young's moduli and entire diatom frustule morphology as design criteria for optimizing material performance. Equipment to measure porosity and pore size distribution (e.g. porosimetry and surface measurements such as dynamic vapor sorption or inverse gas chromatography) can aid the assessment of practical methods to measure the dependence of the mechanical behavior of diatom frustules on porosity. In addition, the use of techniques based on settling velocity (e.g. sedigraph), electrical resistance pulse counting (e.g. coulter counter), and laser diffraction (e.g. Malvern laser sizer) will be useful for studying monodisperse populations of diatom frustules (i.e. similar frustule diameter), minimizing the impact of one of the mentioned variables.

Further progress in materials innovation, testing methods and additive manufacturing will also be needed to fully characterize the effects of microstructure on associated properties, and to design for performance across many length scales. Recent diatom research (Jang *et al.* 2013, Belegratis *et al.* 2014) indicates that studies such as the present work are necessary for the fabrication of prototypes of diatom-inspired structures with desired properties. Future investigations could involve analysis of key structural parameters (e.g. individual features and porous layers) via experiments and simulations similar to those performed independently (Losic *et al.* 2007). The ultimate goal is to clarify the origin of the mechanical response of diatom frustules, which can then help to explain the nature of characteristically deformable and lightweight diatoms.

APPENDIX A – 3D-printed Micromanipulator and a Glass Microneedle

Courtesy of Backyard Brains.

APPENDIX B – Materials Simulations: Length and Time Scales

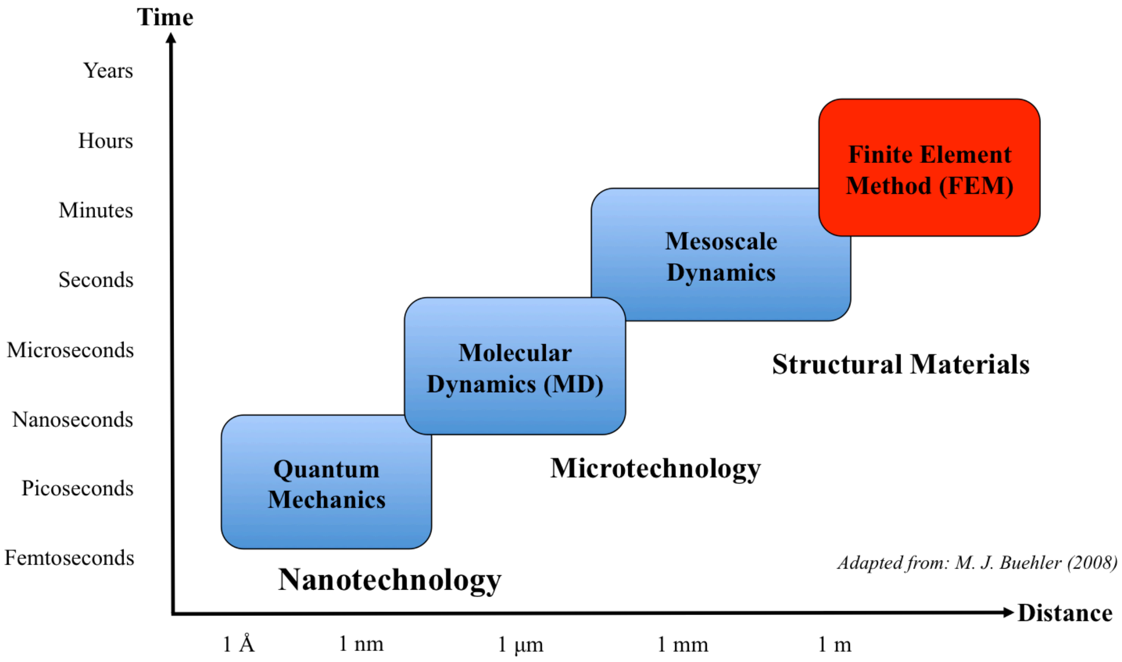

Adapted from: M. J. Buehler (2008)

APPENDIX C – FEM General Procedure

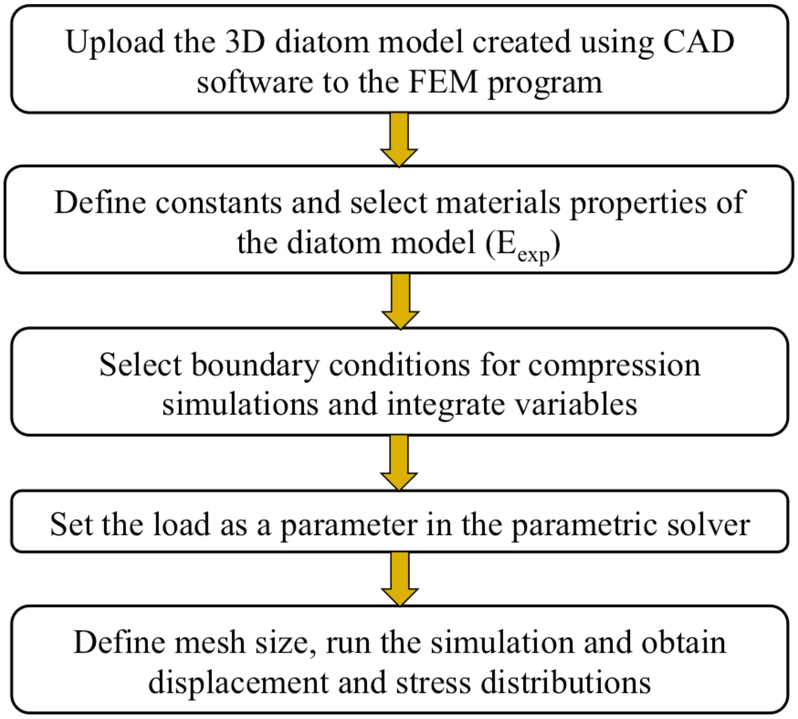

APPENDIX D – Graphic Procedure for Simulating 3D Diatom Models